

AD-A137 902

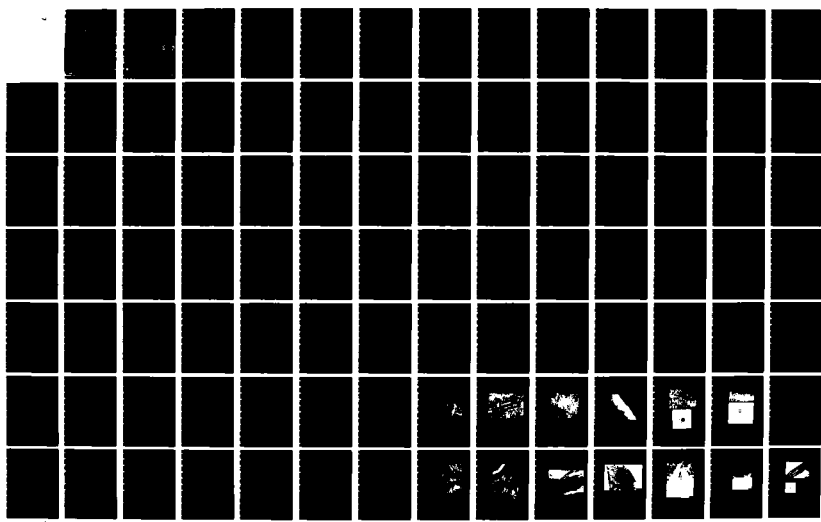
BARRIERS TO THE MIGRATION OF INTERPHASE BOUNDARIES (U)
CARNEGIE-MELLON UNIV PITTSBURGH PA H I AARONSON ET AL.
06 JAN 84 ARO-17094.1-MS DABG29-80-C-0018

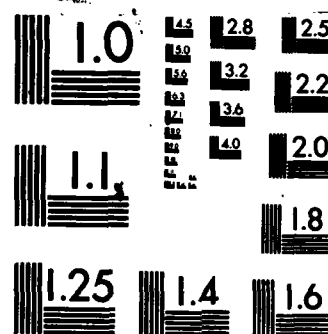
1/2

UNCLASSIFIED

F/G 11/6

NL





MICROCOPY RESOLUTION TEST CHART
NATIONAL BUREAU OF STANDARDS-1963-A

ADA137902

Unclassified

SECURITY CLASSIFICATION OF THIS PAGE (When Data Entered)

ARO 17298.1-MS
ARO 17094.1-MS

REPORT DOCUMENTATION PAGE			READ INSTRUCTIONS BEFORE COMPLETING FORM
1. REPORT NUMBER 17094.1-MS	2. GOVT ACCESSION NO. AD-A137902	3. RECIPIENT'S CATALOG NUMBER	
4. TITLE (and Subtitle) Barriers to the Migration of Interphase Boundaries		5. TYPE OF REPORT & PERIOD COVERED Final: 3 Oct 79 - 8 Sep 83	
7. AUTHOR(s) H. I. Aaronson, W. T. Reynolds, Jr., K. Chattopadhyay, and G. J. Shiflet		8. CONTRACT OR GRANT NUMBER(s) DAAG29 80 C 0018 80 K 0071	
9. PERFORMING ORGANIZATION NAME AND ADDRESS Carnegie-Mellon University Pittsburgh, PA. 15213		10. PROGRAM ELEMENT, PROJECT, TASK AREA & WORK UNIT NUMBERS 17094-MS 17298-MS	
11. CONTROLLING OFFICE NAME AND ADDRESS U. S. Army Research Office Post Office Box 12211 Research Triangle Park, NC 27709		12. REPORT DATE January 6, 1984	
14. MONITORING AGENCY NAME & ADDRESS (if different from Controlling Office)		13. NUMBER OF PAGES	
		15. SECURITY CLASS. (of this report) Unclassified	
		15a. DECLASSIFICATION/DOWNGRADING SCHEDULE	
16. DISTRIBUTION STATEMENT (of this Report) Approved for public release; distribution unlimited.			
17. DISTRIBUTION STATEMENT (of the abstract entered in Block 20, if different from Report)			
18. SUPPLEMENTARY NOTES The view, opinions, and/or findings contained in this report are those of the author(s) and should not be construed as an official Department of the Army position, policy, or decision, unless so designated by other documentation			
19. KEY WORDS (Continue on reverse side if necessary and identify by block number) Ferrite, carbide, interphase boundary structure, nucleation, growth, solute drag effect, barrier, bainite, incomplete transformation, martensite, O-lattice, shear, dislocations			
20. ABSTRACT (Continue on reverse side if necessary and identify by block number) The incomplete transformation phenomenon was shown to be absent in Fe-C-Mo alloys containing 0.15 - 0.25% C and 2½ - 4½% Mo. Four different types of thickening kinetics of grain boundary allotriomorphs were observed in the temperature region at and just above that of the bay in the TTT-diagram. Close to the bay in the richest alloys, growth was found to cease entirely for perceptible intervals. Cessation of growth for sufficiently long times was identified as an essential			

DTIC
ELECTE
S FEB 15 1984

FILE COPY

UNCLASSIFIED

SECURITY CLASSIFICATION OF THIS PAGE (When Data Entered)

Alpha Sub 1

Cont'd

20.

element for the occurrence of incomplete transformation. Radical changes in ferrite and carbide morphology were catalogued in and below the bay region in a representative Fe-C-Mo alloy. The solute drag-like effect appears to be the primary factor responsible for incomplete transformation, for the complex growth kinetics observed in the present alloys and for the morphological effects in the bay region. Evolution of the interphase boundary structure of α Cu-Zn plates was studied with high-resolution TEM. Initially these plates are fully coherent with no internal structure. First one set of misfit dislocations, with Burgers vector out of the habit plane and then a second is acquired from the matrix phase. This sequence is compatible only with a diffusional growth mechanism. Comparison with α Cu-Zn martensite interfacial and internal structures shows major differences. A detailed O-lattice analysis of fcc:bcc partially coherent interfaces is made, revealing numerous possible 2-dislocation network structures. Comparison with our previous computer modeling of these interfaces shows that the two approaches usually yield closely similar results. An experimental study of interphase boundary structures in a Cu-Cr alloy, conducted at Univ. of CA. at Berkeley at very high resolutions, supported the validity of the theoretical analysis.



A-1

Barriers to the Migration of Interphase Boundaries

TABLE OF CONTENTS

List of Captions

A. Publications Resulting in Whole or in Part From Research Supported by the ARO Contract Since Its Inception	6
1. First Three Years (1973 - 1976)	6
2. Second Three Years (1976 - 1979/1980)	7
3. Third Three Years (1980-1983)	8
B. Personnel and Supplemental Support Situations	10
C. The Proeutectoid Ferrite and Bainite Reactions in Fe-C-X Alloys	10
1. The Incomplete Transformation Phenomenon in Fe-C-Mo Alloys	11
a. Introduction	11
b. Experimental Procedures	13
c. Results	14
d. Discussion	16
2. Ferrite and Carbide Morphologies At and Below the Bay of a Representative Fe-C-Mo Alloy	25
a. Introduction	25
b. Experimental Procedures	25
c. Results	25
d. Discussion	28
3. Evaluation of the Relative Effects of Various Factors on Ferrite Growth Kinetics in Fe-C-X Alloys	29
a. Introduction	29
b. Thermodynamic Effect	30
c. Effect of Carbide Precipitation at α:γ Boundaries	30
d. Solute Drag-Like Effect	32

4. Theoretical Analysis of the Solute Drag-Like Effect	33
D. Interfacial Structure Barriers to Growth	38
1. The Role of Interphase Boundary Structure During Phase Transformations in β and β' Cu-Zn Alloys	39
a. The Interphase Boundary Structure and Growth Mechanism of α_1 Cu-Zn Plates	39
(1) Introduction	39
(2) Experimental Procedure	40
(3) Results	41
(4) Discussion	45
b. The Interphase Boundary Structure of α_1 Martensite Cu-Zn Plates	47
(1) Introduction	47
(2) Experimental Procedure	47
(3) Results	47
(4) Discussion	49
c. Structure of the Lengthwise Interfaces of α Cu-Zn Rods	52
(1) Introduction	52
(2) Experimental Procedure	52
(3) Results and Discussion	52
2. The Structure of Partially Coherent Fcc:Bcc Boundaries	54
a. Comparison of the O-Lattice and Computer Matching Models of Fcc:Bcc Interfaces	55
(1) Introduction	55
(2) The O-Lattice Procedure	55
(3) Choice of $S^{(1)}$ and $S^{(2)}$	56
(4) Assignment of Interfaces	56
(a) Cell Sectioning	56
(b) Dislocation Pairs	57

(5) Comparisons with RA	58
b. Structure of Facets on Bcc Cr-rich Precipitates in a Cu-Cr Alloy	59
(1) Introduction	59
(2) Experimental Procedure	60
(3) Results	61
(4) Discussion	62
Bibliography	63

List of Captions

Fig. 1 TTT-curves for the initiation of transformation in the bay region of Fe-C-Mo alloys containing ca. (a) 0.15% C, (b) 0.20% C and (c) 0.25% C, and the Mo concentrations indicated in each Figure.

Fig. 2 Typical optical microstructures, in Fe-0.18% C-4.25% Mo reacted at 580°C for (a) 11 hrs.; (b) 1 day, (c) 5 days, and (d) Fe-0.17% C-3.76% Mo reacted at 610°C for 3 days. Nital etch. Magnification bar represents 40 microns.

Fig. 3 Interphase boundary carbides during stage 2, type III growth in Fe-0.17% C-3.76% Mo reacted for 1 day at 600°C.

Fig. 4 Fibrous carbides in same specimen as Fig. 3.

Fig. 5 Extraction replica showing nearly equal growth of fibrous and interphase boundary carbide structures.

Fig. 6 (a) Extraction replica of interphase boundary carbides in stage 3, type IV growth in Fe-0.18% C-2.25% Mo reacted 6 days at 570°C. (b) SAD pattern for Mo_2C .

Fig. 7 (a) Extraction replica of fibrous carbides in same specimen as Fig. 6. (b) SAD pattern for Mo_2C .

Fig. 8 Fraction transformed vs. time in Fe-0.19% C-2.30% Mo.

Fig. 9 Fraction transformed vs. time in Fe-0.15% C-3.40% Mo.

Fig. 10 Experimental illustration of all four types of allotriomorph thickening kinetics. (S/2 = half thickness)

Fig. 11 (a) Schematic illustrations of the four types of allotriomorph thickening kinetics. (b), (c) and (d): Composition regions within which the four types of thickening kinetics occur as a function of temperature interval, ΔT , above the bay.

Fig. 12 Comparison of experimental thickening kinetics (fitted to t^1 and $t^{1/2}$ growth laws) with calculated kinetics on various models for: (a) Type I growth, in Fe-0.19% C-2.30% Mo at 650°C; (B) Type II growth, in Fe-0.18% C-4.25% Mo at 620°C; (c) Type III growth, in Fe-0.17% C-3.76% Mo at 580°C; and (d) Type IV growth, in Fe-0.18% C-4.25% Mo at 560°C.

Fig. 13 Optical micrographs of ferrite/bainite morphology round the bay of Fe-0.19% C-2.30% Mo at early stages of transformation. Bay temperature--610°C-615°C. (a) 625°C/5000 secs.; (b) 615°C/5000 secs.; (c) 610°C/5000 secs.; (d) 595°C/5000 secs.; (e) 575°C/50 secs.; (f) 550°C/10 secs.; (g) 525°C/10 secs.

Fig. 14 Optical micrographs of ferrite/bainite morphology round the bay of Fe-0.19% C-2.30% Mo at relatively late stages of transformation. (a) 625°C/50,000 secs.; (b) 610°C/72,000 secs.; (c) 595°C/72,000 secs.; (d) 575°C/20,000 secs.; (e) 525°C/50 secs.; (f) 475°C/5 secs.

Fig. 15 Lath-type carbides in bainite. Fe-0.19% C-2.30% Mo, reacted $610^{\circ}\text{C}/10,000$ secs.

Fig. 16 Mo_2C precipitated at dislocations within ferrite. Fe-0.19% C-2.30% Mo, reacted $610^{\circ}\text{C}/10,000$ secs.

Fig. 17 Dislocation-nucleated carbides at a lower reaction temperature. Fe-0.19% C-2.30% Mo, reacted $575^{\circ}\text{C}/72,000$ secs. (a) Bright field; (b) dark field.

Fig. 18 Very fine interphase boundary carbides formed well below the bay. Fe-0.19% C-2.30% Mo, reacted $610^{\circ}\text{C}/72,000$ secs. (a) Bright field; (b) dark field.

Fig. 19 Large cementite laths formed at boundaries between ferrite laths, photographed at low magnification. Fe-0.19% C-2.30% Mo, reacted $475^{\circ}\text{C}/5$ secs.

Fig. 20 (a) and (b) Large cementite laths formed at boundaries between ferrite laths, photographed at high magnification and in bright and in dark field. (c) Dark field micrograph of very small Mo_2C particles. Fe-0.19% C-2.30% Mo, reacted $475^{\circ}\text{C}/5$ secs.

Fig. 21 $\alpha_{\text{Fe-C-X}}/\alpha_{\text{Fe-C}}$ calculated and measured as a function of temperature in the indicated Fe-C-X alloys, where the A/O C is the same in the Fe-C as in the Fe-C-X alloys.

Fig. 22 $G_{\text{Fe-C-X}}/G_{\text{Fe-C}}$ calculated as a function of temperature in the indicated Fe-C-X alloys, where the A/O C is the same in the Fe-C as in the Fe-C-X alloys (solid curves). G_{carb}/G , the ratio of the ledgewise growth rate in the presence of carbides at $\alpha:\gamma$ boundaries to that in the absence of carbides, calculated as a function of temperature in the indicated Fe-C-X alloys (dashed curves).

Fig. 23 Ratio, R, of $\alpha_{\text{experimental}}/\alpha_{\text{paraequilibrium}}$ as a function of temperature for Fe-C-X alloys, of which all but Fe-C-V contain ca. 3 A/O X.

Fig. 24 Indexed selected area diffraction pattern confirming that α_1 Cu-Zn has a 3R structure but not a superlattice.

Fig. 25 Coherency strain contrast associated with α_1 plates during early stages of growth. Cu-38.64 A/O Zn, reacted $250^{\circ}\text{C}/45$ secs., $g = [110]_{\beta'}$.

Fig. 26 Coherent α_1 plate observed at three different tilts in Cu-43.40 A/O Zn after $250^{\circ}\text{C}/150$ min. Arrows mark the position where a matrix dislocation is about to react with the plate.

Fig. 27 Bright field micrograph showing interaction between matrix dislocations and coherent α_1 plates exhibiting dipole strain contrast in Cu-38.64 A/O Zn, quenched to room temperature, aged $250^{\circ}\text{C}/180$ secs.

Fig. 28 α_1 plate encircled by one set of misfit dislocations which also bound stacking faults in the plate. Cu-38.64 A/O Zn, reacted $250^{\circ}\text{C}/300$ secs.

Fig. 29 Dark field micrographs, taken in a variety of matrix reflections, of the same α_1 plate broad face. One set of misfit dislocations is present. (f) is an enlargement of a portion of (b). (g) summarizes results from the contrast experiments. (h) stereoplots of crystallographic data from the trace analysis and contrast experiments.

Fig. 30 (a) Stacking faults and misfit dislocations are displayed in strong contrast.
 (b) Viewed in another reflection which makes the faults and dislocations extinct, growth ledges appear through cusps produced in extinction contours.
 (c) Another α_1 plate, imaged with an $(009)\alpha_1$ reflection, shows cusps in contours under strong two-beam conditions.

Fig. 31 Dark field micrograph imaged in an α_1 reflection and tilted slightly out of the Bragg condition to reveal growth ledges.

Fig. 32 (a) Adsorption of second set of matrix dislocations at $\alpha_1:\beta'$ interface. Inset is an enlargement of a weak-beam image of part of the dislocation being adsorbed; splitting confirms that this is a superdislocation. (b) Second set of misfit dislocations formed at junction between impinged α_1 plates.

Fig. 33 Structure of α_1 interfaces during the third stage of thickening: (a) strong stacking fault contrast; (b) after tilting, two sets of misfit dislocations are revealed; (c) a relatively early stage in adsorption of a second set of misfit dislocations from the matrix, with examples pointed out by arrowheads; (d) A $g-5g$ ($g = [110]$) weak-beam image showing geometrical arrangement of the second set of dislocations; (e) sketch of the interfacial structure in (d).

Fig. 34 Images in two different reflections of faceting at an $\alpha_1:\beta'$ interface after 90 min. reaction at 250°C (Cu-37.38 A/O Zn).

Fig. 35 Series of micrographs, taken at different tilt angles, of the edge of an α_1 plate. Numbers indicate different tilts. The dark and bright field pair at position 3 was taken under exact two-beam conditions. The dark field micrograph at position 4 was taken with the same operating reflection but under weak-beam conditions.

Fig. 36 Half-thickness vs. time of α_1 plates. Solid circles--isothermally reacted at 450°C; open circles--quenched and aged to 250°C; triangles--isothermally reacted at 300°C. Dashed line was calculated assuming volume diffusion-control and disordered $\alpha_1:\beta'$ boundaries.

Fig. 37 Thick α_1 martensite plates.

Fig. 38 Thin (likely thermoelastic) α_1 martensite plates.

Fig. 39 One set of misfit dislocations and the stacking faults they bound in a thick α_1 martensite plate.

Fig. 40 Central area shows a portion of a thick martensite plate at low magnification. Peripheral micrographs illustrate portions of its interphase boundary at higher magnification and demonstrate that extinction of misfit dislocations occurs everywhere with the same reflection.

Fig. 41 A thin α_1 martensite plate, shown at lower (a) and at higher (b) magnifications. Close inspection of (a) shows that a second set of faults is present and is associated with ledges in the interphase boundary. Ledges are outlined with dashed lines in (b).

Fig. 42 Interfacial dislocation structure of a thicker α_1 martensite plate viewed in three different reflections.

Fig. 43 Stereoplot summarizing crystallographic results obtained from the martensite plate in Fig. 42. Note that Burgers vector of interfacial dislocations lies out of both habit plane and fault plane.

Fig. 44 Stereoplot of crystallographic data from another martensite plate, confirming the results of Fig. 43.

Fig. 45 Reconfirmation of Fig. 43 findings with a more accurate technique: (a) foil oriented so that fault traces and misfit dislocations are colinear. (b) habit plane determination from (a). (c)-(e) Burgers vector determination via $g:b$ method. See (b) for plot of results.

Fig. 46 Analysis similar to that of Fig. 45 for a martensite plate located near the edge of thin foil. Now the Burgers vector of dislocations lies in the fault plane.

Fig. 47 Determination of the habit plane in β' of the faceted interfaces noted on an α rod.

Fig. 48 Habit planes of facets on another α rod.

Fig. 49 (a) Low magnification view of three α rods. (b) Higher magnification micrographs of interfaces a_1 , a_2 and a_3 noted in (a). Small differences in interphase boundary orientation are seen to yield substantial changes in interfacial structure.

Fig. 50 Micrographs in different reflections for a $g:b$ analysis of a facet on an α rod.

Fig. 51 An α rod viewed in (a) a precipitate and (b) a matrix reflection, showing faulting and faceting of the originally smooth interphase boundaries.

Fig. 52 Three inequivalent O-lattice cells obtained by using different sets of $a/2 <110>$ Burgers vectors for misfit dislocations; orientation relationship between fcc and bcc is held constant.

Fig. 53 Schematic diagram showing O-lattice cell and 9 planes defined by $\{001\}^\circ$ (nos. 1-3) and $\{110\}^\circ$ (nos. 4-9). Nos. 7-9 are planes containing dislocations with large Burgers vectors, $a/2 <112>$.

Fig. 54 Fifteen different interfaces are derived from consideration of pairs of $a/2 <110>$ Burgers vectors.

Fig. 55 Location of the seven habit planes calculated by the "dislocation pairs" method for the Nishiyama-Wassermann orientation relationship.

Fig. 56 Habit plane normals and O-lattice vector directions for orientation relationships in the range $+2^\circ <\theta<-7^\circ$.

Fig. 57 Theoretical interfaces derived for the same range of orientation relationships considered in Fig. 56. The values listed are for the three "best" interfaces, as characterized by the P parameter. The interfaces marked (+) also have three-dislocation descriptions but with dislocation line densities within 1% of those of the interfaces shown.

Fig. 58 Comparison of the O-lattice and computer modeled interfaces for superimposed $(111)_{\text{fcc}}$ and $(110)_{\text{bcc}}$ planes. The large open circles are O-lattice points and the small symbols $+, \circ$ are lattice coordinates of the bcc and fcc crystals respectively showing the nearest matching points. The heavier arrows mark the O-lattice vectors detailed by the indices. (a) $\theta = 0^\circ$, (b) $\theta = -2^\circ$, (c) $\theta = -4^\circ$ and (d) $\theta = -5^\circ$.

Fig. 59 Dislocation spacings for fcc:bcc interfaces vs. θ at three levels of lattice parameter ratio as calculated by computer modeling and the O-lattice method.

Fig. 60 Lattice image of $(111)_{\text{fcc}}$ and $(110)_{\text{bcc}}$ across interphase boundary of Cr precipitate in a Cu-0.3% Cr alloy. Boundary runs ca. left to right, has a significant projected width due to tilted beam conditions needed to image the lattice planes and is tilted away from the close-packed planes by at least 10° .

Fig. 61 Four Cr precipitates exhibiting fine dislocation structures. The magnification bar represents 10 nm. (a) 1.6 nm. array, $g = [111]_{\text{fcc}}$. (b) Lath, 2.5 nm. spacing, N-W orientation relationship, $g = [111]_{\text{fcc}}$. (c) 1.1 nm. array, $\theta = 3.5^\circ$; note ledge contrast. (d) Complex array, plus Moire pattern caused by surface film on foil, on a Pitsch-Schrader oriented precipitate; minimum spacing is 1.7 nm.

Fig. 62 N-W oriented lath. (a) Low magnification view showing characteristic nodule and planar boundaries; (b) Edge-on view displaying dislocations and possibly also ledges.

Fig. 63 Same precipitate as in Fig. 62, with foil tilted to reveal dislocation structure. (a) 2.5 nm. dislocation array. Note the array is not present (or visible) at the curved region of the boundary. A second set of fringes, spaced 1.5 nm. apart, is also visible. (b) Same precipitate further to the left. Note displacement of the thickness contour at the defects aligned at ca. 45° , showing that they are growth ledges.

Fig. 64 Same precipitate as in Fig. 62, imaged in five different g 's. Contrast observations consistent with $a/2[011]_{\text{fcc}}$, as predicted by O-lattice analysis.

Fig. 65 Another precipitate, viewed in six different reflections. Of the two sets of fringes, spaced 2.5 and 0.8 nm. apart, the former may represent structural ledges.

A. Publications Resulting in Whole or in Part From Research Supported by This Contract Since Its Inception

1. First Three Years (1973 - 1976)

1. Ferrite Allotriomorphs in Fe-C-X Alloys," Met. Trans., 12A, 1729 C. Atkinson, K.R. Kinsman and H.I. Aaronson, "Relative Growth Kinetics of Ledged and Disordered Interphase Boundaries," Scripta Met., 7, 1105 (1973).
2. K.C. Russell, M.G. Hall, K.R. Kinsman and H.I. Aaronson, "Nature of the Barrier to Growth at Partially Coherent FCC:BCC Boundaries," Met. Trans., 5, 1503 (1974).
3. K.C. Russell and H.I. Aaronson, "On the Driving Force for Growth of Grain Boundary Allotriomorphs by the 'Collector Plate' Mechanism," Scripta Met., 8, 559 (1974).
4. K.R. Kinsman, E. Eichen and H.I. Aaronson, "Thickening Kinetics of Proeutectoid Ferrite Plates in Fe-C Alloys," Met. Trans., 6A, 303 (1975).
5. H.I. Aaronson, "Observations on Interphase Boundary Structure," Jnl. of Microscopy, 102, 275 (1974).
6. M.R. Plichta and H.I. Aaronson, "Influence of Alloying Elements upon the Morphology of Austenite Formed from Martensite in Fe-C-X Alloys," Met. Trans., 5, 2611 (1974).
7. G.W. Lorimer, G. Cliff, H.I. Aaronson and K.R. Kinsman, "Analysis of the Composition of α_1 Plates Precipitated from β' Cu-Zn Using Analytical Electron Microscopy," Scripta Met., 9, 705 (1975).
8. H.I. Aaronson, M.G. Hall, D.M. Barnett and K.R. Kinsman, "The Watson-McDougall Shear: Proof That Widmanstatten Ferrite Cannot Grow Martensitically," Scripta Met., 9, 705 (1975).
9. M.G. Hall, H.I. Aaronson and G.W. Lorimer, "Considerations on a Martensitic Mechanism for the F.C.C. \rightarrow B.C.C. Transformation in a Cu-0.33 W/O Cr Alloy," Scripta Met., 9, 533 (1975).
10. M.R. Plichta, H.I. Aaronson and W.F. Lange III, "Application of a Rapid Chemical Polish to Preparation of High-Carbon Steel Specimens for Optical Microscopy," Metallography, 9, 455 (1976).
11. G.W. Lorimer, G. Cliff, H.I. Aaronson and K.R. Kinsman, "Reply to 'Comments on Analysis of the Composition of α_1 Plates Precipitated from β' Cu-Zn Using Analytical Electron Microscopy,'" Scripta Met., 9, 1175 (1975).
12. K.R. Kinsman and H.I. Aaronson, "A Critical Test of Two Theories of Non-IPS Geometric Surface Relief Effects Associated with Diffusional Phase Transformations," Met. Trans., 7A, 896 (1976).

13. H.I. Aaronson and K.R. Kinsman, "Growth Mechanisms of AuCu II Plates," *Acta Met.* 25, 367 (1977).
14. J.R. Bradley and H.I. Aaronson, "The Stereology of Grain Boundary Allotriomorphs," *Met. Trans.*, 8A, 317 (1977).
15. J.R. Bradley, J.M Rigsbee and H.I. Aaronson, "Growth Kinetics of Grain Boundary Ferrite Allotriomorphs," *Met. Trans.*, 8A, 323 (1977).

2. Second Three Years (1976 - 1979/1980)

16. H.I. Aaronson, "The Proeutectoid Reactions in Steel," *Materials Science and Engineering*, 25, 145 (1976).
17. K.R. Kinsman and H.I. Aaronson, "Reply to 'Discussion of 'A Critical Test of Two Theories of Non-ISP Geometric Surface Relief Effects Associated with Diffusional Phase Transformations','" *Met. Trans.*, 8A, 209 (1977).
18. H.I. Aaronson, "Discussion of 'On the Growth Kinetics of Plate-Shaped Precipitates in Aluminum-Copper and Aluminum-Gold Alloys' by Y.H. Chen and R.D. Doherty," *Scripta Met.*, 11, 731 (1977).
19. H.I. Aaronson, K.C. Russell and G.W. Lorimer, "Cessation of the Dislocation Splitting Mechanism for γ' Al-Ag Formation Above a Critical Temperature," *Met. Trans.*, 8A, 1885 (1977).
20. J.R. Bradley, H.I. Aaronson, K.C. Russell and W.C. Johnson, "Effects of Austenitizing Temperature on the Kinetics of the Proeutectoid Ferrite Reaction at Constant Austenite Grain Size in an Fe-C Alloy," *Met. Trans.*, 8A, 1955 (1977).
21. H.I. Aaronson, "Comments on 'Reply to Discussion on the Growth Kinetics of Plate-Shaped Precipitates,'" *Scripta Met.*, 11, 741 (1977).
22. H.I. Aaronson, J.K. Lee and K.C. Russell, "Diffusional Nucleation and Growth," 'Precipitation Processes in Solids', TMS-AIME, New York, p. 31 (1978).
23. G.J. Shiflet, J.R. Bradley and H.I. Aaronson, "A Re-examination of the Thermodynamics of the Proeutectoid Ferrite Transformation in Fe-C Alloys," *Met. Trans.*, 9A, 999 (1978).
24. J.M. Rigsbee and H.I. Aaronson, "The Interfacial Structure of the Broad Faces of Ferrite Plates," *Acta Met.*, 27, 365 (1979).
25. J.M. Rigsbee and H.I. Aaronson, "A Computer Modeling Study of Partially Coherent F.C.C.:B.C.C. Boundaries," *Acta Met.*, 27, 351 (1979).
26. H.I. Aaronson, "Mechanisms of Diffusional Growth," "Phase Transformations", Vol. I, p. II-1, The Institution of Metallurgists/Chameleon Press (April, 1979).
27. H.I. Aaronson, "An Emerging Viewpoint on Interphase Boundaries Developed During

Diffusional Phase Transformations," Proceedings of the (1977) International Conference on Metal Sciences--The Emerging Frontiers, Banaras Hindu University, Varanasi, India, Trans. Indian Institute of Metals, 32, no. 1, 1 (1979).

28. W.A.T. Clark, A. Guha, H.I. Aaronson and J.M. Rigsbee, "Discussion to a Series of Papers on the Structure on Interphase Boundaries in Brass," Scripta Met., 13, 1087 (1979).

29. J.R. Bradley and H.I. Aaronson, "Growth Kinetics of Grain Boundary Ferrite Allotriomorphs in Fe-C-X Alloys," Met. Trans., 12A, 1729 (1981).

3. Third Three Years

30. M. Enomoto and H.I. Aaronson, "On the Linearized Gradient Approximation for Diffusion-Limited Growth of a Spherical Precipitate," Jnl. App. Phys., 51, (1), 818 (1980).

31. H.I. Aaronson, "Orientation Relationships, Surface Reliefs and Growth Mechanisms of Diffusional FCC→BCC Transformations," Scripta Met., 14, 825 (1980).

32. J.K. Lee, Y.Y. Earmme, H.I. Aaronson and K.C. Russell, "Plastic Relaxation of Strain Energy of a Misfitting Spherical Precipitate - I. Ideal Plastic Behavior," Met. Trans., 11A, 1837 (1980).

33. G.J. Shiflet, H.I. Aaronson and J.R. Bradley, "On the Influence of Carbide Formation upon the Growth Kinetics of Proeutectoid Ferrite in Fe-C-X Alloys," Met. Trans., 12A, 1743 (1981).

34. H.I. Aaronson, "Role of Interfaces in Diffusional Nucleation and Growth," Encyclopedia of Materials Science and Engineering, Pergamon Press, in press.

35. J.R. Bradley, T. Abe and H.I. Aaronson, "Maintenance of Constant Carbon Concentration During Heat Treatment of Steel," Rev. Sci. Instrum., 53, 98 (1982).

36. T. Obara, G.J. Shiflet and H.I. Aaronson, "Influence of Interfacial Structure upon Carbide Precipitation at Austenite:Ferrite Boundaries in an Fe-C-Mo Alloy," Met. Trans., 14A, 1159 (1983).

37. M. Enomoto, H.I. Aaronson, J. Avila and C. Atkinson, "Influence of Diffusional Interactions Among Ledges on the Growth Kinetics of Interphase Boundaries," Proc. of an Int. Conf. on Solid-Solid Phase Trans., p. 567, TMS-AIME, Warrendale, PA (1983).

38. D.A. Smith, K.M. Knowles, H.I. Aaronson and W.A.T. Clark, "Misfit in F.C.C.-B.C.C. Interfaces," Proc. of an Int. Conf. on Solid-Solid Phase Trans., p. 587, TMS-AIME Warrendale, PA (1983).

39. M.G. Hall, J.M. Rigsbee and H.I. Aaronson, "Discussion to 'The Observation of Dislocation Arrays in Partially Coherent F.C.C./B.C.C. Boundaries in a Duplex Stainless Steel' by P.R. Howell, P.D. Southwick, R.C. Ecob and R.A. Ricks," Proc.

of an Int. Conf. on Solid-Solid Phase Trans., p. 595, TMS-AIME, Warrendale, PA (1983).

40. K.R. Kinsman and H.I. Aaronson, "Interfacial Structure of Co-Rich Precipitates in a Cu-Co Alloy," Proc. of an Int. Conf. on Solid-Solid Phase Trans., p. 599, TMS-AIME, Warrendale, PA (1983).

41. J.R. Bradley, G.J. Shiflet and H.I. Aaronson, "A Current View of Alloying Element Effects on Growth Kinetics of Proeutectoid Ferrite in Fe-C-X Alloys," Proc. of an Int. Conf. on Solid-Solid Phase Trans., p. 819, TMS-AIME, Warrendale, PA (1983).

42. G.J. Shiflet and H.I. Aaronson, "Discussion to 'Bainite: The Incomplete Reaction Phenomenon and the Approach to Equilibrium' by H.K.D.H. Bhadeshia," Proc. of an Int. Conf. on Solid-Solid Phase Trans., p. 997, TMS-AIME, Warrendale, PA (1983).

43. T. Obara, W.F. Lange III, H.I. Aaronson and B.E. Dom, "Prediction of TTT-Curves for Initiation of the Proeutectoid Ferrite Reaction in Fe-C Alloys," Proc. of an Int. Conf. on Solid-Solid Phase Trans., p. 1105, TMS-AIME, Warrendale, PA (1983).

44. G.J. Shiflet and H.I. Aaronson, "The Bainite Reaction," report on a Panel Discussion, Proc. of an Int. Conf. on Solid-Solid Phase Trans., p. 1581, TMS-AIME, Warrendale, PA (1983).

45. F.K. LeGoues, K. Chattopadhyay and H.I. Aaronson, "On the Application of Orientation Relationship Measurements to Distinguishing Between Different Nucleation Mechanisms," *Scripta Met.*, 17, 675 (1983).

46. J.M. Rigsbee, E.S.K. Menon, H.J. Lee and H.I. Aaronson, "On the Structure of the Broad Faces of Ferrite Plates," *Scripta Met.*, 17 1465 (1983).

47. D.A. Smith, W.A.T. Clark and H.I. Aaronson, "O-Lattice Analysis of Fcc-Bcc Interfaces," *Scripta Met.*, 17, 785 (1983).

48. A. Guha, H.I. Aaronson and W.A.T. Clark, "Structure of Interphase Boundaries in a Eutectic Co-Al Alloy," *Met. Trans.*, in press.

Manuscripts Under Review

(49) G.J. Shiflet and H.I. Aaronson, "The Incomplete Transformation (Stasis) Phenomenon in Fe-C-Mo Alloys," submitted to *Met. Trans.*

(50) G.J. Shiflet, J.R. Bradley and H.I. Aaronson, "Further Considerations on the Thermodynamics of the Proeutectoid Ferrite Reaction in Fe-C Alloys," submitted to *Met. Trans.*

(51) S.K. Liu, W.T. Reynolds, Jr., H. Hu, G.J. Shiflet and H.I. Aaronson, "Discussion of 'The Bainite Transformation in a Silicon Steel' by H.K.D.H. Bhadeshia and D.V. Edmonds", submitted to *Met. Trans.*

Manuscripts in Preparation

(52) K.B. Alexander and H.I. Aaronson, "Crossing of Precipitate Plates Formed by Diffusional Growth," to be submitted to *Met. Trans.*

- (53) M.G. Hall, J.M. Rigsbee and H.I. Aaronson, "Application of the O-Lattice Calculation to FCC/BCC Interfaces," to be submitted to *Acta Met.*
- (54) M.G. Hall, U. Dahmen and H.I. Aaronson, "The Fine Structure of FCC/BCC Boundaries in a Cu-0.3% Cr Alloy," to be submitted to *Acta Met.*
- (55) K. Chattopadhyay and H.I. Aaronson, "Interfacial Structure and Crystallography of Transformations in β' and β Cu-Zn Alloys. I. Isothermal Formation of α_1 Plates from β' ," to be submitted to *Acta Met.*
- (56) K. Chattopadhyay and H.I. Aaronson, "Interfacial Structure and Crystallography of Transformations in β' and β Cu-Zn Alloys. II. Martensitic Formation of α_1 Plates from β' ," to be submitted to *Acta Met.*
- (57) K. Chattopadhyay and H.I. Aaronson, "Interfacial Structure and Crystallography of Transformations in β' and β Cu-Zn Alloys. III. Isothermal Formation of α Rods from β and β' ," to be submitted to *Acta Met.*
- (58) T. Abe, H.I. Aaronson and G.J. Shiflet, "Effects of Interphase Boundary Precipitation upon the Growth Kinetics of Grain Boundary Ferrite Allotriomorphs in an Fe-C-V Alloy," to be submitted to *Met. Trans.*
- (59) H. Tsubakino and H.I. Aaronson, "Morphology of Ferrite and Carbide At and Below the Bay of an Fe-C-Mo Alloy," to be submitted to *Met. Trans.*

B. Personnel and Supplemental Support Situations

J.R. Bradley and G.J. Shiflet received their Ph.D. degrees in Metallurgical Engineering, both from Michigan Technological University, with the support of this contract. In the case of Dr. Shiflet, his tuition and stipend were supplied at Michigan Technological University by a Republic Steel Corporation Fellowship and at Carnegie-Mellon University by a NSF grant awarded the P.I., Prof. H.I. Aaronson. Graduate students W.T. Reynolds, Jr. and Takashi Tanaka subsequently participated in the research operations supported by this contract. Mr. Tanaka has his tuition and stipend furnished by the Nippon Steel Corporation. During the final months of this contract, Mr. Shih-Kai Liu of Southwestern Jiaotong University and Mr. Chi-Kun Shui of Chongqing University, both in the People's Republic of China, worked on research funded by this contract.

C. The Proeutectoid Ferrite and Bainite Reactions in Fe-C-X Alloys

We note at the outset of this section the extensive and still growing controversies as to the nature of the bainite reaction (5,44,45). We further note that these arguments have

become so tangled that persons taking different sides not infrequently find themselves discussing different phase transformations phenomena! Throughout this proposal we shall avoid entanglement in definitional problems--though the P.I. is not noted for avoidance of same!--but will instead attempt to provide clear description of the particular phenomena under investigation and then present our results, both experimental and theoretical, arising from our studies of them, all without attempting to say which of these "deserve" the label "bainite".

1. The Incomplete Transformation Phenomenon in Fe-C-Mo Alloys

a. Introduction

This research, now complete, constituted the main portion of the Ph.D. thesis of Gary J. Shiflet, who is presently Assistant Professor in the Department of Materials Science, University of Virginia. Dr. Shiflet's tuition and stipend were provided by a Republic Steel Corporation Fellowship while he was at Michigan Technological University and by NSF during a final year at CMU; however, his research expenditures at MTU and the participation of the P.I. were funded by ARO.

At the time the previous renewal proposal was written, this work was still in a relatively early stage. Accordingly, a summary of the entire program will be presented here.

Research on the incomplete transformation phenomenon dates back at least 50 years, to the work of Wever and co-workers (46-49) in Germany. These studies were pursued in the Soviet Union (50-52), England (53,54) and the U.S. (55-57) for about 20 years--and then were largely ignored until a recent revival of interest in them. The position developed as a result of the early research efforts is readily summarized (19, 20):

(i) Incomplete transformation is most pronounced at temperatures just below the bay in the TTT-curve for the initiation of transformation in alloy steels containing concentrations of carbide-forming alloying elements sufficient to separate completely the pearlite and bainite reactions.

(ii) In such steels, the fraction of the austenite matrix isothermally transformed to bainite reaches a maximum value which approaches zero as the bay temperature (later termed the "kinetic B", to distinguish this definition, generated on the basis of the overall reaction kinetics

definition of bainite, from the B_s temperatures derived from the microstructural (the eutectoid temperature) and the surface relief (Widmanstatten start-temperature) definitions (5) is approached. The austenite remaining untransformed after cessation of the bainite reaction may remain quiescent for a considerable period of time before transformation resumes, and goes to completion, presumably by another mechanism. (Hence incomplete transformation is sometimes termed "stasis"; this term will be used here, primarily for the sake of brevity.)

(iii) With decreasing reaction temperature below the kinetic- B_s , the maximum amount of austenite which can decompose to bainite increases, reaching 100% and remaining at this level (if the kinetics of carbon diffusion in austenite remain sufficiently high) until the martensite transformation intervenes.

(iv) Steels not exhibiting stasis do so only because the pearlite and bainite reactions overlap. Thus incomplete transformation/stasis is considered to be a wholly general phenomenon in the decomposition of austenite at intermediate reaction temperatures.

In 1968, Boswell, Kinsman and Aaronson (17)* made an optical microscopy study

*This research was unfortunately not published. However, Prof. Shiflet and the P.I. are presently modernizing the calculations involved and hope to have both this paper, and a companion one on the influence of alloying elements upon the W_s temperature, ready for submission to Met. Trans. within the coming year.

of stasis in Fe-C-2 W/O Mo alloys containing from 0.05 to 0.26 W/O C. TTT-curves for the beginning of transformation were determined, thickening kinetics of grain boundary ferrite allotriomorphs were measured and fraction transformed vs. time was evaluated by means of point counting (58), in preference to the easier but less reliable physical properties methods such as dilatometry, magnetometry, resistometry, etc. usually used in previous investigations. Boswell et al proposed a more precise definition of stasis: cessation of transformation when the fraction transformed to ferrite is significantly less than that permitted by application of the Lever Rule to the $\alpha + \gamma$ region extrapolated to the transformation temperature. On this basis, they found that stasis does not exist in any of the alloys they studied. They also discovered a bay or minimum in plots of the parabolic rate constant, α , for allotriomorph thickening vs. temperature; in each of their alloys, this bay was centered at about the temperature of the bay in the TTT-curve for the initiation of the ferrite/bainite reaction. These results indicated that, even in alloys wherein the

bainite (kinetically defined) and pearlite reactions are widely separated, the stasis phenomenon is far less general than had been previously believed. Hehemann (59) and Breyer (60) assured us privately that the phenomenon's existence has been confirmed by quantitative metallography--but in multiply alloyed steels, such as SAE/AISI 4340, rather than in Fe-C-X alloys. The widespread use of such steels (or of nominally Fe-C-X alloys which also contain, as trace impurities, significant proportions of other elements) in the older investigations may well bear much of the "blame" for the apparently exaggerated generality ascribed to stasis; the use of indirect techniques for measuring the progress of transformation is likely responsible for a good proportion of the remainder.

Thus the major objective of Shiflet's Ph.D. thesis research was to extend the Boswell et al studies to alloys containing larger proportions of Mo in an effort to ascertain whether or not stasis really is absent in this system whose deep-bayed TTT-diagrams seem so strongly to "invite" its occurrence in accord with the kinetic definition of bainite. Evaluation of the temperature-composition region of stasis, if it appeared, and characterization of growth kinetics within and without the stasis region were other major program objectives.

b. Experimental Procedures

A total of 19 alloys (17 of which were a gift of the Climax Molybdenum Co. Research Laboratories through Dr. M. Semchyshen and the other two a gift of the Ford Scientific Laboratories through Dr. K.R. Kinsman), containing an average of 0.15, 0.20 or 0.25 W/O C and levels of Mo ranging from ca. 2-1/4 to 4-1/4 W/O, were used in this investigation. The Boswell studies (TTT-curves, fraction transformed vs. time and allotriomorph thickening kinetics) were repeated in these alloys--but this time extensive TEM studies of representative alloys were made as well. These alloys typically contained 0.00X W/O, and sometimes less, of such standard impurity elements as Si, Mn, Ni, Cr, Cu, P and S. Following homogenization for 3 days at 1300°C, individual specimens were austenitized for 30 min. at 1300°C in a graphite-deoxidized, argon-protected BaCl₂ salt bath (61), isothermally reacted for times as long as six days at many temperatures (sometimes at intervals as small as 10°C) in the vicinity of the bay and then quenched in iced brine.

C. Results

Fig. 1 presents the portion of the TTT-curve for initiation of transformation determined and thus indicates the temperature regions studied, and also provides the Mo concentrations (in W/O) in the alloys used. Even the most dilute alloys studied are seen to possess a deep bay in the vicinity of the kinetic- B_s temperature.

Berry and Honeycombe (62) studied the microstructure of Fe-C-Mo alloys within the composition range of this investigation. Whereas their studies were conducted on specimens reacted at 650°C and above, ours were made on specimens reacted at from 650° down to 560°C. The carbide morphologies observed are essentially the same as those observed by Berry and Honeycombe. The following summarizes the observations made on both ferrite and carbide morphologies by optical and electron microscopy during the present study:

(i) The morphology of the ferrite phase is overwhelmingly grain boundary allotriomorphs (Fig. 2).

(ii) At temperatures below that of the bay, the morphology of the ferrite phase became so degenerate that no further measurements of growth kinetics of any type could be made in the present alloys. (This finding is illustrated and further considered in the next sub-section, describing the investigation by Tsubakino of ferrite and carbide morphologies at sub-bay temperatures in a representative Fe-C-Mo alloy.)

(iii) All ferrite observed with both thin foil and extraction replication electron microscopy contained carbides. As Berry and Honeycombe found at higher temperatures, two types of carbide array, dispersed in ferrite and nucleated at α : γ boundaries, were present: interphase boundary carbides (Fig. 3) and fibrous carbides (Fig. 4). Approximately equal proportions of the two types appeared in the higher Mo alloys. At the higher temperature in the low Mo alloys the fibrous structure predominated; however, some interphase boundary carbides were always present.

(iv) The two types of carbide morphology could not be distinguished with optical microscopy--and it was impractical to use TEM to measure the thickening kinetics of allotriomorphs because the scale of the microstructure was so coarse. Fortunately, the thickening kinetics of allotriomorphs containing these carbide morphologies were approximately the same (Fig. 5).

(v) Selected area electron diffraction patterns demonstrated that both fibrous (Fig. 6) and interphase boundary (Fig. 7) carbides are Mo_2C . Precipitation of M_6C , apparently at austenite grain boundaries, was observed in only two alloys, M and R, and does not appear to have affected significantly their transformation kinetics.

All curves of fraction transformed to ferrite + associated carbides (necessarily determined with optical microscopy) either went to completion (Fig. 8) or were clearly in a rising mode (Fig. 9) when measurements were terminated. Even when little transformation had taken place after the longest reaction time used (six days), there was no realistic indication of stasis (Fig. 9).

A large amount of data on the growth kinetics of (carbide-containing) grain boundary ferrite allotriomorphs was obtained. Whereas previously reported data of this type determined on Fe-C and Fe-C-X alloys invariably yielded a single straight line when the logarithm of the half thickness ($S/2$) was plotted against the logarithm of the isothermal reaction time (instead of the more appropriate, but little different, growth time), the present data fell into four categories when so plotted: Type I -- the single straight line (higher reaction temperatures and low to medium C and Mo concentrations); Type II -- two straight lines, with the second line having the higher slope (at somewhat lower temperatures, in all alloys studied); Type III -- three straight lines, the second (middle) one having the smallest slope and the third one the largest (at $> 3\frac{3}{4}\%$ Mo); and Type IV -- also three straight lines, but with the middle one having a zero slope (when % C > 0.25 and % Mo $> 3\frac{3}{4}\%$). Fig. 10 presents experimental data on an Fe-0.20%C-4.00% Mo alloy which exhibits all four types of behavior. Fig. 11a shows these types schematically. The data are summarized in Figs. 11b, c and d by indicating the C-Mo regions in which a given type of behavior is found at the bay temperature (11b), 20°C above the bay (11c) and 40°C above the bay (11d). Since the bay temperature decreases with increasing C and Mo concentrations (Fig. 1), these plots normalize the data to the bay temperature. They show that the higher type numbers of growth behavior become more important the closer the reaction temperature is to that of the bay.

Special attention is called to type IV growth. The middle stage thereof may be properly termed "growth stasis". Recall that complete cessation of transformation, which we now describe as "transformation stasis", was not found in any of the alloys utilized. Metallographic

observations indicated that the middle stage of type IV behavior occurs when coverage of the austenite grain boundaries by allotriomorphs is still quite incomplete; only during the third stage are the grain boundaries essentially fully transformed. Hence one can now state that a prerequisite for transformation stasis is the initiation of middle stage type IV growth at those areas of the austenite grain boundaries where ferrite nucleation took place last prior to entrance into third-stage type IV growth of the first formed allotriomorphs. Transformation stasis thus appears to be essentially a growth phenomenon (rather than one based upon nucleation, as has been recently alleged without direct experimental support (63)).

Least squares analyses of the slopes of the various stages of growth in the four types reveals some pronounced trends--as well as considerable scatter. For type I and the first stage of the other types of growth, the time exponent varies from 0.1 to 1, though a trend toward values in the 0.5 - 1 range is apparent in the first stage of types III and IV. The exponent during the second stage of type II and the third stage of types III and IV tends toward unity, particularly in the case of type III. The second stage of type IV has, of course, an essentially zero exponent, whereas the corresponding stage of type III has an exponent ranging from 0.2 to 0.5.

d. Discussion

In view of the numerous phenomena uncovered during this study, which was apparently the first to incorporate growth kinetics measurements in the temperature region of the bay, attempts were made to consider the entire range of observations rather than only the growth stasis results. In order to compare the measured growth kinetics with the predictions of the various models used, the data were fitted to both $t^{1/2}$ and to t^1 time laws, even though these laws were obviously not always appropriate. Comments will be offered later on the time laws actually operative. For present purposes, though, it should be noted that, the distortion of the growth kinetics produced by force fitting to inappropriate time laws is minor relative to the differences in the predictions of the various models for the growth processes. Figs. 12a-d are sample plots of $\log S/2$ vs. \log reaction time for types I, II, III and IV growth. The growth kinetics data for the particular steels and reaction temperatures used to illustrate each type are plotted as scatter bands, for both $t^{1/2}$ and t^1 growth, on each graph. The various models for

allotriomorph thickening considered and the conclusions drawn from comparing them with the measured kinetics are now summarized.

(i) Planar Growth of Ferrite Controlled by Volume Diffusion of Carbon in Austenite

This model ignores the precipitation of Mo_C in association with ferrite and assumes, on the basis of results obtained when X is not so strong a carbide-former (61), that paraequilibrium conditions obtain during growth. It was investigated to secure one type of upper limit to allotriomorph thickening kinetics. The calculated $S/2$ values plotted in Fig. 12 (denoted as "Planar- D_{Vc}^γ ") are seen to exceed the $t^{1/2}$ version of their measured counterparts usually by ca. two orders of magnitude, but in some situations by more than four orders of magnitude. Since the allotriomorphs measured have undergone extensive lateral impingement, they have a nearly zero aspect ratio. Accordingly, the Atkinson (64) analysis for the growth kinetics of planar boundaries, which takes account of the influence of the variation of the diffusivity of carbon in austenite with carbon concentration through a numerical technique, was employed to calculate growth kinetics with Hillert-Staffansson (65) paraequilibrium boundary conditions.

(ii) Planar Growth by Volume Diffusion of Mo in Austenite

Since $D_{\text{Mo}}^\gamma \ll D_{\text{C}}^\gamma$, this is a binary Fe-Mo diffusion problem. Inasmuch as this model requires bulk partition of Mo between austenite and ferrite, which does not obtain experimentally (66), it cannot be correct. However, this model does provide one form of lower limit to the growth kinetics. Figs. 12a-d show that with progress from type I through type IV growth patterns the thicknesses calculated from this model ("Planar- $D_{\text{V}_{\text{Mo}}}^\gamma$ ") approach more closely the experimental thicknesses. In Fig. 12d, disagreement between calculated and measured thicknesses average less than an order of magnitude during the interval of growth stasis. Hence the mechanism actually controlling the thickening of carbide-containing allotriomorphs evidently works nearly as slowly as the slowest possible diffusion process which might be operative in this system in the absence of an interfacial barrier to growth.

(iii) Growth of the Fibrous Structure by Volume Diffusion of Mo Through Austenite

This is the first realistic mechanism to be evaluated. A model similar to that for the edgewise growth of pearlite (67) was employed, but with appropriate modifications for the replacement of carbide plates by the fibrous carbide morphology. The fibers were modeled as cylinders. Volume diffusion of Mo from ferrite to the Mo_2C cylinders through austenite was considered as taking place from the outer to the inner wall of a hollow cylinder (68), where the outer radius reflects the average cross-sectional area of ferrite assignable to each fiber and the inner radius is that of the average fiber. Using a Fick's First Law type of flux balance analysis and the maximum growth rate assumption, the edgewise growth rate of the fibrous structure is given by

$$(1) \quad G_v = \frac{(\pi)^{1/2} D_v^\gamma (y_\gamma^{\gamma\alpha} - y_\gamma^{\gamma C})}{4b' L^{3/2} \ln(L^{-1/2}) (y_C^{C\gamma} - y_\gamma)}$$

where D_v^γ = volume diffusivity of Mo in austenite, b' = one-half the average inter-fiber distance, $L = (y_\gamma - y_\alpha^{\alpha C})/(y_C^{\alpha C} - y_\gamma)$, and the following y's are atom fractions of Mo: $y_\gamma^{\gamma\alpha}$ - at $\gamma/(\gamma + \alpha)$ phase boundary, $y_\gamma^{\gamma C}$ - at $\gamma/(\gamma + \text{Mo}_2\text{C})$ phase boundary, y_γ - in the alloy prior to transformation, $y_\alpha^{\alpha C}$ - at $\alpha/(\alpha + \text{Mo}_2\text{C})$ phase boundary, $y_C^{\alpha C}$ - at $\text{Mo}_2\text{C}/(\text{Mo}_2\text{C} + \alpha)$ phase boundary and $y_C^{\gamma C}$ - at $\text{Mo}_2/(\text{Mo}_2\text{C} + \alpha)$ phase boundary. The Hillert-Staffansson (65) analysis was used to compute phase boundary compositions; b' was taken from experimental measurements. Calculated values of $S/2$ --denoted as "Fibrous- $D_{v\text{Mo}}^\gamma$ "--are plotted in Figs. 12a-d. For type I growth the calculated values lie below the experimental ones; with increasing type number, however, increasingly good agreement is achieved except during the stasis portion of type IV growth. Other discrepancies, though, include failure to predict the four types of growth and approximation of a t^1 growth law only in the final stage of types II, III and IV growth. Hence this mechanism does not appear to be the primary one for the growth of the fibrous structure in the bay region.

(iv) Growth of the Fibrous Structure by Interphase Boundary Diffusion of Mo

Since the average reaction temperature used lies at ca. $0.5 T_m$, interphase boundary diffusion is a plausible transport mechanism for the diffusion of Mo to Mo_2C fibers. The apparently higher energy of austenite:ferrite boundaries in fibrous than in interphase boundary

carbide structures (1,2) should improve the feasibility of this mechanism. The D_v -control analysis of fibrous growth summarized in the preceding sub-sections is readily modified for the interphase boundary diffusion case:

$$(2) \quad G_b = \frac{D_b \delta (y^{\gamma_a} - y^{\gamma_c})}{6(b')^2 L \ln(L^{-1/2}) (y_c^{\gamma_c} - y^{\gamma})}$$

where D_b = the austenite:ferrite boundary diffusivity of Mo and δ = thickness of austenite:ferrite boundaries. Values calculated from this analysis are shown in Fig. 12, denoted as "Fibrous- $D_{b_{Mo}}$ ". The calculated half-thicknesses are seen to be usually four or more orders of magnitude higher than the experimental ones. Hence this mechanism, by itself, cannot provide an accounting for the experimental growth kinetics.

(v) **Growth of Interphase Boundary Carbides and of The Interphase Boundary Carbide Structure by Volume Diffusion of Mo in Austenite or Ferrite**

The growth mechanism of the interphase boundary carbide structure is very different from that of the fibrous carbide structure. Essentially following the description of Honeycombe (1,2), the growth mechanism is highly non-cooperative rather than fully cooperative (69) as in the case of the fibrous structure. The basis of the interphase boundary carbide structure is the thickening of grain boundary ferrite allotriomorphs predominantly by the ledge mechanism. Carbides nucleate and grow as isolated crystals (cylinders in the case of Mo_2C (62)) on the immobilized partially coherent broad faces of the ledges. Hence a sheet or layer of carbides formed at a given broad face is exposed to austenite only until it is overrun by the passage of the next ledge.

Although the interphase boundary carbide structure has been the subject of many careful morphological and crystallographic investigations (1,2), the growth kinetics of this structure have so far been considered only in qualitative fashion. Accordingly, some aspects of the growth of Mo_2C crystals at the broad faces of ferrite ledges will be examined before resuming consideration of the influence of carbides on the growth of ferrite.

Using the Jones-Trivedi (70) equation for the lateral migration rate of ledges and TEM-measured values of average ledge height and inter-ledge spacing, the average time at which a

given broad face of a ledge is exposed to austenite was calculated at five different temperatures in three alloys. Radii of cylindrical interphase boundary carbides were also measured. The radii attained by carbide cylinders after the same times, assuming control by Mo diffusion, first in austenite and then in ferrite, were calculated from a relationship due to Zener (71). Agreement usually within an order of magnitude was obtained between calculated and measured radii assuming growth into austenite; calculated values assuming growth into ferrite were up to an order of magnitude higher. The latter values, however, are probably overestimates since they do not take account of depletion of Mo supersaturation in ferrite by formation of the previous sheet of carbide cylinders.

The hypothesis that the growth of carbide cylinders is assisted by diffusion of Mo along the broad faces of ferrite ledges was investigated through an appropriate modification of the analysis for the "collector plate" mechanism for the growth of grain boundary allotriomorphs (32,72):

$$(3) \quad G = \frac{2y_{\gamma}^{\gamma C} D_b \delta (y_{\gamma_r}^{\gamma C} - 1)t^{-1/2}}{(1 - (2)^{1/2}/2)k^2 (y_C - y_{\gamma_r}^{\gamma C})}$$

where

$$(4) \quad k = \frac{2A(D_{V_{Mo}}^{\gamma})^{1/2} (y_{\gamma} - y_{\gamma_r}^{\gamma C})}{\pi^{3/2} r (y_C - y_{\gamma_r}^{\gamma C})}$$

where D_b is here the diffusivity of Mo along partially coherent austenite:ferrite boundaries, assumed equal to the grain boundary diffusivity (23), A is the area of such boundary assigned to an individual carbide cylinder as a collector plate, $y_{\gamma_r}^{\gamma C}$ is the capillarity-corrected Mo concentration in austenite at the surface of a carbide cylinder and t is the growth time. The cylinder radii thus calculated are ca. five orders of magnitude higher than the radii calculated assuming volume diffusion in ferrite and six orders of magnitude larger than those computed on D_v -controlled growth into austenite. It thus appears that, a previous suggestion (73) to the contrary, the collector plate mechanism probably does not contribute significantly to the growth of interphase boundary carbides. The relatively low diffusivity of Mo along the partially coherent broad faces of ferrite plates as compared with that along disordered-type grain or interphase boundaries is probably responsible for the gross overestimates of the growth kinetics of carbides achievable by the collector plate mechanism.

We next consider the question of whether or not the interphase boundary carbides continue to grow within ferrite after passage of the next ledge has terminated their contact with austenite. In the present and in previous studies (73,74), qualitative observations indicated that no further growth occurs. Assuming that the ferrite retains its original Mo concentration as an upper limiting approximation, an equation developed by Ham (75) for the unprecipitated fraction of excess solute vs. time for prolate ellipsoids of constant aspect ratio was used to calculate times required for a 90% decrease in supersaturation. These times were found to lie within the scatterbands for the exposure of Mo_2C to austenite. Hence sufficient time was available for each sheet of carbides to deplete almost completely the supersaturation of the ferrite against which it formed even if this ferrite had managed to retain its original supersaturation. Since this calculation indicates that the inverse is more nearly correct, it seems clear that negligible driving force remains for further growth of interphase boundary carbides by the time that the next ledge has enclosed them wholly within ferrite--in agreement with qualitative observations of the microstructure.

Finally, the ledgewise growth of ferrite in the presence of interphase boundary carbides is considered on the hypothesis that this process is controlled by the volume diffusion of Mo from the risers of the ledges through austenite to the carbides formed on the broad faces of the ledges. The Jones-Trivedi equation (70) for ledgewise growth can be adapted to this situation in semi-quantitative fashion by simply replacing the Mo concentration in the untransformed bulk austenite with that corresponding to the $\gamma/(\gamma + \text{Mo}_2\text{C})$ phase boundary. The results obtained are plotted in Fig. 12 as "Ledge- $D_{\text{V}_{\text{Mo}}}^{\gamma}$ ". As does the planar, $D_{\text{V}_{\text{Mo}}}^{\gamma}$ -controlled model, this one also yields $S/2$ values lying below the experimental data for all four types of growth. Although the agreement improves with progression through successive growth types, the difference between calculated and experimental values becomes no smaller than two orders of magnitude.

(vi) Fibrous Growth with D_{b} Transport Inhibited by SDE upon Carbon Transport Through Austenite

In this sub-section the mechanism considered to be operative for the growth of fibrous carbide structures in the alloys studied is presented. The mechanism proposed for growth of the interphase boundary carbide structure will be described in the next subsection.

From the considerations of preceding subsections dealing with the growth kinetics of the fibrous carbide structure, the most likely option remaining is Mo diffusion to the Mo_2C fibers along the advancing austenite:ferrite boundaries, with the motion of these boundaries controlled, and greatly slowed down, by a particularly potent SDE. Hence growth of the fibrous carbide structure is suggested to be controlled by the volume diffusion of carbon through austenite, albeit under the greatly reduced driving force allowed by the SDE. In section II-C-3, the results of an evaluation of the importance of various factors affecting the migration kinetics of austenite:ferrite boundaries will be presented. Fig. 23, showing the ratio of the parabolic rate constant experimentally measured to that calculated assuming paraequilibrium growth of a planar, disordered boundary as a function of reaction temperature for Fe-C-X alloys, most of which contain ca. 3 A/O X and ca. 0.5-0.6 A/O C, is advanced as an empirical evaluation of the relative strength of the SDE produced by a number of substitutional solutes; the SDE is considered stronger the further this ratio falls below unity. Mo is thus shown to produce an especially effective SDE, in support of the basic postulate underlying the mechanisms to be developed in this and the next subsection.

In order to explain the four types of growth behavior observed, it is necessary to propose two additional postulates. One is that the kinetics of Mo adsorption at austenite:ferrite boundaries are gradual, with the steady state value not being achieved (in types II-IV growth) until the end of the first stage. The second is that the steady state concentration of Mo in disordered-type austenite:ferrite boundaries increases with decreasing temperature in a given alloy (4,5).

Now consider the first stage of allotriomorph thickening when type IV growth behavior prevails, i.e., near the bay temperature in the higher Mo alloys studied. As Mo is accumulated at austenite:ferrite boundaries, the driving force for growth is diminished. If growth takes place by the ledge mechanism, the time exponent will fall below unity; if disordered boundary motion predominates, the exponent will diminish below 0.5; and in both cases the exponent obtained from linearizing a $\log(S/2)$ vs. $\log(\text{time})$ plot will be only an apparent one. The finding that the experimental exponent lies between 0.5 and 1 more often than below 0.5 during first stage growth of all four types indicates behavior different than is usually found in Fe-C and Fe-C-X alloys, where the 0.5 exponent had heretofore seemed general (4,6,14,16). Since the measurement

technique used yields the maximum thickening kinetics (16), it is suggested that more extensive adsorption of Mo at the broad faces of allotriomorphs which have larger proportions of disordered area has preferentially diminished the growth kinetics of this "group" of allotriomorphs, and has instead favored allotriomorphs at which the principal facet plane is nearly parallel to the grain boundary plane; such allotriomorphs must thicken predominantly by the ledge mechanism.

The number and size of ferrite allotriomorphs present during first stage thickening was too small to permit their examination with TEM. Optical microscopy suggests, though, that at least initially the density of carbides associated with them is relatively small, since allotriomorphs at this stage of transformation tend to be light etching. Hence it is also proposed that carbides may not interfere with the SDE during the first stages of growth.

In section II-C-4, the current status of SDE theory is described. The essential point required here is that Mo adsorption at disordered-type austenite:ferrite boundaries is expected to diminish the activity of carbon in bulk austenite in contact with the boundary region below its paraequilibrium $\gamma/(\alpha+\gamma)$ value because under paraequilibrium conditions equality of Mo partial molar free energies in the two bulk phases cannot be established; the strong reduction in the activity of carbon in austenite by Mo ensures this consequence of the resulting non-equilibrium Mo segregation.

During stage two of type IV growth, even disordered austenite:ferrite boundaries become immobile because the SDE, operating at peak effectiveness, eliminates the difference in carbon activity between the "surface" of austenite grains in contact with disordered austenite:ferrite boundaries and their interior. As a result of the presence of carbides at the austenite:ferrite boundaries, however, departure from paraequilibrium occurs more rapidly than would otherwise be feasible; an estimate of the Mo transport kinetics, based upon Mo diffusion through austenite (76), yields times within an order of magnitude of the typical growth stasis or stage two/type IV interval.

Stage three of type IV growth should then begin, with the carbon activity gradient in austenite now restored. This gradient, from $\gamma:\alpha$ to $\gamma:\text{Mo}_2\text{C}$ boundaries, will still be affected by the SDE, but less than during stage one growth. Lateral diffusion of Mo to the Mo_2C fibers will ensure that paraequilibrium conditions are not regained at austenite:ferrite boundaries;

diffusion of carbon over distances which are independent of growth time (and the order of a fraction of the average inter-fiber spacing) will guarantee a constant growth rate, i.e., a t^1 growth law, as experimentally observed.

At somewhat higher reaction temperatures or lower Mo concentrations, the SDE caused by Mo segregation to austenite:ferrite boundaries will be smaller. Hence the second stage of growth, though slow, will still proceed with finite kinetics, i.e., the type III growth pattern. But again, the second stage should continue until sufficient departure from paraequilibrium at α : γ boundaries has occurred to permit the development of the 3rd stage of growth. A further increase in reaction temperature or decrease in Mo or C concentration in the alloy can make a distinct interval for the loss of paraequilibrium unnecessary and thus permit a direct transition from the initial to a more rapid second stage of growth. This is the type II pattern. Finally, at still higher temperatures or in more dilute alloys, the SDE will be sufficiently reduced so that a single growth law, i.e., type I, will be continuously maintained, with a $t^{1/2}$ growth law.

(vii) Interphase Boundary Carbide Structure Growth with Carbon Transport Through Austenite Inhibited by SDE

Unlike the fibrous carbide structure, the growth kinetics of the interphase boundary carbide structure do not directly involve carbide precipitation. Our analyses have shown that sufficient time is available for this to take place between the passage of successive ledges. Hence thickening kinetics of ferrite allotriomorphs containing interphase boundary carbides are controlled by the formation and lateral movement of ledges. The driving force for this process is somewhat changed by the presence of carbides, from the difference in carbon concentrations between the extrapolated paraequilibrium Ae_3 and the carbon concentration in the bulk alloy to the difference between the extrapolated paraequilibrium Ae_3 and the extrapolated γ /(γ + Mo_2C) phase boundaries. The circumstance that the thickening kinetics calculated on this basis are again orders of magnitude higher than those measured experimentally is again ascribed to the very strong SDE produced by Mo, varying with alloy composition and temperature as in the case of fibrous carbide growth.

The mechanisms finally arrived at for both fibrous carbide and interphase boundary carbide growth are thus critically dependent upon SDE. While the carbides certainly do play a role in the growth process of these structures, particularly in the fibrous carbide structure, the foregoing

analysis indicates that it is not really central. It is now apparent that future research in this portion of our program should be focused upon the SDE per se, with special attention being paid to this effect in alloys where it is strong but carbide precipitation (which is also encouraged by alloying elements which reduce the activity coefficient of carbon in austenite) is either absent or infrequent. Not until a quantitative theoretical analysis of the SDE per se has been developed will it be possible to derive useful formal analyses of the mechanisms proposed for the growth of the interphase boundary and fibrous carbide structures.

2. Ferrite and Carbide Morphologies At and Below the Bay of a Representative Fe-C-Mo Alloy

a. Introduction

This program was undertaken by Dr. Harushige Tsubakino of the University of Osaka Prefecture, Osaka, Japan, during a 14 month visit with the P.I.'s group.

Remarkably little information and still less interpretation thereof are available on the morphology of ferrite--or shall we say the ferritic component of bainite--at reaction temperatures in the vicinity of and below that of the bay in the TTT-diagram of alloy steels exhibiting such behavior. No previous TEM study of the morphology and distribution of the carbides associated with the bay region and lower reaction temperatures appears to have been made.

b. Experimental Procedures

A combined optical and TEM investigation was undertaken to provide both sets of information on a representative Fe-C-Mo alloy, containing 0.19% C and 2.30% Mo. The bay temperature of this alloy lies between 610° and 615°C; studies were conducted from 625° down to 475°C; the M_s temperature was estimated as 440°C (77).

c. Results

Fig. 13 illustrates the very sharp variation of proeutectoid ferrite morphology with reaction temperature at early stages of reaction, as observed with optical microscopy. Just above the bay, grain boundary allotriomorphs predominate (Fig. 13a). At the bay, sawteeth appear (Fig. 13b). Just below the bay, these evolve into irregularly shaped

sideplates (Fig. 13c). At a slightly lower temperature, the degeneracy of the ferrite morphology has become extreme (Fig. 13d). Even 20°C lower, the path followed by ferrite plates is tortuous (Fig. 13e). A further reduction in reaction temperature, by 25°C, is required to restore a normal Widmanstatten sideplate morphology, in whose development sympathetic nucleation (15,78) obviously plays an important role (Fig. 13f). The main effect of a still lower reaction temperature is to increase further the proportion of ferrite plates which appear to be sympathetically nucleated (Fig. 13g).

Fig. 14 illustrates these microstructures at later reaction times. Although ferrite continues to be most degenerate at 595°C, this effect is no longer so pronounced. The rapidity with which the interiors of ferrite crystals are etched also varies appreciably with temperature, with the darker etching structures indicative of the presence of higher densities of carbides.

TEM observations were directed toward the carbide component of the microstructure and exhibited equally complex patterns. At temperatures above that of the bay, the observations essentially duplicated those of Berry and Honeycombe (62). Fibrous carbide and interphase boundary carbide structures again predominated. Selected area electron diffraction (SAD) showed that the carbides in both are Mo_2C and that the orientation relationships between ferrite and carbides are of the Pitsch-Schrader type (79,80) for interphase boundary carbides and of the Burgers (81) type for fibrous carbides. The scale of both types of carbide structure is very small; typically, the largest dimension of the interphase boundary carbides and the diameter of the fibrous carbides is 2-5 nm.; the spacing between carbides is 10-20 nm. for both morphologies. At the austenite grain boundaries, $(\text{Fe},\text{Mo})_6\text{C}$, i.e., M_6C carbides developed as grain boundary allotriomorphs. This observation extends downwards the temperature range in which these carbides appear by 100°C relative to the observations of Berry and Honeycombe (62) and downwards in Mo concentration by 1.5 W/O from Shiflet's work described in the preceding subsection. Dark field observations revealed that M_6C allotriomorphs form first at austenite grain boundaries; grain boundary ferrite allotriomorphs then form round them and extend along the austenite grain boundaries; a zone denuded of carbides surrounds the M_6C allotriomorphs. Subsequently, fibrous and interphase boundary carbides develop at the austenite:ferrite boundaries of the ferrite allotriomorphs. The role played by the M_6C allotriomorphs may thus be primarily one of shifting

transformation times as a whole to shorter times and of displacing the initiation of the interphase boundary and fibrous carbide structures a little toward the interiors of the austenite grains.

The foregoing observations describe the situation with respect to carbide precipitation at and above the bay in the TTT-diagram, and show it to be different only in scale from the previous descriptions of Shiflet, and earlier of Berry and Honeycombe (62). Below the bay, however, the pattern of carbide precipitation undergoes drastic changes. These are summarized, together with the observations on ferrite morphology, in Table I. The fibrous structure, which is so prominent above the bay, disappears almost immediately at lower temperatures. Instead, relatively long, lath-shaped carbides (which are again Mo_2C) appear in much smaller numbers, as illustrated in Fig. 15. Both the thickness of these laths and the spacing between them are 4-5-fold larger than their counterparts for fibrous and interphase boundary carbides formed above the bay. Mo_2C laths appear to nucleate preferentially at austenite:ferrite boundaries and perhaps also at ferrite:ferrite boundaries (Fig. 15).

In some areas of the same specimens, Mo_2C needles or plates were observed to have precipitated at dislocations within the ferrite phase (Fig. 16). This mode of carbide precipitation occurred throughout the temperature range investigated; it is commonly observed at high reaction temperatures in numerous Fe-C-X systems (1), including Fe-C-Mo (62). With decreasing reaction temperature, the size of dislocation-nucleated carbides rapidly diminishes; at 575°C , typical carbides of this set are plates ca. one nm. thick and 50 nm. long (Fig. 17). Selected area diffraction showed that they have the expected Burgers orientation relationship with respect to ferrite. Nucleation sites included both isolated dislocations and small-angle boundaries between slightly misoriented ferrite laths.

Although fibrous carbides disappeared immediately below the bay in the TTT-diagram, another familiar carbide morphology which nucleates at austenite:ferrite boundaries, that of interphase boundary carbides, persisted down to 550°C (Fig. 18). The very finely divided structure produced by this reaction is responsible for the rapid etching of the ferrite allotriomorphs at late reaction times, as observed by optical microscopy (Figs. 14a-d).

Beginning at ca. 525°C , a new type of carbide precipitate begins to appear in the form of large cementite (presumably $(\text{Fe},\text{Mo})_3\text{C}$) laths occasionally nucleated at boundaries between ferrite

laths. Figs. 19 and 20 illustrate this morphology at a low and a high magnification, respectively. The SAD pattern in Fig. 19 indicates that the cementite laths have a Bagaryatskii (82) orientation relationship with respect to the surrounding ferrite. This relationship has been previously observed in lower bainite formed in Fe-C-Cr (83) and Fe-C-Si (84) alloys. Close examination of Fig. 20 shows that very small carbides are also present. These are Mo_2C , nucleated on dislocations. Their length is ca. 10^{-3} that of the cementite laths, reflecting the difference between Mo and C diffusion-control of growth kinetics.

d. Discussion

The effects of reaction temperature per se as well as of location on the TTT-curve for the initiation of transformation upon ferrite morphology and also some aspects of carbide precipitation can be explained in terms of the postulated adsorption of Mo at austenite:ferrite boundaries (4,5). This adsorption should occur preferentially at disordered-type areas on these boundaries, thereby intensifying the SDE and making the growth of ferrite more nearly isotropic. The increasing degeneracy of ferrite morphology as the bay is approached is accentuated by increasing concentrations of carbon and of Mo (17), finally culminating in the elimination of the sideplate and intragranular plate morphologies in any form within the bay region at ca. 0.25 W/O C and 4 W/O Mo (85). These observations are consistent with this explanation. The restoration of the Widmanstatten morphologies in increasingly non-degenerate form below the bay follows from the deduced maximum adsorption of Mo at austenite:ferrite boundaries in the bay region. The continued increase in driving force for growth permits the SDE to be overpowered increasingly, once the amount of Mo adsorbed either becomes constant or decreases (86) below the bay, thereby permitting at least partial restoration of the kinetics as well as the morphology which would have obtained in the absence of the SDE.

The adsorption of Mo at austenite:ferrite boundaries which produces the SDE also reduces the energy of these boundaries. On the plausible expectation that the energy of austenite:ferrite boundaries is reduced more than the energy of carbide:austenite boundaries on critical nuclei, heterogeneous classical nucleation theory predicts that austenite:ferrite boundaries should become less effective catalysts for carbide nucleation at and below the bay than they are at high temperatures. In finer detail, we note that fibrous carbides evidently nucleate at austenite:ferrite

boundaries which have a considerably higher proportion of disordered area than do interphase boundary carbides (1,87). Hence Mo adsorption should be more effective in suppressing fibrous than interphase boundary carbides, as is experimentally observed (Table I). The low nucleation rate of lath carbides at austenite:ferrite boundaries amounts to a residual effectiveness of these nucleation sites; their absence above the bay suggests that they nucleate at less effective sites on austenite:ferrite boundaries which have no opportunity to function above the bay and do so below only because the more effective sites have been deactivated by more extensive Mo adsorption. The larger sizes to which lath carbides grow are a trivial consequence of the smaller number of such carbides per unit volume competing for the available C and Mo supersaturation.

On the other hand, the appearance of cementite laths at and below ca. 525°C seems a separate and simpler effect: the rapidly decreasing diffusivity of Mo in ferrite permits the lower driving force which one would expect to attend the nucleation and growth of $(\text{Fe},\text{Mo})_3\text{C}$ to yield reaction kinetics competitive with those of Mo_2C at sufficiently low temperatures because cementite formation kinetics (particularly those of growth) should be limited by the diffusion of carbon rather than of Mo in ferrite.

3. Evaluation of the Relative Effects of Various Factors on Ferrite Growth Kinetics in Fe-C-X Alloys

a. Introduction

This sub-section summarizes a brief but crucial calculational study performed in collaboration with Dr. John R. Bradley of the General Motors Research Laboratory and Professor Gary J. Shiflet of the University of Virginia for a paper prepared for the Proceedings of the International Conference on Solid-Solid Phase Transformations (88), and also a further set of calculations performed with Prof. Shiflet while completing preparation for publication of the manuscript presenting the research summarized in section II-C-1. Although both did their Ph.D. thesis research with the full or partial support of this ARO contract, the present studies were undertaken subsequently, as part of a continuing joint effort with the P.I.

These studies dealt with the growth kinetics of grain boundary ferrite allotriomorphs in Fe-C-X alloys. This morphology was utilized in order to minimize the influence of partially coherent facets upon the migration kinetics of austenite:ferrite boundaries (15,16). Bradley and

Aaronson (6) had recently compared the growth kinetics of ferrite allotriomorphs measured in representative Fe-C-X alloys with those calculated from the three major models for X distribution during the early stages of growth (when carbon diffusion can be considered to be taking place under semi-infinite bar diffusion conditions): paraequilibrium (7-11), local equilibrium no-partition (86,89) and local equilibrium-with-partition (89,90). They concluded that the paraequilibrium model is the most appropriate; however, they also confirmed earlier observations (4,14,91) of significant deviations from the predictions of paraequilibrium growth kinetics. The purpose of the present study was to evaluate individually the influence of these deviatoric effects:

(i) Thermodynamic effect -- arising from the displacement of the paraequilibrium ($\gamma/(\alpha + \gamma)$) phase boundary of the Fe-C-X system relative to the $\gamma/(\alpha + \gamma)$ phase boundary for the Fe-C system (89,92,93);

(ii) Kinetic effects

(a) Carbide precipitation at austenite:ferrite boundaries (1-3,21);

(b) Solute drag-like effect upon the motion of austenite:ferrite boundaries (4,5,86).

b. Thermodynamic Effect

The thermodynamic effect was evaluated from the calculated ratio of the parabolic rate constant for allotriomorph thickening, α , in an Fe-C-3 A/O X alloy to that for an Fe-C alloy with the same A/O C in four Fe-C-X systems, where X was successively Si, Mn, Ni and Mo. Curves marked "Calc." in Fig. 21 show the variation of this ratio with temperature in each system. The curves denoted "Meas." in this Figure were computed from experimental data on Fe-C alloys reported by Bradley et al (16) and on Fe-C-X alloys by Bradley and Aaronson (6). (No experimental data are shown here for Fe-C-Mo because the austenite phase field contracts too rapidly to dissolve 3 A/O Mo (94).) Clearly Ni is the only element whose influence upon α can be regarded, at least in the temperature range experimentally studied, as being due primarily to the thermodynamic effect.

c. Effect of Carbide Precipitation at α : γ Boundaries

For simplicity, the influence of carbide precipitation upon ferrite growth

kinetics was analyzed only for the interphase boundary carbide structure where, despite subsequent disputes (1,2,87), it appears that the basic component in the formation of this structure is the nucleation and growth of carbides at immobilized partially coherent austenite:ferrite boundaries. The Jones-Trivedi (70) equation was used to express the overall growth rate of ledged austenite:ferrite boundaries and the influence of carbide precipitation was taken into account, in approximate but reasonable fashion, by replacing the bulk carbon concentration in the alloy with that corresponding to the extrapolated austenite/(austenite + carbide) phase boundary calculated from the Hillert-Staffansson model (65). The solid curves in Fig. 22 (for the same alloys considered in Fig. 21) show the ratio of the calculated ledgewise (constant) growth rate in Fe-C-3 A/O X alloys to that in Fe-C alloys with the same carbon concentration as a function of reaction temperature. The dashed curves in Fig. 22 indicate the temperature-dependence of the ratio of the calculated growth rate by the ledge mechanism in these Fe-C-X alloys in the presence of carbides to that in their absence. Comparison with the "Meas." curves in Fig. 21--which are for the parabolic rate constant rather than for the time-independent ledgewise growth rate--indicates that the presence of carbides at austenite:ferrite boundaries accentuates the discrepancy between the calculated and measured kinetics in Fe-2 A/O C-3 A/O C, might possibly explain the depressed experimentally measured kinetics in Fe-0.5 A/O C-3 A/O Mn and has only a limited effect in Fe-0.5 A/O C-3 A/O Ni. Carbides were found at austenite:ferrite boundaries at some higher temperatures in the Fe-C-Si alloy on which growth kinetics were measured (21), but whatever effect is causing the discrepancy between the calculated paraequilibrium and measured growth kinetics is clearly directing the experimental kinetics in the opposite direction from that of the carbide effect. In the case of Fe-C-Mn, TEM studies conducted on specimens reacted within the reaction temperature/time envelope used in ref. (6) disclosed essentially no carbides at austenite:ferrite boundaries (21), thereby ruling out this explanation for any of the discrepancy between paraequilibrium-calculated and measured growth kinetics. A similar absence of carbides at austenite:ferrite boundaries was established in the Fe-0.5 A/O C-3 A/O Ni alloy (21). The inability of carbide precipitation to explain the remarkable complex of growth kinetics effects disclosed in Fe-C-Mo was discussed in detail in section II-C-1.

d. Solute Drag-Like Effect

Fig. 23 is a plot of $\alpha_{\text{experimental}} / \alpha_{\text{paraequilibrium}} \equiv R$ for grain boundary allotriomorphs in alloys studied by the P.I. and his colleagues during several investigations (4,6,14,95, section II-C-1). With the exception of the very dilute Fe-C-V alloy, each contains roughly 3 A/O X. Many of the alloys have ca. 0.5 A/O X; higher carbon concentrations are present in several others, but only in Fe-C-Al is the A/O C drastically larger. Unless there are other as yet unknown effects involved, on the considerations of the preceding subsection Fig. 23 displays primarily the SDE in the empirical form of deviations of the plotted ratios from unity. Thus, the thermodynamic effect is automatically incorporated in α_{para} . As far as effects of carbides at $\alpha:y$ boundaries are concerned, although TEM studies were not made on the alloys wherein X is Al or Co, there is little reason to expect extensive carbide precipitation in these alloys. In the case of Fe-C-V (95), the data used in this plot are for "snake-like" grain boundary allotriomorphs at whose austenite:ferrite boundaries VC was not present. While carbides certainly were present at all austenite:ferrite boundaries observed in Fe-C-Mo, and doubtless did influence growth kinetics, as discussed in section II-C-1 this effect, no matter how considered, failed decisively to account for the measured kinetics. Hence the substantial deviations of R from unity in the Fe-C-Mo alloy should also reflect to a significant degree the influence of "the missing factor" which we have termed the SDE.

From Fig. 23, the following conclusions may be drawn: (i) at the 3 A/O X level, Mo is far more effective in producing the SDE than any of the other elements studied; (ii) if 3 A/O V could be dissolved in austenite (which it cannot (96)) and the SDE at this level may be scaled linearly upwards from that at the A/O V actually employed, V would furnish a considerably larger SDE than Mo; (iii) as we have previously suggested on the basis of less complete information (6), efficiency in producing the SDE correlates at least qualitatively with increasing size misfit between X and Fe and an increasingly negative Wagner interaction parameter, $\partial \ln \gamma_C / \partial X$, where γ_C is the activity coefficient of C in austenite or in ferrite; (iv) Co, which increases this Wagner interaction parameter, is seen to make $R > 1$ and thus produce an inverse SDE; Si increases this parameter much more and has a much larger misfit with respect to Fe, but surprisingly produced an inverse SDE only in a 2 A/O C-3 A/O Si alloy (6), and not in the

0.55 A/O C material for which R is plotted in Fig. 23; (v) in some alloys, particularly Fe-C-Mn, R increases with the decreasing temperature; this is not in accord with the previously discussed expectation for its variation with temperature and is not presently understood.

Particularly when the relatively high accuracy of the growth kinetics measurements and the calculated values of α_{para} is taken into account, together with the compression of the ordinate axis of this plot by its logarithmic character, Fig. 23 makes clear that the SDE plays a major role in determining the growth kinetics of grain boundary ferrite allotriomorphs in a number of Fe-C-X systems. The need for a quantitative treatment of the SDE is thus further emphasized.

4. Theoretical Analysis of the Solute Drag-Like Effect

This project represents the theoretical portion of the Ph.D. thesis program being followed by Mr. William T. Reynolds, Jr. The experimental component of his research includes:

(i) scanning Auger microprobe analyses of X segregation at austenite:ferrite boundaries; these data would be used during application of SDE theory to growth kinetics measurements.

(ii) a re-examination of the question: does stasis (incomplete transformation) exist in any of the "common" Fe-C-X systems?

Mr. Reynolds' research is in its early stages, with most of the effort to date having been devoted to the theoretical aspect. A full description of the projected experimental program is offered in section III-B-1. For present purposes, though, it should be recalled that stasis is considered to occur under circumstances where the SDE is exceptionally strong. It seems likely that sufficient experimental data on ferrite allotriomorph growth kinetics are already available with which to test a theory of the SDE for the situation in which this effect is not strong enough to produce stasis. By contrast, however, reliable information on the presence or absence of stasis in high-purity Fe-C-X alloys seems confined, at the present time, to Fe-C-Mo alloys. Hence we propose to rebuild the "data bank" of information on stasis by means of studies on a few carefully chosen alloys in each of a wide range of Fe-C-X systems. Interpretation of these data would be based on application of the SDE theory being developed to the qualitative concepts presented in section II-C-1, with the objective of evolving a quantitative theory of stasis.

The principal theories of the solute drag effect during the migration of grain boundaries remain those of Lucke and Detert (12a), Lucke and Stuwe (12b) and Cahn (13).*. A central aspect of these theories is that impurity atoms are considered to interact with a moving grain boundary with sufficient strength so that, unless the driving force is high (relative to the impurity concentration and the temperature), migration of the boundary requires that the impurity atoms be either dragged along behind or pushed ahead of the advancing boundary. Hence movement of the impurity atoms occurs with an activation energy approximating that for volume diffusion, though somewhat modified by the precise positions of the impurity atoms relative to the boundary region and the sign of the impurity-grain boundary interaction. It is at this point that the solute drag-like effect we are considering and the (true) solute drag effect upon grain growth are suggested to differ. Over most of the temperature ranges of interest, the X atoms cannot diffuse as much as a single austenite lattice parameter during the time interval during which measurements of growth kinetics are made (6). Hence migration of austenite:ferrite boundaries under these circumstances will not be controlled by the volume diffusion of X or any approximation thereof.

On the other hand, X atoms which have a binding energy to an austenite:ferrite boundary are readily acquired by the moving boundary and retained for sometime after the instant of acquisition, since solute diffusivity in ferrite and in austenite grain boundaries (23), and hence probably in disordered-type areas of austenite:ferrite boundaries, is approximately comparable to the diffusivity of carbon in austenite (99). With Lucke and Detert (12a), it seems permissible (at least initially) to approximate the X concentration at a moving austenite:ferrite boundary as similar to that at a stationary boundary of the same type. Taking the growth kinetics of this boundary to be controlled by the diffusion of carbon in austenite, one may then consider how X adsorption at the boundary would affect the kinetics of carbon diffusion. Clearly, such an effect could only occur if X adsorption were to alter the carbon concentration, or more accurately, the partial molar free energy of carbon in the austenite in contact with the boundary, and thus the driving force for carbon diffusion. Assume, temporarily, that transformation is occurring sufficiently near the $\gamma/(\alpha + \gamma)$ temperature and the value of that temperature is sufficiently high

*A parallel theory has been developed by Hillert and Sundman (97) for the massive transformation. It appears that Hillert (98) may currently be working on an extension of this theory to precipitation reactions, and probably especially to the proeutectoid ferrite reaction. We would certainly apply Hillert's theory if it takes the expected direction.

so that not only C but also Fe and X atoms in austenite are in equilibrium with those in ferrite in the region of the austenite:ferrite boundary. Any segregation of X to (and Fe away from) the boundary would then ensure that the partial molar free energy of all three species in ferrite is equal to that of their counterparts in austenite at the boundary. Hence no effect would be exerted upon the driving force for carbon diffusion by X segregation under equilibrium conditions.

Consider next the situation which would obtain if paraequilibrium were to be established at austenite:ferrite boundaries. Only the partial molar free energy of carbon is now the same on both sides of the boundary. For Fe and X atoms, discontinuities are established in accord with the relationship (11):

$$(5) \quad \bar{G}_X^Y - \bar{G}_X^\alpha = -(\bar{G}_{Fe}^Y - \bar{G}_{Fe}^\alpha) \frac{x_{Fe}}{x_X}$$

where \bar{G}_i is the partial molar free energy of X or Fe in austenite or ferrite as indicated and x_i is the atom fraction of X or Fe in the alloy. The very low volume diffusivity of X in austenite relative to carbon diffusivity in this phase permits retention of these discontinuities during at least the early (and most important) stages of growth. However, Fe and X atoms can migrate freely within the moving boundary. Hence it should be possible for these species to segregate or desegregate within the boundary by means of a "sweeping up" mechanism or its inverse. Unlike the full equilibrium situation, however, segregation of the substitutional species will change the partial molar free energy of the carbon atoms in the bulk austenite (and ferrite) with which they are in immediate contact. If this change decreases the difference between the partial molar free energy of carbon in contact with the austenite:ferrite boundary and that remote from the carbon diffusion field associated with this boundary, the driving force for the growth of ferrite will be diminished, and vice versa. These effects are proposed as the origins of the SDE and the inverse SDE, respectively.

In order to place these considerations on a quantitative basis, the model developed by Guttmann and McLean (22) for segregation to grain boundaries in substitutional-interstitial ternary solid solutions will be adapted to the interphase boundary case. The particular form of the Guttmann-McLean (GM) model to be used is that in which C and X are taken to reside on independent sublattices, but are allowed to interact chemically and thereby affect segregation. In

order to acquire a "baseline" for segregation under paraequilibrium conditions, the equations governing segregation to austenite:ferrite boundaries under conditions of full equilibrium were first sought. A basic hypothesis of the GM treatment is that equilibrium is established between a bulk crystal and the grain boundary with which it is in contact. The boundary is treated as a "surface phase", designated as ϕ . On this approach, both bulk austenite and bulk ferrite, each with its equilibrium composition, are in equilibrium with the boundary phase. Hence the formalism for equilibrium segregation at grain boundaries may be converted to that for equilibrium segregation at interphase boundaries by simple one-to-one replacement of a few symbols. Enomoto (24) has recently maneuvered the GM equations for grain boundary segregation into more directly usable form. For segregation to an austenite:ferrite boundary--using the austenite phase as the bulk one simply because of the superior availability of ancillary data in this phase--these relationships become:

$$(6) \quad \frac{y_X^{\gamma\alpha} \gamma}{(1-y_X^{\gamma\alpha})^{\omega_X/\omega_{Fe}} (1-y_C^{\gamma\alpha})^{\omega_C/\omega_{Fe}} \gamma^{(c/a)\gamma} \gamma^{(\omega_X/\omega_{Fe} - 1)}} \cdot \exp \left(\frac{\Delta G_X^0(\gamma) + \Delta^m H_X(\gamma)}{RT} \right)$$

$$= \frac{y_X^\phi}{(1-y_X^\phi)^{\omega_X/\omega_{Fe}} (1-y_C^\phi)^{\omega_C/\omega_{Fe}} \phi^{(c/a)\phi} \phi^{(\omega_X/\omega_{Fe} - 1)}}$$

$$(7) \quad \frac{y_C^{\alpha\gamma} \gamma}{(y_{Fe}^{\gamma\alpha})^{\omega_C/\omega_{Fe}} (1 - y_C^{\gamma\alpha})^{\omega_C/\omega_{Fe}} \gamma^{(c/a)\gamma} \gamma^{(\omega_C/\omega_{Fe} + 1)}} \exp \left(\frac{\Delta G_C^0(\gamma) + \Delta^m H_C(\gamma)}{RT} \right)$$

$$= \frac{y_C^\phi}{(y_{Fe}^\phi)^{\omega_C/\omega_{Fe}} (1 - y_C^\phi)^{\omega_C/\omega_{Fe}} \phi^{(c/a)\phi} \phi^{(\omega_C/\omega_{Fe} + 1)}}$$

where $y_X^{\gamma\alpha}$ and $y_C^{\gamma\alpha}$ are the atom fractions of X and of C in austenite corresponding to the austenite terminus of the equilibrium tie-line across the $\alpha + \gamma$ region of the Fe-C-X system at temperature T, $y_{Fe}^{\gamma\alpha}$ and $y_C^{\gamma\alpha}$ are the atom fractions of Fe and C in the boundary, respectively, ω_i is the partial molar area of the i'th component (at constant values of pressure, temperature and concentrations of the other elements present), $(c/a)_\gamma$ and $(c/a)_\phi$ are the number of interstitial sites per substitutional site in austenite and in the boundary, respectively, $\Delta G_i^0(\gamma)$ is the binding free energy of the i'th component to the austenite:ferrite boundary relative to the γ phase in the

absence of chemical interactions and $\Delta^m H_i(\gamma)$ is the binding enthalpy of the i 'th component to the boundary relative to the γ phase arising from chemical (mixing enthalpy) interactions. (An entropic term is not included with $\Delta^m H_i(\gamma)$ because incorporation of the Hillert-Staffansson (65) regular solution formalism automatically excludes excess entropy of binding.) With GM, it is assumed (with little loss of accuracy) that $\omega_X = \omega_{Fe}$; with justification arising primarily from the use of dilute solutions, it is also taken that $\omega_C = 0$. Noting that $(c/a)_\gamma = 1$ and assuming that the same value applies to $(c/a)_\phi$, the foregoing equations are simplified to:

$$(8) \quad \frac{y_X^{\gamma\alpha}}{X - y_X^{\gamma\alpha}} \exp \left(\frac{\Delta G_X^o(\gamma) + \Delta^m H_X(\gamma)}{RT} \right) = \frac{y_X^\phi}{1 - y_X^\phi}$$

$$(9) \quad \frac{y_C^{\gamma\alpha}}{X - y_C^{\gamma\alpha}} \exp \left(\frac{\Delta G_C^o(\gamma) + \Delta^m H_C(\gamma)}{RT} \right) = \frac{y_C^\phi}{1 - y_C^\phi}$$

ΔG_X^o and ΔG_C^o in Eqns. (8) and (9) can be approximated as the strain energy associated with X and with C atoms in austenite, taken to be relieved completely by segregation to disordered austenite:ferrite boundaries (following McLean (99a) for grain boundaries). These quantities can be estimated from a relationship due to Friedel (99b). The adsorption enthalpies in Eqns. (8) and (9) are defined as:

$$(10) \quad \Delta^m H_X(\gamma) = ({}^m H_{Fe}^\phi - {}^m H_{Fe}^\gamma) - ({}^m H_X^\phi - {}^m H_X^\gamma)$$

$$(11) \quad \Delta^m H_C(\gamma) = -({}^m H_C^\phi - {}^m H_C^\gamma)$$

where ${}^m H_i^j$ is the enthalpy of mixing of the i 'th species in the j 'th phase. These quantities are expressed as quadratic functions of y_i^j and regular solution constants on the ternary regular solution model of Hillert and Staffanssen (65). Taking (necessarily) these constants to be the same in the boundary as in the bulk austenite, $\Delta^m H_X$ and $\Delta^m H_C$ can be calculated from available thermodynamic data (96).

As previously discussed, under paraequilibrium conditions the details of the segregation process are quite different. However, if $y_X^{\gamma\alpha}$ and $y_C^{\gamma\alpha}$ are replaced by their paraequilibrium (65)

values Eqns. (8) and (9) apply to this situation. Unlike the full or orthoequilibrium situation, though, different values of y_X^* and y_C^* will be obtained when calculated on the basis of equilibrium with the ferrite instead of the austenite phase. (In the full equilibrium case this will not happen.) This unusual situation follows directly from Eq. (5), in which the inequality of the partial molar free energies of both X and Fe in ferrite with respect to their counterparts in austenite is quantitatively characterized. Hillert (86) has deduced remarkably complex curves of X-concentration vs. distance lying wholly within austenite:ferrite boundaries. Here, a simpler postulate is made, namely, that such boundaries, when they have a disordered type of structure, may be approximated by two layers, one in atomic contact with bulk austenite and the other with bulk ferrite. Hence two layers of atoms are juxtaposed in which both X and Fe have different partial molar free energies in the respective layers. Given the proximity of the layers and the high diffusivity expected in disordered-type boundaries, this situation should, of course, promptly undergo modification. Again unlike the grain boundary case, equalization of the partial molar free energies cannot be accomplished through volume diffusion of X in austenite because the transformation kinetics are too rapid (6). Hence such adjustments as can occur will have to take place wholly within the boundary. At the present time we are considering various possibilities for this adjustment which could be quantitatively modeled. One might be obtained from a Cahn-Hilliard-like gradient energy approach, wherein the presence of one layer would alter the partial molar free energies in the other without changing the composition of either. Another establishes equality between the partial molar free energies by interdiffusion between the two layers. On either model, as well as others which might be reasonably foreseen, however, the interaction between the two layers of atoms would require a change in the partial molar free energy of carbon in the bulk austenite in contact with the austenite-side boundary layer. This change, transformed into an alteration in the paraequilibrium y^* , would constitute the heart of the solute drag-like, or the inverse solute drag-like effect. Once the amount of this change has been established, modification of any equation used to describe the growth kinetics of austenite:ferrite boundaries should be straightforward.

D. Interfacial Structure Barriers to Growth

Whereas the previous section dealt with investigations concerned with chemical effects

upon growth kinetics in Fe-C-X alloys (which often turn out to be barriers to or interferences with diffusional growth processes, e.g., the solute drag-like effect), here we summarize studies which dealt with interfacial structure barriers to growth. While the venue of these studies is considerably broader in that a wide range of alloy systems, predominantly non-ferrous (and fortuitously Cu-base), is utilized as experimental models, the influence of the proeutectoid ferrite and bainite reactions in steel is usually not far below the "surface", and indeed becomes increasingly apparent in successive subsections. In all cases, however, we view the alloy systems and particular pairs of crystal structure comprising a given type of interphase boundary as prototypes through which fundamental generalizations and understanding are sought.

1. The Role of Interphase Boundary Structure During Phase Transformations in β and β' Cu-Zn Alloys

This subsection reports the work performed by Dr. Kamanjo Chattopadhyay during the tenure of a two-year sabbatical leave with the P.I. which was wholly supported by the present contract. Dr. Chattopadhyay was a Lecturer in the Department of Metallurgical Engineering, Banaras Hindu University, Varanasi, India, when he joined us but since returning to India has become an Assistant Professor in the Department of Metallurgy, Indian Institute of Science, Bangalore.

This investigation was originally planned to be confined solely to the structure of the broad faces of α_1 Cu-Zn plates; it was then expected that Dr. Chattopadhyay would undertake investigations of the interphase boundary structure of planar facets formed during a massive transformation and finally of the broad faces of AuCu II plates. However, through Dr. Chattopadhyay's initiative, the α_1 plate study was successively enlarged to include the broad faces of α_1 martensite plates, which also form from β' Cu-Zn, though at lower temperatures, and then the long faces of α rods precipitated from β and β' Cu-Zn. The results and interpretation of these studies are reported in the following subsubsections.

a. The Interphase Boundary Structure and Growth Mechanism of α_1 Cu-Zn Plates

(1) Introduction

When Cu-Zn alloys containing ca. 38-43 A/O Zn are quenched from the β (disordered bcc) region into the $\alpha + \beta'$ region (α is disordered fcc), the β phase swiftly undergoes homogeneous ordering to the CsCl-type β' phase. Below temperatures varying from ca. 400°C at 38 A/O Zn to ca. 250°C at 43 A/O Zn, plates of the orthorhombic transition phase, α_1 , are formed from the (now) β' matrix (100). In the last 15 years, the $\beta' \rightarrow \alpha_1$ transformation has become an important model reaction through which to develop, by means of increasingly refined experiments, the debate about the contributions made by diffusional and by shear mechanisms to the formation of slowly growing precipitate plates which appear to fulfill at least some of the specifications provided by the phenomenological theory of martensitic transformations.

The surface relief effects, irrational habit plane, irrational lattice orientation relationships, lattice correspondence and internal structure (which can be associated with the lattice invariant deformation of a martensitic transformation) are all the same as those characterizing α_1 martensite formed at lower temperatures in some of the same alloys (101). Since α_1 plates form above the M_s temperature and appear to grow slowly, with approximately D_v -controlled kinetics (102), they are currently considered to be bainite, as defined by the surface relief-definition (103). However, as Wayman (104) has pointed out, a product phase claimed to have formed martensitically must obey all of the specifications of the phenomenological theory of martensite. The question of whether or not one of these specifications, that the composition of the product phase be identical to that of the matrix, is fulfilled, however, is the subject of an intense and continuing dispute in the literature (105-112); evidently Cu-Zn alloys in this composition range are particularly troublesome subjects for STEM-type analyses (45). Hence an attempt was made during the present study to consider experimentally the question of whether α_1 plates form by a martensitic or a diffusional mechanism through still another specification for a martensitic transformation (113), namely that the interphase boundary structure (especially that of the broad faces of plates) be capable of migration by a shear mechanism. This crucial question was investigated by means of high-resolution TEM.

(2) Experimental Procedure

Alloys containing 37.38, 38.64 and 43.40 A/O Zn, furnished by the

Brush Wellman Co. through the courtesy of Dr. Amitava Guha, were employed. Specimens were solution annealed one min. at 875°C and isothermally reacted at 230° to 400°C. Mechanical thinning was avoided to prevent formation of stress-induced martensite. For electrolytic thinning, needed to prepare thin foils, a Struers D2 electrolyte, operated at 15°C, was employed instead of those used by previous investigators because these electrolytes, requiring much lower temperatures for successful use, may have permitted formation of martensite in thin foils. TEM studies were performed with a JEOL 120CX; Kikuchi patterns were employed for crystallographic analyses; unless otherwise specified, matrix reflections were usually used for both imaging and analyses.

(3) Results

Fig. 24 shows one of the most crucial results obtained: a selected area electron diffraction pattern confirms, using Sato's approach (114), the customarily ignored findings of Hornbogen and Warlimont (115) that the crystal structure of α_1 is of the close-packed 3R type, having orthorhombic symmetry, but without the rows of superlattice reflections characterizing martensite with the same crystal structure in the same alloys (116). Hence the isothermally formed α_1 plates which we studied have a disordered structure formed in an ordered matrix, contravening an important specification of the phenomenological theory of martensite (104).**

Habit plane data were consistent with those of previous investigators and will not be repeated here. Instead attention will be focused upon the new observations made on the evolution of the interfacial and internal structure of isothermal α_1 plates.

TEM studies showed that the thickening of α_1 plates can be divided into at least four rather well defined stages. During the first stage, a characteristically complex dislocation loop-type contrast could be observed with a $[110]_{\beta'}$ reflection (Fig. 25). The micrographs comprising Fig. 26 show an α_1 plate tilted at three different angles, with the electron beam being perpendicular to the broad faces in Fig. 26b and revealing the plate edges in Fig. 26c. In none of these views are stacking faults or any other defects observed within the plate, and no interphase boundary dislocations appear at any interface. Taken together, Figs. 25 and 26

** As discussed in section III-C-1 in connection with the proposed investigation of the structure of the broad faces of AuCu II plates, however, this violation is no longer universally considered to be fatal to the operation of a martensitic growth mechanism (31).

demonstrate that α_1 plates are initially fully coherent with their β' matrix. Further, the strain contrast associated with α_1 plates in Fig. 25 is similar to that observed by Weatherly et al (117) at bcc Cr-rich precipitates formed within an fcc Cu-rich Cu-Cr matrix during early stages of growth. Using computer modeling techniques, these investigators established that the details of strain contrast observed are consistent with full coherency. (Hornbogen and Warlimont (115) noted similar contrast effects during the early stages of α_1 plate growth but did not offer the present interpretation of them.)

During the second stage of α_1 plate thickening, one set of misfit dislocations became emplaced on the broad faces of these plates. Arrows in Figs. 26a and 27 show examples of fully coherent α_1 plates acquiring misfit dislocations by attraction of and interaction with matrix dislocations, a process first described (for another alloy system) by Weatherly and Nicholson (118) and since observed in many others (119). Fig. 28 illustrates the second stage fully developed: a single set of dislocation loops is wrapped around an α_1 plate. These loops are also seen to bound stacking faults passing through the plates, as schematically illustrated in Fig. 28c. Possibly the faults are formed by dissociation of the loops. Contrast experiments were carried out at several interfaces in order to determine the Burgers vector of the misfit dislocations and its orientation with respect to the interface plane. All yielded the same result. Fig. 29 is a typical set of micrographs taken of a given interface (this one lay near $(2,11,12)\beta'$) under various diffraction conditions. Figs. 29a, d and e were obtained with the indicated operating reflections in exact two-beam condition, while Figs. 29b and c are weak-beam images satisfying $g - 3g$ conditions. Fig. 29e was enlarged to display the details of the interfacial structure. Only one set of dislocations, spaced a minimum of ca. 2.1 nm. apart, is seen to be present. Fig. 29d shows that the dislocations are essentially invisible when the operating g is $[020]\beta'$. A summary of the contrast experiments is provided in Fig. 29g and indicates that the Burgers vector of the misfit dislocations is parallel to $[101]\beta'$. Fig. 29h shows the results of the habit plane, fault plane and Burgers vector determinations for this interface on a stereogram. As at all of the other $\alpha_1:\beta'$ interfaces analyzed in this manner, the Burgers vector of the misfit dislocation loops lay in the stacking fault plane but out of the interface (habit) plane.

Both the interphase boundary and the faults are imaged in the $(009)\alpha_1$ reflection, accurately

fulfilling the Bragg condition, in Fig. 30. The faults and the misfit dislocations are invisible. This result, coupled with the streaks in the c^* direction in reciprocal space shown in Fig. 24, lead to the conclusion that the faults are normal to the c -axis of the orthorhombic cell.

In addition to misfit dislocations, the weak-beam image of Fig. 29b shows that growth ledges are also present. With the assistance of a dashed line, the ledges are more clearly revealed in the enlargement of a portion of this micrograph included as Fig. 29f. Another diffraction contrast mechanism is utilized to reveal growth ledges in Fig. 30b. Imaging the interface with a β' reflection which satisfies the extinction condition of the misfit dislocations displays growth ledges through the cusps which they produce in extinction contours. Further observations on this α_1 plate made by tilting away from the Bragg condition demonstrated that at least in this instance the ledges encircled the plate. Fig. 30c illustrates similar deflections of the extinction contours on another interface, but now imaged under strong two-beam conditions with respect to an α_1 reflection. Finally, Fig. 31 shows an α_1 plate whose broad faces were fortuitously oriented nearly parallel to the foil surface. Using the Weatherly et al (120-123) method of displaying ledges by imaging with a precipitate reflection not duplicated in the matrix and tilting slightly away from the Bragg condition yields a clear view of the growth ledge structure on some areas of this plate.

The third stage of α_1 plate thickening consists of the acquisition of a second set of misfit dislocations. (Typically, these dislocations are first found after 7 min. of transformation at 250°C in the 38.64 A/O Zn alloy.) As in the acquisition of the first set of dislocations, adsorption of matrix dislocations plays an important role in the establishment of the second array. Fig. 32a illustrates the initial stage in this process, pointing out with arrowheads a dislocations being incorporated in the interphase boundary. Since the matrix phase is ordered, the adsorbed dislocation should be a superdislocation; this is confirmed in the inset of Fig. 32a. Arrows in Fig. 32b indicate example misfit dislocations in the second array formed at the junction between two α_1 plates. Upon further transformation, the second set of dislocations becomes periodic. Although the strong fault contrast often makes observation of these dislocations difficult (Fig. 33a), they can always be seen by appropriate tilting of the foil (Fig. 33b). Periodicity of these dislocations appears to be achieved by glide in the interface. Fig. 33c illustrates acquisition of

matrix dislocations by the interface in a configuration suggesting that gliding has occurred. Figs. 33d and e demonstrate that the second set of dislocations can be complexly and irregularly arrayed. In general, though, the angle between the first and second sets tends to be ca. 60°. The average spacing between dislocations of the second set, when they are present as a well formed array, is ca. 12 nm. Although it was not feasible to determine uniquely the Burgers vector of the second set of dislocations for a sufficient number of cases to ensure reliability, the results obtained suggest that this vector is parallel to $[011]_{\beta'}$. Since these dislocations appear to be redistributing by glide within the broad faces, their Burgers vector would appear to lie in the interface plane.

After reaction for one hr. or longer at 250°C in the 38.64 A/O Zn alloy, the fourth stage of α_1 plate thickening begins: the broad faces become pronouncedly faceted, with the facet planes lying at an appreciable angle with respect to the original plane of the broad faces, as illustrated in Fig. 34. Indications were found that not only the facet planes but also at least some of the risers connecting them are partially coherent.

Isothermal reaction was terminated not later than the fourth stage of thickening during the present studies. Subsequent development of wriggly interphase boundaries and the accompanying annealing out of stacking faults and conversion of the precipitate lattice from orthorhombic to fcc reported by previous investigators (101,115) should probably be considered to comprise the fifth and final stage of the thickening process.

Although not on our original agenda, some interesting qualitative observations were made on the interfacial structure of α_1 plate edges. The best of these observations were acquired during the second stage of thickening. Fig. 35 shows a sequence of micrographs taken at a succession of tilt angles. Although it did not prove practicable to characterize quantitatively the linear defects displayed in these micrographs, some useful conclusions can still be drawn from them. The defect structure at the edges differs significantly from that at the broad faces. These defects exhibit the broad contrast characteristic of ledges (124). Considerable strain appears to be associated with the edge of an α_1 plate (Fig. 35a). The weak-beam micrograph of Fig. 35d suggests the presence of additional complexities in this structure, possible in the form of misfit dislocations.

Fig. 36 plots the maximum thickness of α_1 plates formed in the 38.64 A/O Zn alloy as a function of isothermal reaction time at 250° and 300°C. An additional data set, in which specimens were quenched to room temperature prior to transformation at 250°C, is also included and shows that other transformation processes which occurred during the initial quench to room temperature (125) significantly reduced the driving force for growth.

(4) Discussion

In addition to serving as a model transformation for elucidating the shear vs. diffusional growth controversy, the $\beta' \rightarrow \alpha_1$ reaction has also acquired a considerable literature in which particular attention is paid to the complexities introduced by the 3R orthorhombic structure of the α_1 phase. In the nearly finished draft of the paper for Acta Met. recounting the results of the present investigation, this special literature is critically reviewed in some detail. In the interest of brevity, however, the considerations summarized here will emphasize the impact of the present results upon the more or less system-independent literature dealing with the fundamental controversy at issue.

The consequences of the observations reported on the interfacial and internal structures of α_1 will be examined first. In respect of the first stage of thickening, the absence of both internal (stacking) faults and misfit dislocations is inconsistent with the various martensitic mechanisms proposed for the growth of α_1 . Since the average distance between the random stacking faults in α_1 is only ca. 2.3 nm., whereas the average thickness of fully coherent α_1 plates is 10 nm. and their average length is 200-300 nm. during transformation at 250°C in the 38.64 A/O Zn alloy, the presence of the faults, indicative of the operation of a lattice invariant deformation, is essential to the formation of such plates by shear. The absence of interfacial dislocations in glissile orientation is almost equally indicative that a shear mechanism is not operative during this stage of growth. On the other hand, these observations are consistent with growth via diffusion-controlled lateral migration of ledges. Failure to observe ledges may be regarded as "non-lethal" and a reasonable consequence of both coherency strains and microscope resolution insufficient to resolve ledges on these thin plates, particularly in the presence of a coherency strain field. We hope to readdress this specific question soon, however, with a higher resolution transmission electron microscope.

During the second stage of thickening, the simultaneous presence of stacking faults and a single array of misfit dislocations in glissile orientation is consistent with a shear mechanism of growth. However, an ample supply of growth ledges was also observed. These ledges can be regarded as linear defects whose Burgers vector is ca. orthogonal to the interface plane. Simultaneous normal growth of the interphase boundary by shear and lateral movement of the growth ledges--even by shear--is of course mechanistically impossible. On the diffusional model, however, the terraces of the ledges are immobile despite the glissile dislocations which they contain because the difference in crystal structure across the coherent regions between the interfacial dislocations should prevent any normal migration of these regions, and hence of the terraces as a whole (32).

The presence of two different sets of interfacial dislocations during the third, and presumably also the fourth stages of thickening also prevents growth by a shear mechanism. Once again, however, these interfacial structures will permit growth by the diffusion-controlled lateral migration of growth ledges.

Doig and Flewitt (126) have proposed that α_1 plates thicken initially by shear, but subsequently by diffusion. However, Fig. 36 shows no sign of the discontinuity in thickening kinetics this mechanism would require.

Although confirmation of the Hornbogen-Warlimont (115) finding that α_1 is disordered despite the fact that it has formed from an ordered matrix should, on the phenomenological theory of martensite, immediately rule out shear mechanisms of growth, Bowles and Wayman (31) have proposed, in respect of the equivalent controversy concerning the growth mechanism of AuCu II plates, that ordering can occur simultaneously with shear by a (necessarily) diffusional process. This mechanism, however, seems self-contradictory, since in a substitutional solid solution, shear and diffusion would appear to be mutually exclusive.

The final result of general importance is the finding that the edges of α_1 plates are partially coherent. Although it was disappointing not to be able either to resolve fully nor to characterize quantitatively the structure of these interfaces, the conclusion (at least on the diffusional growth mechanism!) that they also migrate by the lateral movement of ledges is consistent with the lengthening kinetics measurements and analyses reported by Simonen and Trivedi (102).

b. The Interphase Boundary Structure of α_1 Martensite Cu-Zn Plates

(1) Introduction

Several investigations of the interfacial structure of martensite plates have now been reported (127-131). Only one of these, by Perkins (128), has dealt with α_1 martensite in Cu-Zn alloys (whose crystal structure is identical to that of isothermal α_1), and was devoted to the morphology rather than the dislocation structure of these interfaces. Although the results obtained from the present study also turned out to be of interest to the study of martensitic interfaces per se, the primary objective was to compare the interfacial structure (and internal structure) of α_1 martensite with that of α_1 plates formed isothermally well above the M_s temperature, as described in the previous subsection.

(2) Experimental Procedure

The 37.38 and the 38.64 A/O Zn alloys used in the preceding study were employed. Identical results were obtained from these alloys.

(3) Results

Both α_1 and fcc (132) martensites (primarily the former) were found; the present investigation was confined to α_1 martensite. Two different types of α_1 martensite plates were observed. These are illustrated in Figs. 37 and 38. Selected area electron diffraction showed that both types of martensite have the ordered 3R (orthorhombic) crystal structure. The martensite plates in Fig. 38 have an appreciably smaller aspect ratio than those of Fig. 37 and are presumably of the thermoelastic variety. A significant difference in their internal structures and a lesser one in their interfacial configurations will be demonstrated.

Fig. 39 shows the internal and interfacial structures of a plate of the thicker (Fig. 37-type) α_1 martensite. Only one set of misfit dislocations is present; as in the isothermal α_1 , these dislocations bound stacking faults passing through the plate. Noting that the direction of the dislocations varies, however, the question had to be raised as to whether or not additional sets of dislocations might be present. This question was answered by imaging the dislocation with a

matrix reflection which makes them invisible. Only if all of the dislocations at different portions of a curved interface are simultaneously extinct can the dislocations be of a single set. Fig. 40 "performs" this test and proves that, indeed, but one set of interfacial dislocations is present.

Fig. 41 illustrates the TEM structure of a "thin" martensite plate (Fig. 38-type). Note that a second set of faults, with an average spacing of ca. 0.15 microns, is present and has caused formation of ledges in the interphase boundary. Whereas the first, much denser array of faults can be associated with the primary inhomogeneous shear, the second set indicates that a secondary inhomogeneous shear also occurred, presumably to reduce the transformation strain energy (116). The association of the secondary set of stacking faults with ledges indicates that the dislocations associated with these faults halted growth in areas of the interphase boundary where two non-parallel sets of dislocations were simultaneously present.

The Burgers vector of the interfacial dislocations bounding the thicker plates, as well as the habit plane and orientation relationship of these plates, were determined by standard means. Fig. 42 shows the dislocation structure of one such interface viewed in three different reflections. Extinction was achieved with both of the latter two; hence the Burgers vector of these dislocations is parallel to $[101]_{\beta'}$. Fig. 43 is a stereogram in which the orientation relationship between the plate and its β' matrix grain has been plotted. These results do not differ very much from the three different sets of relationships reported in the literature (115,132,133), but are closest to those of Cornelis and Wayman (132):

$$\begin{aligned} (009)_{\text{ortho}} & 5.5^\circ \text{C from } (101)_{\beta'} \\ (114)_{\text{ortho}} & // (\pm 0.5^\circ)(011)_{\beta'} \\ (115)_{\text{ortho}} & // (\pm 0.5^\circ)(110)_{\beta'} \end{aligned}$$

Fig. 43 also includes the Burgers vector of the misfit dislocations, the stacking fault plane and the habit plane. An expected result apparent from the stereogram is that the Burgers vector is not parallel to, i.e., lies out of the habit plane. This is consistent with the requirement that the interfacial dislocations round a martensite plate have a glissile orientation (113). An unexpected result displayed by this Figure is that the Burgers vector does not lie in a plane parallel to that of the stacking faults. Fig. 44 is a stereoplot summarizing the crystallographic results from another interface, yielding equivalent results. In order to test this surprising and important

finding further, another, more accurate method was employed. The foil is carefully tilted until the trace of the fault planes in the plane of the foil and the interfacial dislocations which bound the faults lie in the same lines (Fig. 45a). Under this condition, the beam direction (which can be accurately determined by means of Kikuchi line analysis) lies in the fault plane and permits unique determination of this plane (Fig. 45b). Contrast experiments are then conducted to determine the Burgers vector of the dislocations (Figs. 45c-e). The results are plotted in Fig. 45b, again with respect to the β' lattice, and the finding that the Burgers vector of the dislocations lies out of the fault plane is seen to be confirmed.

Fig. 45e shows the same interface imaged with an $(009)_{\beta'}$ operating reflection. This g is nearly parallel to the $(110)_{\beta'}$ reflection shown in Fig. 45c. However, extinction has been achieved only with the $(110)_{\beta'}$ and not with the $(009)_{\beta'}$ reflection. It can also be noted that the Burgers vector with respect to the α_1 lattice under the extinction condition of Fig. 45e will lie in the fault plane. Thus the displacement fields due to the dislocation are not equivalent on both sides of the interphase boundary.

Fig. 47 presents one more analysis of the foregoing type for a martensite:matrix boundary. In this case, however, the interface lies close to the edge of the foil. Fig. 45a shows the interface aligned as previously described so as to make the fault plane parallel to the beam direction. The foil plane normal in this case is close to the $\langle 111 \rangle_{\beta'}$ zone axis. The arrow in this Figure marks the $[110]_{\beta'}$ direction perpendicular to the fault plane. Figs. 45b and c show extinctions of the faults and their associated dislocations in two different reflections. A stereoplot of the crystallographic data obtained, again with respect to the β' phase, shows that unlike the previous observations the Burgers vector in this situation lies in the fault plane. The achievement of extinction with $(009)_{\beta'}$ indicates that the displacement field of the interfacial dislocations in the martensite phase now lies in the fault plane.

(4) Discussion

It should first be briefly noted that a few differences developed between the results of the present study and the investigation reported by Perkins (128) of martensitic interfacial structure in Cu-Zn alloys. In particular, both glissile dislocations and ledges were identified in the present study whereas Perkins observed only ledges. Our results, however, are consistent with the observations of Chakraborty and Wayman (129) in Cu-Zn-Al alloys.

Ledges of different origins and heights were found in the two types of α_1 martensite. Their origins will be considered in some detail in the paper but not here, since they are somewhat apart from the main thrust of this research.

Comparison of the present results with those reported in the previous subsection on α_1 plates formed isothermally above the M_s temperature shows the following differences between the two transformation products:

(i) Isothermal α_1 is disordered whereas martensitic α_1 is ordered. Since the β' matrix is ordered, only the ordered structure of α_1 martensite is consistent with the phenomenological theory of martensite.

(ii) During early stages of growth, isothermal α_1 plates are fully coherent and free of internal faults whereas α_1 martensite plates are always faulted and partially coherent. (One could, of course, point out that the high growth velocity of the martensite plates prevents their observation at sizes comparable to those of isothermal α_1 plates during the first stage of their growth. However, if α_1 martensite plates really are initially fully coherent then martensite theory must be seriously in error.)

(iii) The interfacial and internal structures of isothermal and martensitic α_1 are similar during the second stage of isothermal α_1 growth. However, whereas the single array of interfacial dislocations which initially appears on isothermal α_1 plates is acquired slowly and "painfully", that on the martensite plates is swiftly emplaced despite the fact that orders of magnitude less time are available in which to acquire and organize the dislocations on the martensite plates. Also, the isothermal α_1 plates have growth ledges on their broad faces whereas α_1 martensite plates do not. As previously noted, the addition of growth ledges to interfacial dislocations with a different Burgers vector prevents displacement of second stage, isothermal α_1 broad faces by shear.

(iv) The third (and later) stages of isothermal α_1 plate growth have no counterpart in the martensitic structures. When two sets of interfacial dislocations are present, as during the third (and presumably later) stages of isothermal α_1 growth, the shear mechanism becomes mechanistically infeasible.

Thus this investigation has shown significant differences between the internal and interfacial

structures of isothermal and martensitic α_1 , sufficient to permit the conclusion that the growth mechanisms of the two transformation products must be different, with the isothermal version being impossible to produce by a shear mechanism.

The results obtained on α_1 martensite are also of interest in the context of the theory of martensitic transformations per se. Christian (113) has pointed out that the nature of a martensitic interphase boundary depends upon that of the lattice invariant deformation. If this deformation is achieved by twinning, the "austenite:martensite" interface should be fully coherent, whereas if it occurs by slip or faulting the interface should incorporate a single set of glissile dislocations whose glide accomplishes the deformation. Hence the slip planes of these dislocations are corresponding planes in the two lattices which meet edge-to-edge, at a small angle, at the interphase boundary. In α_1 martensite, however, only the single-set-of-glissile-dislocations specification is fulfilled. Only at the one interphase boundary examined near the edge of a foil (Fig. 46) was the restriction on the slip planes in the two phases satisfied. At the other martensite interfaces examined, while the Burgers vector of the dislocations did lie in the fault plane of the martensite it formed an appreciable angle with respect to even the nearest {110} slip plane in the β' matrix.

A number of geometrical models for martensitic formation of the 9R structure have been published (132,134-136). These are, however, oriented more toward explaining the transformation crystallography in a phenomenological manner than elucidating the atomic mechanisms involved. Attempts have also been made (137,138), though, to describe the transformation with a hard sphere model; these approaches can be more closely related to the atomic details of the transformation. Essential features of these models are: (i) a (011)[011] shear in the bcc matrix which transforms the $(101)_{bcc}$ to a close packed structure; and (ii) shuffles in the transformed planes which convert the structure to the 9R type with a nearly (011) habit plane. Although neither of these models explain the dense random faulting observed in α_1 martensite, this can be incorporated by means of a second lattice invariant deformation (LID). The primary LID will lie in the habit plane (near $(011)_{\beta'}$), while the secondary LID, which generates the stacking faults, will be $(101)_{\beta'}$. The resultant displacement field in the matrix at the dislocations bounding the faults will not lie in a close-packed slip plane of the matrix. Since this

displacement may well not correspond to a stable configuration in the matrix, relaxation is to be anticipated. Such a relaxation could occur to $(110)_{\beta'}$, as observed within the foil. Near the foil edge, on the other hand, the relaxation attending the primary LID may be accommodated at the free surface, thereby permitting Christian's prescription to be followed more closely.

c. Structure of the Lengthwise Interfaces of α Cu-Zn Rods

(1) Introduction

A rod-shaped Widmanstatten morphology develops from β and β' Cu-Zn at temperatures above those at which α_1 plates form (105,139). The rods have the fcc crystal structure of equilibrium α . That α rods are the product of a diffusional rather than a shear transformation now seems to be accepted fairly generally (102,104,140). Hence it is of interest to compare the interphase boundary structures of α rods with those produced by α_1 plates and α_1 martensite.

(2) Experimental Procedure

This investigation was conducted primarily on a 39.3 A/O Zn alloy in specimens isothermally reacted from 500° down to 350°C.

(3) Results and Discussion

Widmanstatten siderods were observed to have evolved from grain boundary α allotriomorphs as part of the same single crystal. Intragranular α rods were also observed and studied. Siderods are largely bounded by planar $\{110\}_{\beta'}$ facets; intragranular rods, fully faceted, are mostly enclosed by $\{110\}_{\beta'}$ interfaces but also exhibit a few of $\{112\}_{\beta'}$ type. However, growth ledges, occurring with rather high frequency, deviate the "macroscopic" habit plane from $\{110\}_{\beta'}$ toward $\{123\}_{\beta'}$. Figs. 47 and 48 are stereoplots summarizing crystallographic analyses of the interfaces bounding two typical α rods.

With TEM it is possible to resolve linear defects in most facets, excepting only those whose macroscopic habit plane deviates significantly from any rational plane. Presumably the inter-dislocation spacing at such interfaces is below the resolution limit (ca. 1.5 nm.) of the present experiments. Usually but not always, only one set of linear defects was observed; a

second set, if present, was much more widely and irregularly spaced. Fig. 49 illustrates some of these observations. Three interfaces are indicated (denoted as a1, a2 and a3) on three adjacent rods. These interfaces are nominally parallel. However, determination of their habit planes shows that they are not. Interface a1, lying between $(121)_{\beta'}$ and $(011)_{\beta'}$, contains an array of linear defects averaging 2.7 nm. apart. Interface a2 lies close to $(121)_{\beta'}$ and exhibits a 3.7 nm. average inter-defect spacing. In the case of interface a3, which is near $(231)_{\beta'}$, the fine linear defects cannot be resolved; only some coarse ledges (note deflections of extinction contours) are observed.

Fig. 50 presents components of a $g \bullet b$ analysis for a typical facet parallel to the long axis of an α rod. This facet is within $2^{\circ}C$ of $(121)_{\beta'}$. In addition to one set of closely spaced linear defects, this interface contains a second set, most easily seen at the "left hand corner" of the interface, whose spacing increases near the corner. Deflection of the extinction contours by the latter defects indicates that they are ledges. A $g \bullet b$ analysis was performed on this interface; a number of the micrographs, taken in different reflections for the analysis, are included in Fig. 50. On the basis of it, the first set of linear defects was concluded to have a Burgers vector parallel to $[101]_{\alpha}$ and $[111]_{\beta'}$. These are evidently misfit dislocations whose Burgers vector lies at an angle to the interface plane. This situation is not unusual (32,119) and presumably results from the particular mechanism through which the misfit dislocations were acquired. As shown in Fig. 51, this mechanism is the adsorption of dislocations from the matrix (here of superdislocations from β'), one which is particularly prone to yielding out-of-plane Burgers vectors (118). At another facet analyzed in detail, the Burgers vector of the single set of misfit dislocations lay in the interface plane, in support of this interpretation. The $g \bullet b$ analysis showed that the displacement field of the second set of linear defects is parallel to $\langle 123 \rangle_{\beta'}$, thus confirming their purely ledge character. The presence of two sets of linear defects with non-parallel Burgers vectors ensures that this interface cannot migrate by shear. Lateral, diffusion-controlled movement of the growth ledges is most likely the operative transformation mechanism.

Fig. 51 also illustrates incipient destabilization of the rod morphology. This was particularly noted at later reaction times. Strain fields associated with individual rods begin to overlap significantly, leading to faulting of the rods. The stacking faults disturb the originally

smooth rod faces and initiate changes in morphology. However, dissociation of the interfaces into corrugated facets suggests that minimization of interfacial energy is likely to be the thermodynamic driving force for the observed instability.

Further interpretation of these results, particularly the evolution of α_1 plates and α as rods, and also the differences in misfit dislocation structure, is still in progress.

2. The Structure of Partially Coherent Fcc:Bcc Boundaries

This problem has been periodically of interest to this contract since its inception. Although the only direct "investment" made by the contract in this topic during the past three years has been support of some of the P.I.'s time, there has nonetheless been considerable ARO-based activity in this area. The next two subsections represent work performed by Dr. Malcolm G. Hall of the Centre for Materials Science, University of Birmingham, U.K., with the personal support of the R.F. Mehl Professorship. Prof. J. Michael Rigsbee of the University of Illinois at Urbana-Champaign, who worked on these problems as the first postdoctoral on this contract (42,140) collaborated on the first portion of it, a comparison of two theoretical analyses of partially coherent fcc:bcc interfacial structures. Dr. Ulrich Dahmen collaborated on experimental studies of these structures in a Cu-Cr alloy. The latter work was largely done by Dr. Hall at the University of California at Berkeley, where the P.I. arranged to "second" him in order to take advantage of a better electron microscope than is available at CMU (a JEOLCO 200CX instead of our JEOLCO 120CX) and also Berkeley's more sophisticated TEM image interpretation capabilities. Dr. Hall worked on the same Cu-Cr alloy as a postdoctoral with the P.I. when the latter was a staff member at the Ford Scientific Laboratory. Although Dr. Hall devised the concept of "structural ledges" at that time (142), neither the resolution of electron microscopes nor the techniques of using them were as yet good enough to resolve either the structural ledges or the misfit dislocations anticipated on planar facets on bcc Cr-rich precipitates formed in the Cu-Cr alloy. With the support of this contract, Dr. Hall tried again several years later to resolve the fcc:bcc interfacial structure in this alloy with a JEOLCO 120 CX during a six-week visit with the P.I. at Michigan Technological University. Only limited success was achieved. After the P.I. moved to Carnegie-Mellon University, Dr. Hall spent six months at Berkeley tackling the same problem on the same specimens as were used at

Ford and Michigan Tech; as will be seen in the second subsection, further progress was made, now to the point where publishable results have been achieved, but a still better instrument will be required in order to solve some of the remaining problems.

a. Comparison of the O-Lattice and Computer Matching Models of Fcc:Bcc Interfaces (with M.G. Hall and J.M. Rigsbee)

(1) Introduction

Two disparate theoretical approaches to predicting the structure of partially coherent fcc:bcc interfaces are now available. One is the computer matching procedure of Rigsbee and Aaronson (RA) (141), based upon concepts due to Hall et al (142) and further developed by Russell et al (143). The other is the O-lattice model conceived by Bollmann (35), first applied to fcc:bcc interfaces by Bollmann and Nissen (144) and subsequently expounded by Ecob and Ralph (ER) (145,146). The two approaches are fundamentally different. RA used computer calculation of the crystal lattice coordinates to delineate directly the matching atomic positions. In the O-lattice calculation, on the other hand, enhanced matching is only indirectly inferred from the size of the O-lattice unit cell. This investigation is a first attempt at comparing the predictions of the two approaches. Further, since certain assumptions used by ER in their application of the O-lattice model require further consideration, the details of the application of this model to fcc:bcc interfaces have to be re-examined before the desired comparison is made.

(2) The O-Lattice Procedure

In this method, the x, y and z coordinates of three non-coplanar atomic positions in each of the two crystal structures are chosen and used to formulate the 3×3 matrices $S^{(1)}$ and $S^{(2)}$ of each structure. If the lattices are taken to be interpenetrating, the nearest neighboring atomic positions closest to the origin are chosen. For an assumed orientation relationship the transformation matrix A is evaluated from (35):

$$(12) \quad A = R \cdot S^{(2)} \cdot S^{(1)}^{-1}$$

where R is a rotation matrix specifying the orientation relationship. The x, y and z coordinates of the basic vectors of the O-lattice cell are then given by (35):

$$(13) \quad x^o = (I - A^{-1})^{-1} b^{(L)} = T^{-1} b^{(L)}$$

where $b^{(L)}$ are the three non-coplanar Burgers vectors of interfacial dislocations and are usually assumed identical to the matrix $S^{(1)}$. Having obtained the O-lattice vectors, the O-lattice cell may be completed by simple summation and interfaces can be assigned and assessed in terms of inter-dislocation spacings, geometry and habit planes. However, the size, shape and symmetry of the O-lattice cell are markedly affected by the choices of $S^{(1)}$ and $S^{(2)}$; quite different interfaces can be generated by the particular selections made. Hence the rationale for making these choices is now further investigated.

(3) Choice of $S^{(1)}$ and $S^{(2)}$

Provided that corresponding atom positions are employed in each structure, the same transformation matrix A (and hence T) applies to any three basic non-coplanar vectors comprising $S^{(1)}$ or $S^{(2)}$. Six $a/2 <110>$ vectors in the fcc lattice and four $a/2 <111>$ as well as two $a <100>$ in bcc comprise the smallest fcc vectors and their bcc counterparts. Having evaluated T for a given orientation relationship, it is then only necessary to assume a set of values for $b^{(L)}$ to obtain the O-lattice positions corresponding to Eq. (13). The three $b^{(L)}$ vectors generate the O-lattice cell.

Fig. 52 shows how three different O-lattice cells are derived for one orientation relationship simply by changing the assumed values of $b^{(L)}$. Although the cell points lie on the same lattice, no cell is fundamental to the other two, and more importantly the faces of the unit cells delineate different planes in the lattice. Since there appears to be no a priori means through which one cell or $S^{(1)}$, $S^{(2)}$ combination may be selected so as to obtain the lowest energy interface, it is necessary to consider how one cell may be used to generate all possible interfaces or how the procedure can be modified so that all interfacial situations are automatically described.

(4) Assignment of Interfaces

(a) Cell Sectioning

This should be done so that contact with the O-lattice points is maximized while the number of intersections with the cell walls is minimized. Sections formed by $\{001\}^o$ planes will satisfy this criterion, as will $\{110\}^o$ (where the superscript o designates an

O-lattice plane), whereas $\{111\}^o$ and other planes of higher indices will not. Nine sections considered in detail are illustrated in Fig. 53. Four sets of cell walls (nos. 1-3 and 6) are $\{110\}^o$ planes. However, nos. 7-9 in this Figure pass through O-lattice points formed by the sum of two of the basic vectors, e.g.

$$(14) \quad x_4^o = x_1^o + x_2^o$$

According to Bollmann's "duality relationship", these cell walls contain a dislocation array whose Burgers vector is the sum of the other two:

$$(15) \quad b_4 = b_1 + b_2$$

In an fcc lattice, this reaction will yield energetically unfavorable $a/2<112>$ Burgers vectors. On the other hand, boundaries 4-6 are produced by a reaction of the type:

$$(16) \quad b_5 = b_1 - b_2$$

Such a reaction yields $a/2<110>$ dislocations. For an assumed $S^{(1)}$, $S^{(2)}$, six interfaces containing only $a/2<110>$ dislocations are therefore derived for each unit cell by this procedure: three cell walls and three $\{110\}^o$ sections. This result may be compared with the more rigorous approach derived next.

(b) Dislocation Pairs

For every vector in the b -lattice there is a corresponding O-lattice vector. An interface may be formed by the interaction of two O-lattice vectors. Accordingly, all possible interfaces containing $a/2<110>$ dislocations will be constructed by considering the b -vectors in pairs. Fig. 54 shows the 15 interface descriptions produced in this manner. These interfaces, however, yield only 7 different habit planes. Three habit planes are found to have a unique dislocation structure while the remaining four each have three possible structures.*** Fig. 55 locates the habit planes derived in this manner, using the lattice parameters for pure Cu and pure Cr and assuming that the Nishiyama-Wasserman orientation relationship obtains; Table II lists the characteristics of all 15 interfaces. Fig. 56 shows the variation of the habit plane and the

***Minimum dislocation line length per unit area is probably the best means now available for selecting which of each set of three is preferred.

O-lattice vector directions for a range of orientation relationships, θ , defined as the angle between $[110]_{\text{fcc}}$ and $[100]_{\text{bcc}}$, plotted on a $(111)_{\text{fcc}}$ stereographic projection. The habit planes can be seen to lie in four distinct regions of the stereogram. The dislocation structure of each of the three best interfaces, measured in terms of the Bollmann P parameter ($P = \sum (b_i^2/d_i^2)$, where d_i is the distance between parallel dislocations with Burgers vector b_i), is shown in Fig. 57.

The following aspects of these structures are of particular interest:

- (i) For the Nishiyama-Wasserman ($\theta = 0^\circ$) orientation relationship, the best interface is near $(533)_{\text{fcc}}$ with orthogonal sets of dislocations spaced 2.5 and 25 nm apart, in good agreement with the graphical analyses of these interfaces (142,143), the "manual" equivalent of the RA computer modeling treatment.
- (ii) For most orientation relationships, $(111)_{\text{fcc}}$ is only the third best interface.
- (iii) For all orientation relationships investigated, spacings between dislocations in the finer array vary only between 1.5 and 2.5 nm.
- (iv) At $\theta = \pm 5.7^\circ$ there is perfect matching along lines in the interface ca. 5° from $[110]_{\text{fcc}}$.

(5) Comparison with RA

ER (146) claimed poor agreement between the O-lattice and the RA analyses. This investigation showed, however, that the two methods yield nearly identical results.

Figs. 58a-d compare the computer drawn interfaces of RA at four different orientation relationships (expressed as values of θ) with their respective O-lattice cells. Excellent agreement is seen to have been obtained between the two techniques. One O-lattice point is produced for each center of best fit; the O-lattice point is always located at the symmetry point of the best fit region, whose essential atomic sites are included in these Figures.

Fig. 57 shows that the inter-dislocation spacing of the coarse array of misfit dislocations is usually one-half to one order of magnitude larger than that of the fine array. The need for the coarsely spaced arrays was noted by RA but not calculated, in part because of the very large additional amount of computer calculations and plotting required. However, this omission, which was criticized by ER, is easily remedied and is without effect upon the finely spaced dislocation arrays.

The spacings of the finer set of dislocations, calculated by means of both the O-lattice and the RA computer matching approaches, are shown in Fig. 59 as a function of θ at three typical lattice parameter ratios. Agreement between the predictions of the two approaches is seen to be very good at small θ values but to become less satisfactory, especially at $a_{\text{fcc}}/a_{\text{bcc}} = 1.32$, when θ approaches ca. 5°. However, it is at this angle that $\det T$ approaches zero, where the O-lattice calculation becomes of doubtful accuracy.

Hence it becomes apparent that the ER criticism of RA to the effect that they used a method "founded largely on concepts which can only be associated with incoherent boundaries" is unfounded and that the O-lattice and computer matching techniques are in fact very nearly equivalent. Further, re-examination of the ER usage of the O-lattice method to calculate polar γ -plots and Wulff constructions from them (145,146) shows that the effects of the various vectors which can be used to formulate $S^{(1)}$ and $S^{(2)}$, considered in detail during the present study, were only examined in casual fashion by ER. This alone makes the significance of the γ -plots as supposedly representing the minimum energy fcc:bcc interface as a function of boundary orientation very doubtful indeed. Taking also into consideration the separate issue of the dubious value of the P and R parameters for representing the dislocation component of the interphase boundary energy, it appears that the ER investigations may amount to no more than an interesting first attempt upon a very important problem which surely deserves closer attention.

b. Structure of Facets on Bcc Cr-rich Precipitates in a Cu-Cr Alloy (with M.G. Hall and U. Dahmen)

(1) Introduction

This investigation was undertaken to ascertain whether or not the structure of partially coherent fcc:bcc interphase boundaries between two disordered substitutional solid solutions is the same as that between two disordered interstitial solid solutions. The detailed study of Rigsbee and Aaronson (42), funded by this contract, of the structure of austenite:ferrite boundaries in an Fe-C-Si alloy, served as the prototype for the interstitial solid solution case. An incomplete study of austenite:ferrite boundaries in a duplex stainless steel by Howell et al (147) has tentatively shown significant difference with respect to the results obtained on the Fe-C-Si alloy, of which the most important is the presence of structural ledges in the interstitial but

not in the substitutional alloy steel. Hall et al (142) attempted in 1971 and 1972 to investigate the interfacial structure of planar facets produced during formation of bcc Cr-rich precipitates in the fcc matrix of a Cu-0.3% Cr alloy, using a Philips 200 electron microscope at the Scientific Laboratory of Ford Motor Co. Only the coarse (several score nm. spacing) array of misfit dislocations discussed in the preceding subsection was detected. The present study was undertaken for the purposes of resolving the finely spaced dislocation array and ascertaining whether or not structural ledges are present. The investigation was undertaken at the University of California at Berkeley with a Siemens 102 electron microscope particularly adapted and reserved for research requiring very high resolution. This microscope is equipped with a high-brightness LaB₆ electron emitter and a $\pm 45^\circ$ double tilt stage. As will now be shown, this much improved instrument combined with the fruits of a decade's advances in the techniques of using TEM yielded much improved results. However, this research has also made clear than an instrument of still higher resolution capability will have to applied before the structure of partially coherent fcc:bcc interfaces in Cu-Cu is fully resolved.

(2) Experimental Procedure

A Cu-0.3% Cr alloy was employed. Specimens were solution annealed at 900°C, then isothermally reacted for long times at 700°C and finally quenched in iced water. Two different methods of determining orientation relationships were employed. One method, previously used in the Fe-C-Si study (42), was based on tilting to all accessible $\langle 111 \rangle_{\text{fcc}}$ zone axes and measuring the relative orientation of the superimposed $\{110\}_{\text{bcc}}$ diffraction pattern. This method permitted direct measurement from the diffraction pattern of the angle θ between $(002)_{\text{bcc}}$ and $(022)_{\text{bcc}}$. Usually, multiple diffraction between these two diffraction spots exaggerated the rotation, thereby making this method accurate to better than $\pm 0.2^\circ$ (148). When the specific $\{111\}_{\text{fcc}}$ planes parallel to $\{110\}_{\text{bcc}}$ were not accessible, a $\langle 110 \rangle_{\text{fcc}}$ zone axis which contained a variant of $\{111\}_{\text{fcc}}$ parallel to $(110)_{\text{bcc}}$ was tilted in, and adjusted until a symmetrical precipitate diffraction pattern was obtained. Kikuchi lines from the matrix were then used to measure the orientation of the fcc phase. Limitations on the obtainable symmetry of the precipitate diffraction pattern restricted the accuracy of this method to ca. $\pm 1^\circ$.

(3) Results

Howell et al (147) found that $\{111\}_{\text{fcc}}$ and $\{110\}_{\text{bcc}}$ are misoriented by up to a few degrees in a duplex stainless steel, whereas these planes are accurately parallel in Fe-C-Si (42). This question was accordingly investigated with some care in Cu-Cr. Fig. 60 shows that lattice fringes of $\{111\}_{\text{fcc}}$ and $\{110\}_{\text{bcc}}$ are continuous across the interphase boundary. The two sets of fringes are also seen to have parallel projections, indicating that the planes are parallel about an axis normal to the plate. Since the two sets of planes are simultaneously observed under the same specimen and beam tilting conditions, they must be precisely parallel about an axis in the image plane. Note also that the interphase boundary (which runs approximately left to right in the micrograph) is not parallel to the fringes, providing conclusive evidence that the average position of the interface does not lie along the close packed planes of either structure. Hence we conclude that a $\{111\}_{\text{fcc}}$ and an $\{110\}_{\text{bcc}}$ plane are indeed accurately parallel in Cu-Cr, as in Fe-C-Si but not in a duplex stainless steel.

Approximately 20 precipitates were studied during the current investigation (as contrasted with 7 in the earlier research (142)); the range of orientation relationships observed, $\theta = 0^\circ$ (Nishiyama-Wasserman) to $\theta = 5 1/4^\circ$ (Kurdjumow-Sachs), was the same as that previously found.

An important qualitative observation is first noted by means of Fig. 61: whatever the value of θ (see the caption for this Figure), finely spaced dislocation arrays, ranging from 1 nm. (Fig. 61c) to 2.5 nm. (Fig. 61b), were observed. Although for the four examples shown in this Figure imaging was not possible in a sufficient number of reflections to permit a $g \bullet b$ analysis, in each case it was possible to image the structures in at least two g vectors and thereby to show with certainty that the contrast was due to interfacial dislocations rather than Moire patterns.

Interfaces on three precipitates were imaged with enough reflection to allow $g \bullet b$ analysis and also accurate measurement of their orientation relationship. Figs. 62-64 and Table III summarize the observations made and the main results obtained on one of these precipitates, a lath with the $\theta = 0^\circ$ (N-W) orientation relationship. This morphology and orientation relationship occurred most frequently, and the agreement between the experimental observations and those predicted by computer modeling for this orientation relationship and lattice parameter ratio (149)

and translated into diffraction contrast intensities was the best secured in this investigation. As may be seen from inspection of Table III, only the weak contrast observed in a $(111)_{\text{fcc}}$ reflection represents a definite disagreement with theoretical predictions. The fine fringe pattern in Figs. 63a and 64a may have originated in interference between the operating reflection and dislocation arrays in the interface (147,149). Another important result is displayed in Fig. 63b: several linear defects may be observed which exhibit much stronger contrast than the dislocation structure. Extinction contour displacement is also observed at these defects, indicating an abrupt change in thickness. From measurements thus made, the height of these ledges was 2.5-3.5 nm.; one can be virtually certain that they are growth ledges, as predicted by a general theory of precipitate morphology (15,32).

Detailed analyses were also made of an equi-axed Cr precipitate with a $\theta = 2^\circ$ orientation relationship and a variant of the lath morphology with an orientation relationship near to that of Kurdjumow-Sachs ($5 1/4^\circ$). At $\theta = 2^\circ$, two non-orthogonal arrays of dislocations, spaced 2.3 nm. and 1.1 nm. apart, were observed. This structure does not correspond to any of the interfaces derived in the O-lattice study of fcc:bcc interfaces summarized in the preceding subsection. However, a higher energy structure was devised which is consistent with the observed dislocation morphology. On the other hand, Table IV indicates a significant number of disagreements between the contrast anticipated and that observed from the misfit dislocations, assumed to be $a/2<110>$, and also the predicted and experimentally found geometry of the two arrays. The third morphology studied in detail is shown in six different g vectors in Fig. 65. The more widely spaced fringes are ca. 2.5 nm. apart (though this spacing can be as large as 4.0 nm.) and do not become extinct at any of the reflections studied. The more closely spaced fringes are only ca. 0.8 nm. apart, too fine to permit a detailed $g \bullet b$ analysis. It seems possible that the former fringes correspond to structural ledges.

(4) Discussion

Failure of partially coherent interfacial structures to correspond in Burgers vector, spacing between misfit dislocations, geometry of the dislocation array, etc. to predictions made upon the basis of minimum interfacial energy is familiar from studies on interphase boundaries much simpler than those attending fcc:bcc transformations (32,119). Hence

it is not surprising that the predicted low energy configurations were not always observed in the present study. However, as indicated by Table IV, characterization of the observed structures was not complete; it remains to be established whether structural ledges are always absent (as seems to be the case in duplex stainless steels (147)) or always present (as was definitely found in Fe-C-Si (42)). The very fine spacings of some of the defect structures, e.g., Fig. 65, and the 1-3 atomic plane height expected for structural ledges (141) could not be adequately characterized with a Siemens 102 microscope. A third investigation of interphase boundary structure in Cu-0.3% Cr, using the JEOL 1000 atomic resolution TEM now being installed at Berkeley, now appears to be required. The P.I. will attempt to develop an informal arrangement for this enterprise through Dr. Ronald Gronsky.

Bibliography

1. R.W.K. Honeycombe, Met. Trans., 7A, 915 (1976).
2. R.W.K. Honeycombe, Met. Sci., 14, 201 (1980).
3. G.R. Purdy, Acta Met., 26, 477, 487 (1978).
4. K.R. Kinsman and H.I. Aaronson, Transformation and Hardenability in Steels, p. 39, Climax Molybdenum Co., Ann Arbor, MI. (1967).
5. H.I. Aaronson, The Mechanism of Phase Transformations in Crystalline Solids, p. 270, Institute of Metals, London (1969).
6. J.R. Bradley and H.I. Aaronson, Met. Trans., 12A, 1729 (1981).
7. M. Hillert, Internal Report, Swedish Institute for Metals Research, Stockholm, Sweden (1953).
8. A. Hultgren, Jern. Ann., 135, 403 (1951).
9. M. Hillert, ibid, 136, 25 (1952).
10. E. Rudberg, Ibid, 137, 91 (1952).
11. J.B. Gilmour, G.R. Purdy and J.S. Kirkaldy, Met. Trans., 3, 1455 (1972).
12. K. Lucke and K. Detert, Acta Met., 5, 628 (1957).
- 12a. K. Lucke and H.P. Stuwe, ibid, 19, 1087 (1971).
13. J.W. Cahn, ibid, 10, 789 (1962).
14. K.R. Kinsman and H.I. Aaronson, Met. Trans., 4, 959 (1973).
15. H.I. Aaronson, Decomposition of Austenite by Diffusional Processes, p 387, Interscience, New York (1962).

16. J.R. Bradley, J.M. Rigsbee and H.I. Aaronson, *Met. Trans.*, 8A, 323 (1977).
17. P.G. Boswell, K.R. Kinsman and H.I. Aaronson, unpublished research, Ford Motor Co., (1968).
18. G.J. Shiflet and H.I. Aaronson, to be submitted to *Met. Trans.*
19. R.F. Hehemann and A.R. Troiano, *Metal Progress*, 70 (2), 97 (1956).
20. R.F. Hehemann, Phase Transformations, p. 397, ASM, Metals Park, OH (1970).
21. G.J. Shiflet, H.I. Aaronson and J.R. Bradley, *Met. Trans.*, 12A, 1743 (1981).
22. M. Guttmann and D. McLean, Interfacial Segregation, p. 261, ASM, Metals Park, OH (1979).
23. J. Fridberg, L.-E. Torndahl and M. Hillert, *Jern. Ann.*, 153, 263 (1969).
24. M. Enomoto and H.I. Aaronson, unpublished research, Carnegie-Mellon University (1982).
25. W.F. Lange III and H.I. Aaronson, *Met. Trans.*, in press.
26. J.S. Kirkaldy, *Met. Trans.*, 4, 2327 (1973).
27. C.H. Johansson and J.O. Linde, *Ann. Phys.*, Paris, 25 1 (1936).
28. R. Smith and J.S. Bowles, *Acta Met.*, 8, 405 (1960).
29. A.J. Pedraza and J. Kittl, *ibid*, 24, 835 (1976).
30. H.I. Aaronson and K.R. Kinsman, *ibid*, 25 367 (1977).
31. J.S. Bowles and C.M. Wayman, *ibid*, 27, 833 (1979).
32. H.I. Aaronson, C. Laird and K.R. Kinsman, Phase Transformations, p. 313, ASM, Metals Park, OH (1970).
33. T.B. Massalski, *ibid*, p. 433.
34. M.R. Plichta and H.I. Aaronson, *Acta Met.*, 28, 1041 (1980).
35. W. Bollmann, Crystal Defects and Crystalline Interfaces, Springer-Verlag, Berlin, FRG (1970).
36. K.K. Kelley, *Bur. Min. Bull.*, 584, 167 (1959).
37. J.W. Cahn and J.E. Hilliard, *Jnl. Chem. Phys.*, 31 688 (1959).
38. J.H. van der Merwe, *Jnl. App. Phys.* 34 117, 123 (1963).
39. E.B. Hawbolt and T.B. Massalski, *Met. Trans.*, 1 2315 (1970).
40. J.D. Ayres and D.C. Joy, *Acta Met.*, 20, 1371 (1972).

41. J.D. Ayres, *Acta Met.*, 28, 1513 (1980).
42. J.M. Rigsbee and H.I. Aaronson, *ibid.*, 27 365 (1979).
43. B.P.J. Sandvik and C.M. Wayman, *Met. Trans.*, 14A, 823 (1983).
44. H.I. Aaronson, The Mechanism of Phase Transformations in Crystalline Solids, p. 270, Institute of Metals, London (1969).
45. G.J. Shiflet and H.I. Aaronson, Proc. of an Int. Conf. on Solid-Solid Phase Trans., p. 1581, TMS-AIME, Warrendale, PA. (1983).
46. F. Wever and E. Lanage, *Mitt. K.-W. Inst. Eisenforschung*, 14, 71 (1932).
47. F. Wever and W. Jellinghaus, *ibid*, p. 85.
48. F. Wever and W. Jellinghaus, *ibid*, p. 105.
49. F. Wever and W. Jellinghaus, *ibid*, 15, 167 (1933).
50. S. Steinberg and V. Zyuzin, *Arch. Eisenhuttenwesen*, 7, 537 (1934).
51. S. Steinberg and V. Zyuzin, *Rev. Met.*, 31 554 (1934).
52. V.D. Sadovski, *Trudy UFAN*, (4) and (5), 1945, and (13), 1949.
53. W.T. Griffiths, L.B. Pfeil and N.P. Allen, Second Report of the Alloy Steels Research Committee, Spec. Rep. No. 24, p. 343, Iron and Steel Inst., London (1939).
54. N.P. Allen, L.B. Pfeil and W.T. Griffiths, *ibid*, p. 369.
55. E.P. Klier and T. Lyman, *Trans. AIME*, 158, 394 (1944).
56. T. Lyman and A.R. Troiano, *Trans. ASM*, 37, 402 (1946).
57. T. Lyman and A.R. Troiano, *Trans. AIME*, 162, 196 (1945).
58. J.E. Hilliard and J.W. Cahn, *Trans. TMS-AIME*, 221, 344 (1961).
59. R.F. Hehemann, priv. comm. (1969).
60. N.N. Breyer, priv. comm. (1969).
61. J.R. Bradley, T. Abe and H.I. Aaronson, *Rev. Sci. Inst.*, 53, 98 (1982).
62. F.G. Berry and R.W.K. Honeycombe, *Met. Trans.*, 1, 3279 (1970).
63. H.K.D.H. Bhadeshia, Proc. of an Int. Conf. on Solid-Solid Phase Trans., p. 1041, TMS-AIME, Warrendale, PA. (1983).
64. C. Atkinson, H.B. Aaron, K.R. Kinsman and H.I. Aaronson, *Met. Trans.*, 4, 783 (1973).

65. M. Hillert and L.I. Staffansson, *Acta Chem. Scand.*, 24, 3618 (1970).
66. H.I. Aaronson and H.A. Domian, *Trans., TMS-AIME*, 236, 781 (1966).
67. M. Hillert, *Met. Trans.*, 3, 2729 (1979).
68. J. Crank, *The Mathematics of Diffusion*, 2nd Ed., p. 69, Oxford (1975).
69. M. Hillert, *Decomposition of Austenite by Diffusional Processes*, p. 197, Interscience, NY (1962).
70. G.J. Jones and R.K. Trivedi, *Jnl. App. Phys.*, 42, 4299 (1971).
71. C. Zener, *Jnl. App. Phys.*, 20, 850 (1949).
72. H.B. Aaron and H.I. Aaronson, *Acta Met.*, 16, 789 (1968).
73. A.T. Davenport and R.W.K. Honeycombe, *Proc. Roy. Soc.*, 322, 191 (1971).
74. K. Campbell and R.W.K. Honeycombe, *Met. Sci.*, 8, 197 (1974).
75. F.S. Ham, *Jnl. App. Phys.*, 30, 1518 (1959).
76. J. Crank, *The Mathematics of Diffusion*, 2nd Ed., p.76, Oxford (1975).
77. K.W. Andrews, *JISI*, 203, 721 (1965).
78. H.I. Aaronson and C. Wells, *Trans., AIME*, 206, 1216 (1956).
79. H.I. Aaronson, W.B. Triplett and G.M. Andes, *ibid*, 209, 1227 (1957).
80. D.J. Dyson, S.R. Keown, D. Raynor and J.A. Whiteman, *Acta Met.*, 14, 867 (1966).
81. W. Pitsch and A. Schrader, *Arch. Eisenhuttenwesen*, 29, 1715 (1958).
82. Y.A. Bagaryatskii, *Doklady Akademii Nauk SSR*, 73, 1161 (1950).
83. G.R. Srinivasan and C.M. Wayman, *Acta Met.*, 16, 609, 621 (1968).
84. D.H. Huang and G. Thomas, *Met. Trans.*, 8A, 1661 (1977).
85. G.J. Shiflet, Ph.D. Thesis, Michigan Technological University (1981).
86. M. Hillert, *The Mechanism of Phase Transformations in Crystalline Solids*, p. 231, Institute of Metals, London (1969).
87. T. Obara, G.J. Shiflet and H.I. Aaronson, *Met. Trans.*, in press.
88. J.R. Bradley, G.J. Shiflet and H.I. Aaronson, *Proc. of an Int. Conf. on Solid-Solid Phase Trans.*, p. 819, TMS-AIME, Warrendale, PA. (1983).
89. J.S. Kirkaldy, *Can. Jnl. Phys.*, 36, 907 (1958).
90. G.R. Purdy, D.H. Weichert and J.S. Kirkaldy, *Trans. TMS-AIME*, 230, 1025 (1964).

91. R.C. Sharma and G.R. Purdy, *Met. Trans.*, 4, 2303 (1973).
92. J.S. Kirkaldy, Decomposition of Austenite by Diffusional Processes, p. 39, Interscience, NY (1962).
93. H.I. Aaronson, H.A. Domain and G.M. Pound, *Trans. TMS-AIME*, 236, 768 (1966).
94. T. Wada, ASM Handbook: Metallography, Structures and Phase Diagrams, 8, (8th ed.), 409 (1973).
95. T. Abe, H.I. Aaronson and G.J. Shiflet, unpublished research, Michigan Technological University (1979).
96. B. Uhrenius, Hardenability Concepts with Applications to Steel, p. 28, TMS-AIME (1978).
97. M. Hillert and B. Sundman, *Acta Met.*, 24, 731 (1976).
98. *Journal of Metals*, to be published in Sept. 1983.
99. L. Kaufman, S.V. Radcliffe and M. Cohen, Decomposition of Austenite by Diffusional Processes, p. 313, Interscience, NY (1962).
- 99a. D. McLean, Grain Boundaries in Metals, p. 116, Oxford (1957).
- 99b. J. Friedel, *Advan. Phys.*, 3, 446 (1954).
100. R.D. Garwood, *Jnl. Inst. Metals*, 83, 64 (1954).
101. I. Cornelis and C.M. Wayman, *Acta Met.*, 22, 301 (1974).
102. E.P. Simonen and R. Trivedi, *ibid*, 25, 945 (1977).
103. T. Ko and S.A. Cottrell, *JISI*, 172, 307 (1972).
104. C.M. Wayman, Phase Transformations, p. 59, ASM, Metals Park, OH (1970).
105. P.E.J. Flewitt and J.M. Towner, *J.I.M.*, 95, 273 (1967).
106. I. Cornelis and C.M. Wayman, *Scripta Met.*, 7, 579 (1973).
107. G.W. Lorimer, G. Cliff, H.I. Aaronson and K.R. Kinsman, *Scripta Met.*, 9, 271 (1975).
108. M.M. Kostic and E.B. Hawbolt, *ibid*, 9, 1173 (1975).
109. G.W. Lorimer, G. Cliff, H.I. Aaronson and K.R. Kinsman, *ibid*, 9, 1175 (1975).
110. P. Doig and P.E.J. Flewitt, Proc. of an Int. Conf. on Solid-Solid Phase Trans., p. 983, TMS-AIME, Warrendale, PA. (1983).
111. K.C. Chattopadhyay, *ibid*, p. 990.
112. B.C. Muddle and H.L. Fraser, *ibid*, p. 987.

113. J.W. Christian, Physical Properties of Martensite and Bainite, p. 1, Iron and Steel Institute, London (1965).
114. A.L. Titchener and M.B. Bever, Trans. AIME, 200, 303 (1954).
115. E. Hornbogen and H. Warlimont, Acta Met., 15, 943 (1967).
116. H. Pops and T.B. Massalski, Trans. TMS-AIME, 230, 1662 (1964).
117. G.C. Weatherly, P. Humble and D. Borland, Acta Met., 27, 1815 (1979).
118. G.C. Weatherly and R.B. Nicholson, Phil Mag., 17, 801 (1968).
119. H.I. Aaronson, Journal of Microscopy, 102, 275 (1974).
120. G.C. Weatherly, Can. Met. Quart., 8, 105 (1969).
121. G.C. Weatherly and C.M. Sargent, Phil. Mag., 22, 1049 (1970).
122. G.C. Weatherly, Acta Met., 19, 181 (1971).
123. G.C. Weatherly and T.D. Mok, Surface Sci., 31, 335 (1972).
124. R. Hutchings, M. Loretto, I.P. Jones and R.E. Smallman, Ultramicroscopy, 3, 401 (1979).
125. H. Kubo and C.M. Wayman, Met. Trans., 10A, 633 (1979); Acta Met., 28, 395 (1980); Acta Met., 28, 405 (1980).
126. P. Doig and P.E. J. Flewitt, Proc. of an Int. Conf. on Solid-Solid Phase Trans., p. 983, TMS-AIME, Warrendale, PA. (1983).
127. C. Hammond and P.M. Kelly, Acta Met., 17, 869 (1969).
128. J. Perkins, Phil. Mag., 30, 379 (1974).
129. S. Chakraborty and C.M. Wayman, Acta Met., 25, 989 (1977).
130. R. Sinclair and H.A. Mohamed, ibid, 26, 623 (1978).
131. K.M. Knowles and D.A. Smith, ibid, 29, 1445 (1981).
132. I. Cornelis and C.M. Wayman, Acta Met., 22, 291 (1974).
133. S. Sato and K. Takezawa, Trans. J.I.M., Supp. 9, 925 (1968).
134. L. Delaey, S. van Paemel and I. Struyve, Scripta Met., 6, 507 (1972).
135. K. Otsuka and C.M. Wayman, ibid, 9, 1017 (1975).
136. S. Kagiwara, Trans. Japan Inst. Metals, 17, 435 (1976).
137. M. Ahlers, Zeit. Metallkunde, 10, 636 (1974).

138. G.B. Olson and M. Cohen, Met. Trans., 7A, 1897 (1976).
139. P.E. Repas and R.F. Hehemann, Tech. Rep. No. 6 to ONR (June, 1967).
140. A. Crosky, P.G. McDougall and J.S. Bowles, Acta Met., 31, 603 (1983).
141. J.M. Rigsbee and H.I. Aaronson, Acta Met., 27, 351 (1979).
142. M.G. Hall, H.I. Aaronson and K.R. Kinsman, Surface Science, 31, 257 (1972).
143. K.C. Russell, M.G. Hall, K.R. Kinsman and H.I. Aaronson, Met. Trans., 5, 1503 (1974).
144. W. Bollmann, Phys. Stat. Sol. (a), 21, 543 (1974).
145. R.C. Ecob and B. Ralph, Proc. Nat. Acad. of Sci. USA, 77 (no. 4), 1749 (1980).
146. R.C. Ecob and B. Ralph, Acta Met., 29, 1037 (1981).
147. P.R. Howell, P.D. Southwick, R.C. Ecob and R.A. Ricks, Proc. of an Int. Conf. on Solid-Solid Phase Trans., p. 591, TMS-AIME, Warrendale, PA. (1983).
148. M.G. Hall, U. Dahmen and H.I. Aaronson, unpublished research (1982).
149. C.T. Forwood and L.M. Clarebrough, Phil. Mag., 37A, 837 (1978).

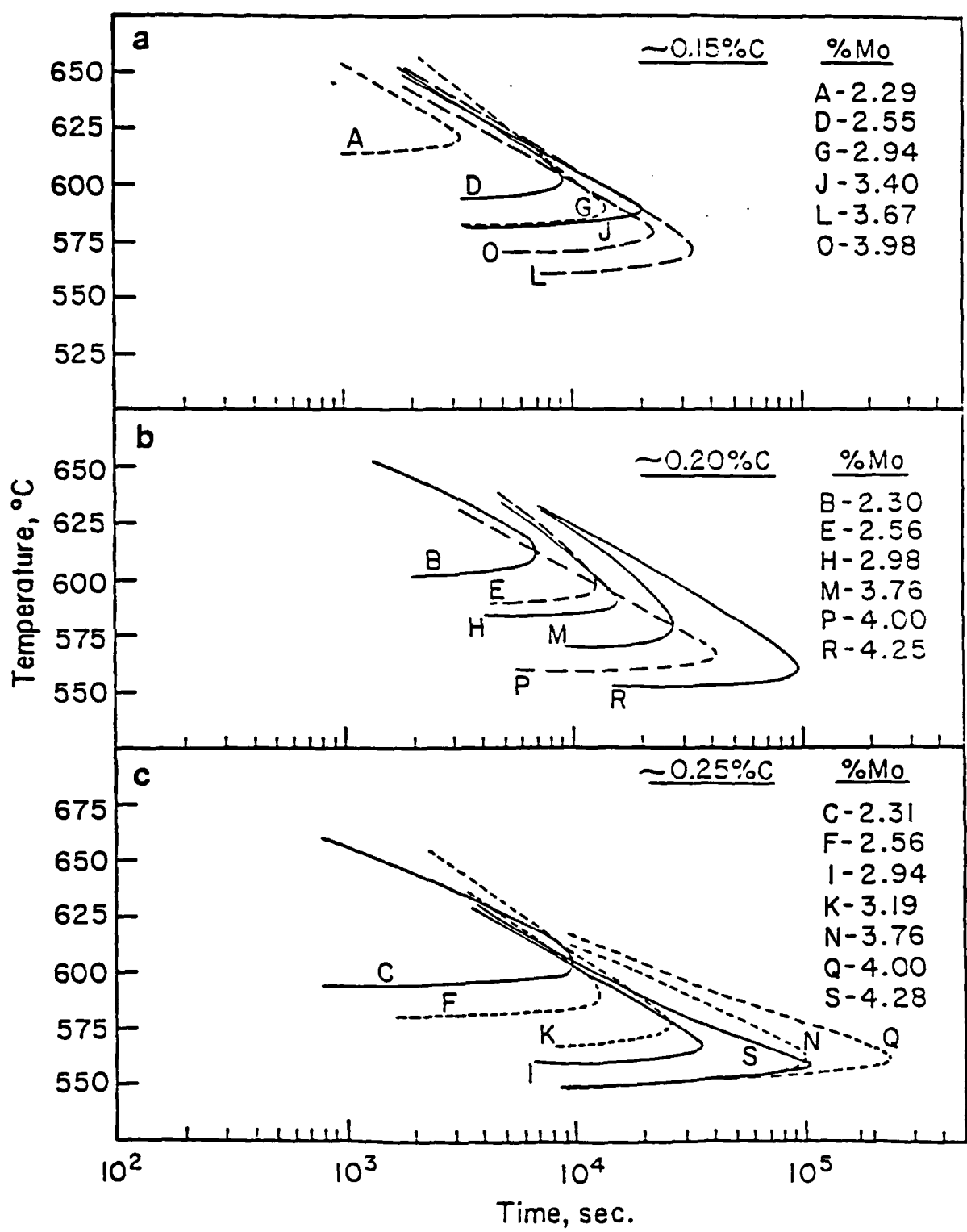


Figure 1



Figure 2

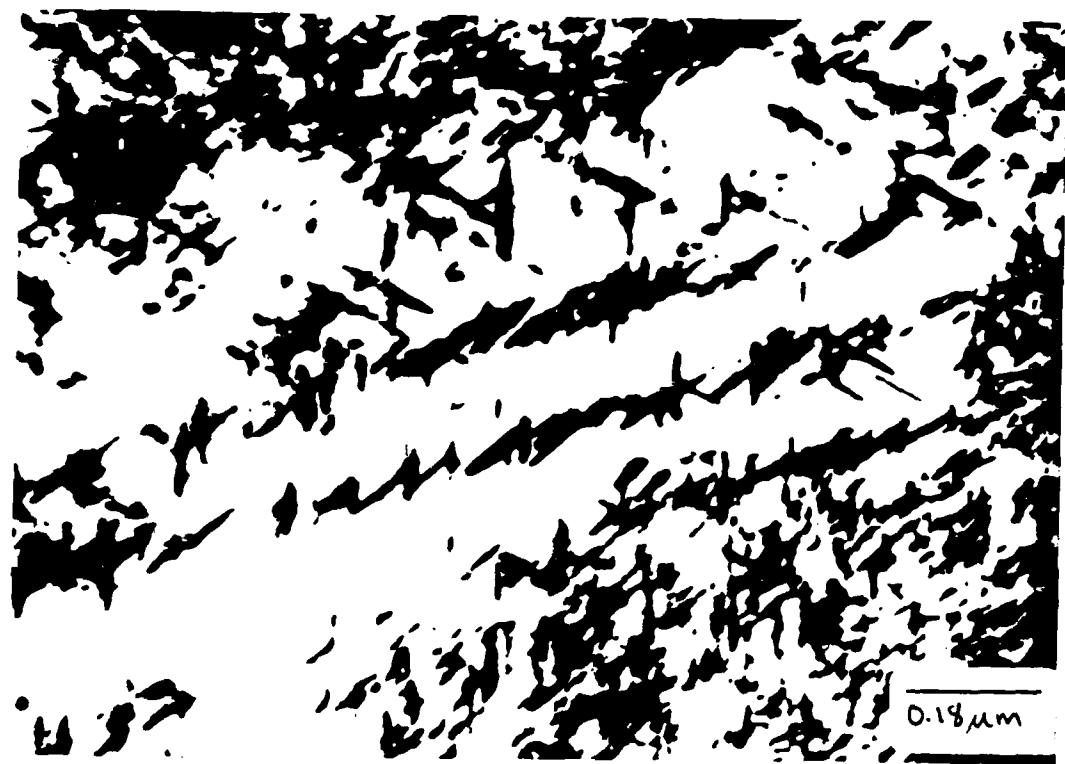


Figure 3



Figure 4

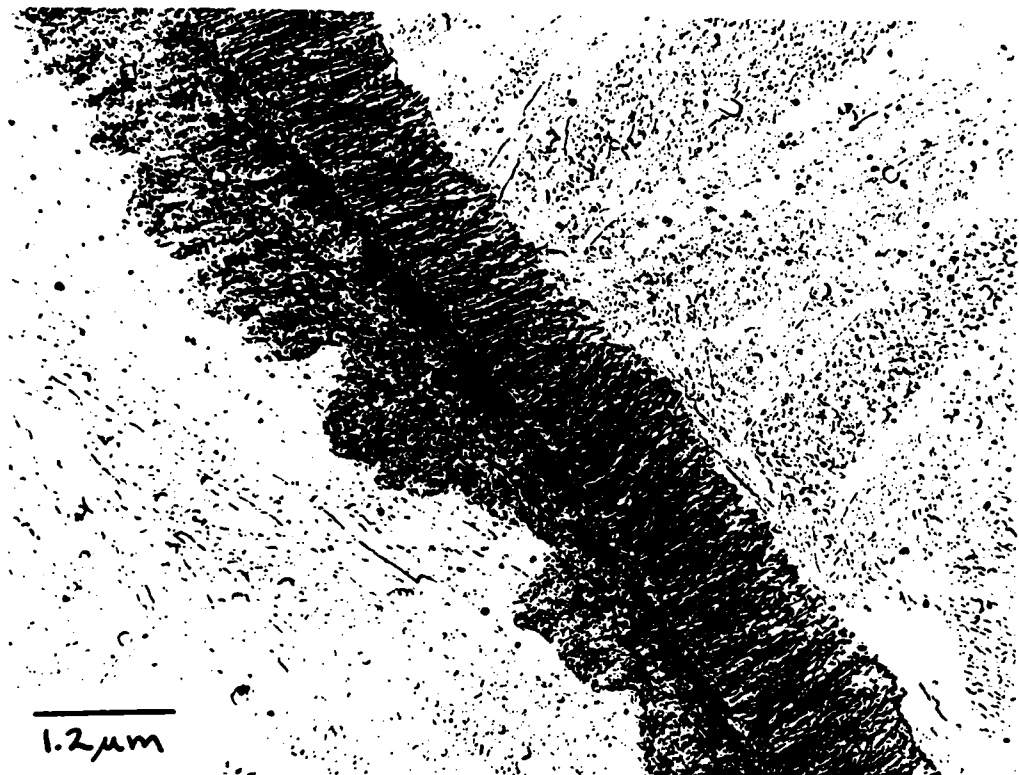


Figure 5

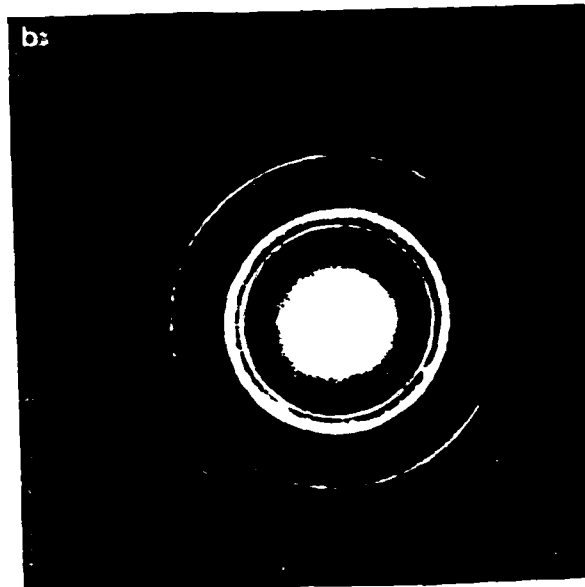
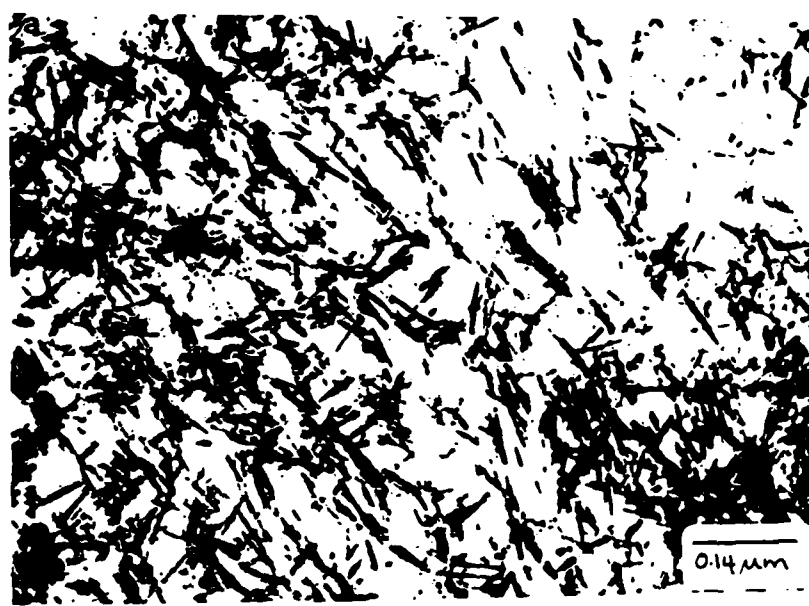


Figure 6

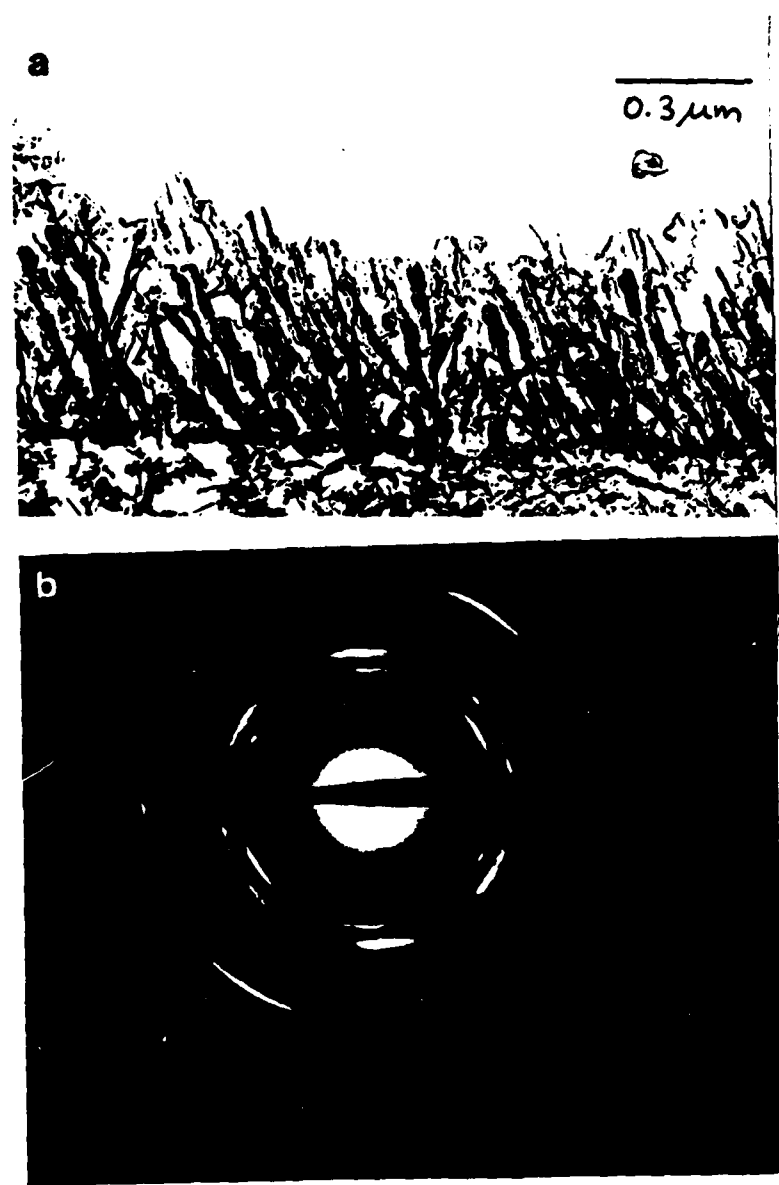


Figure 7

100
90
80
70
60
50
40
30
20
10
0

Fe-0.19C-2.30Mo

▼ 560 °C ▼ 630 °C
● 570 °C ● 640 °C
△ 580 °C × 650 °C
▲ 590 °C □ 675 °C
□ 600 °C ▲ 700 °C
■ 610 °C △ 725 °C
▽ 620 °C

Volume Fraction, %

10³ 10⁴ 10⁵ 10⁶
1h 6h 15h 2d 4d

Time, seconds

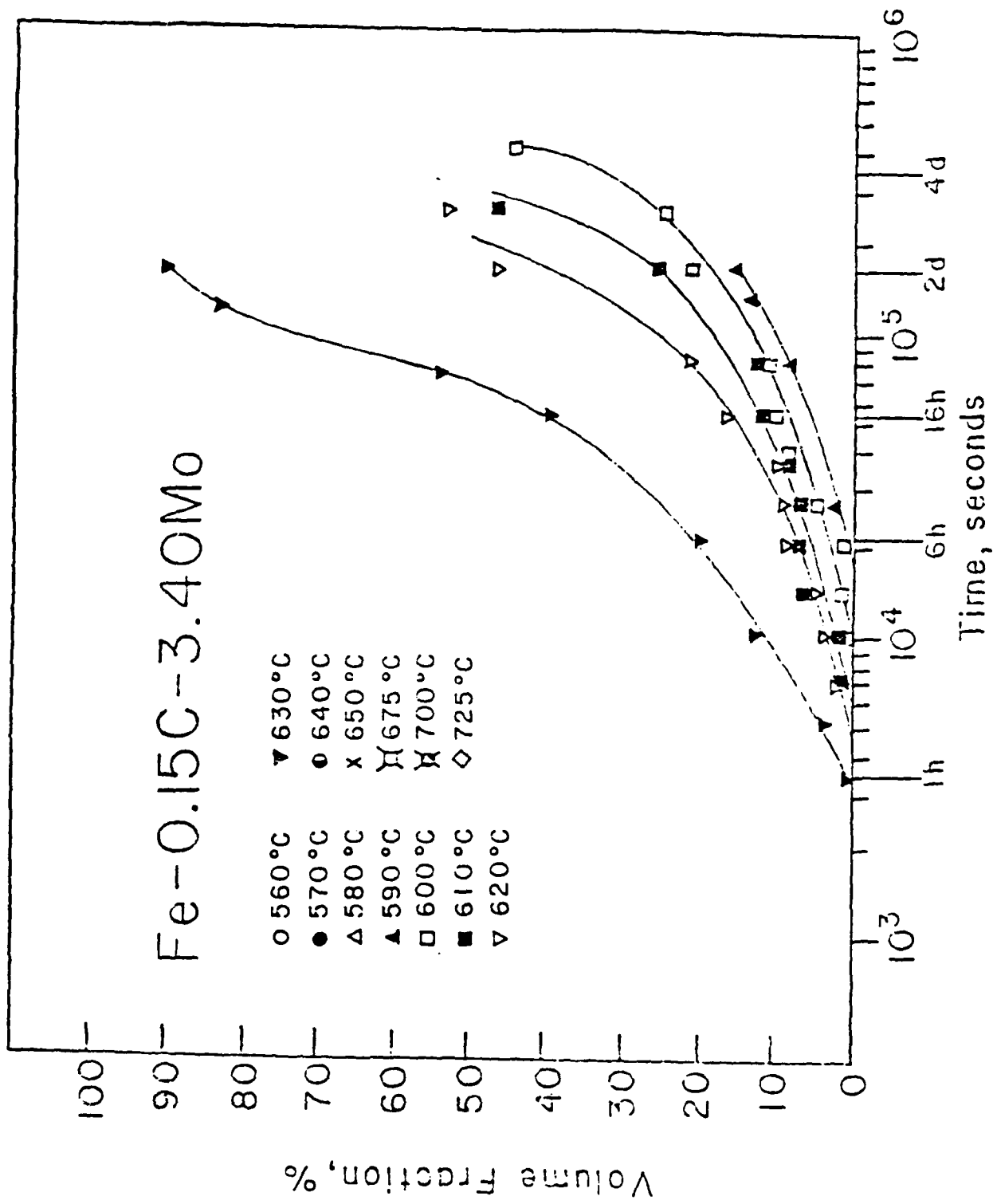


Figure 9

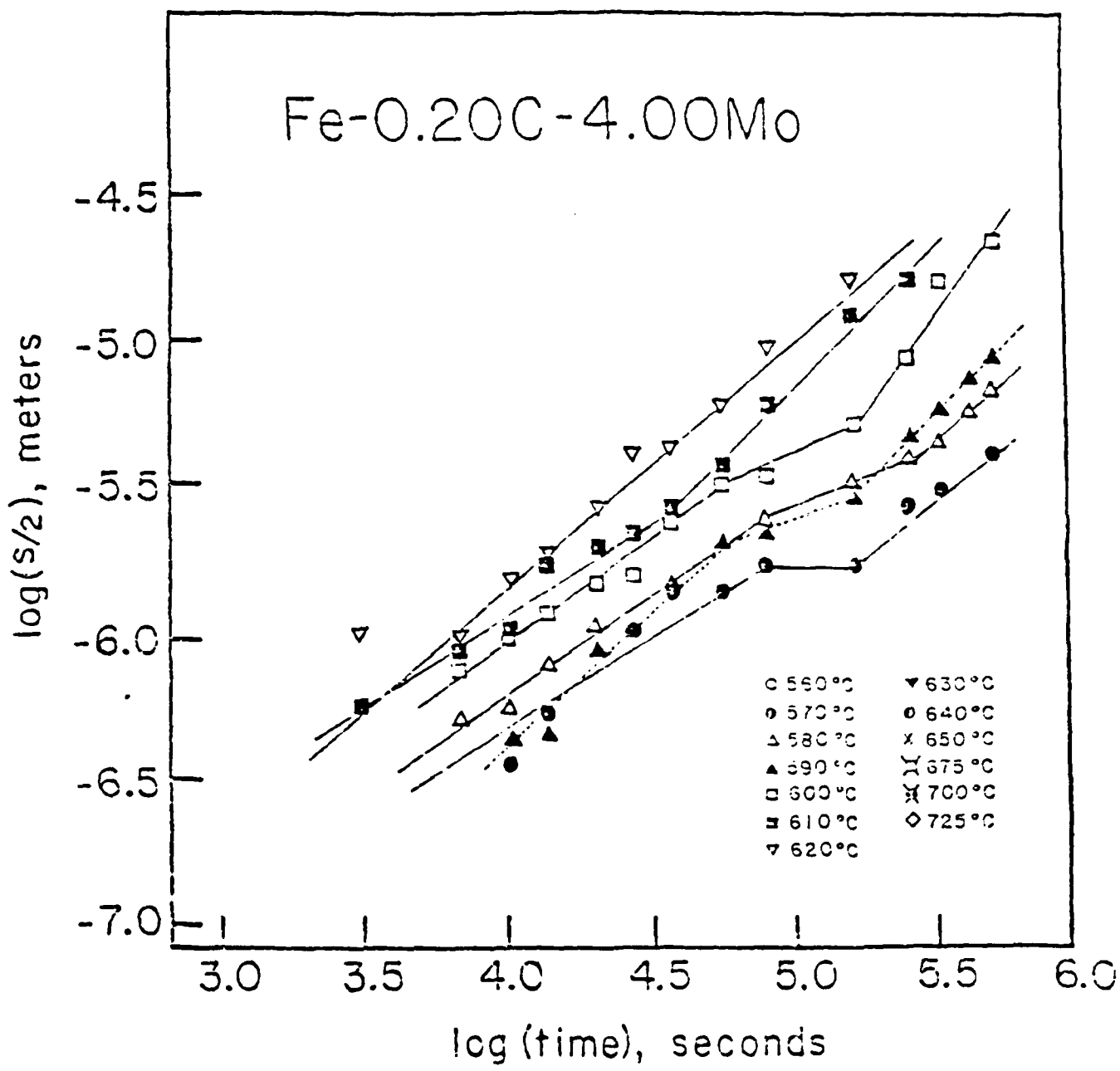
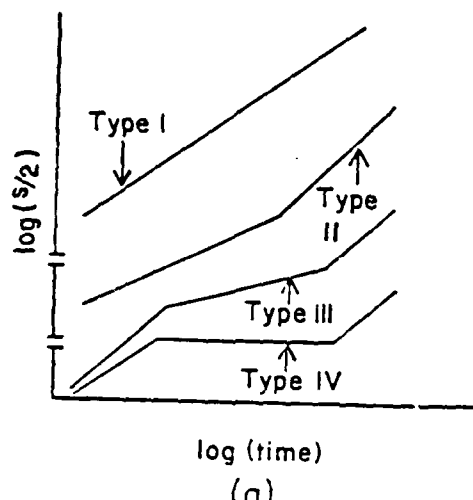
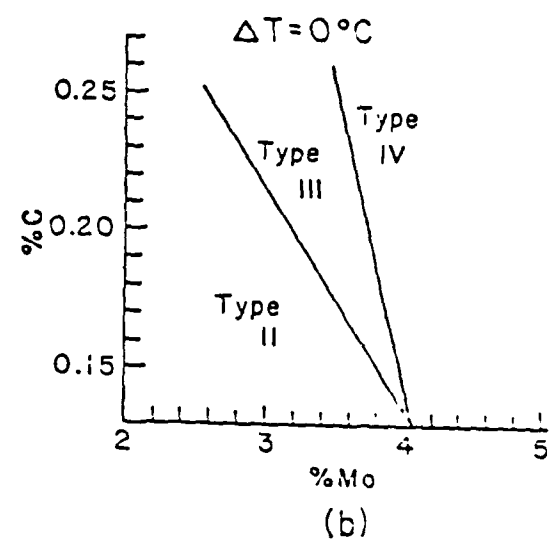


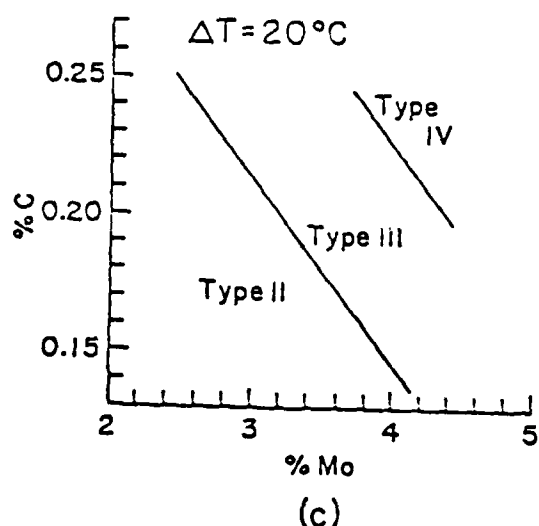
Figure 10



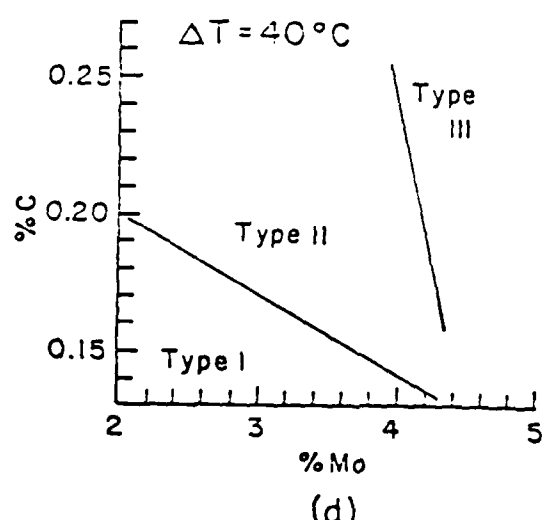
(a)



(b)



(c)



(d)

Figure 11

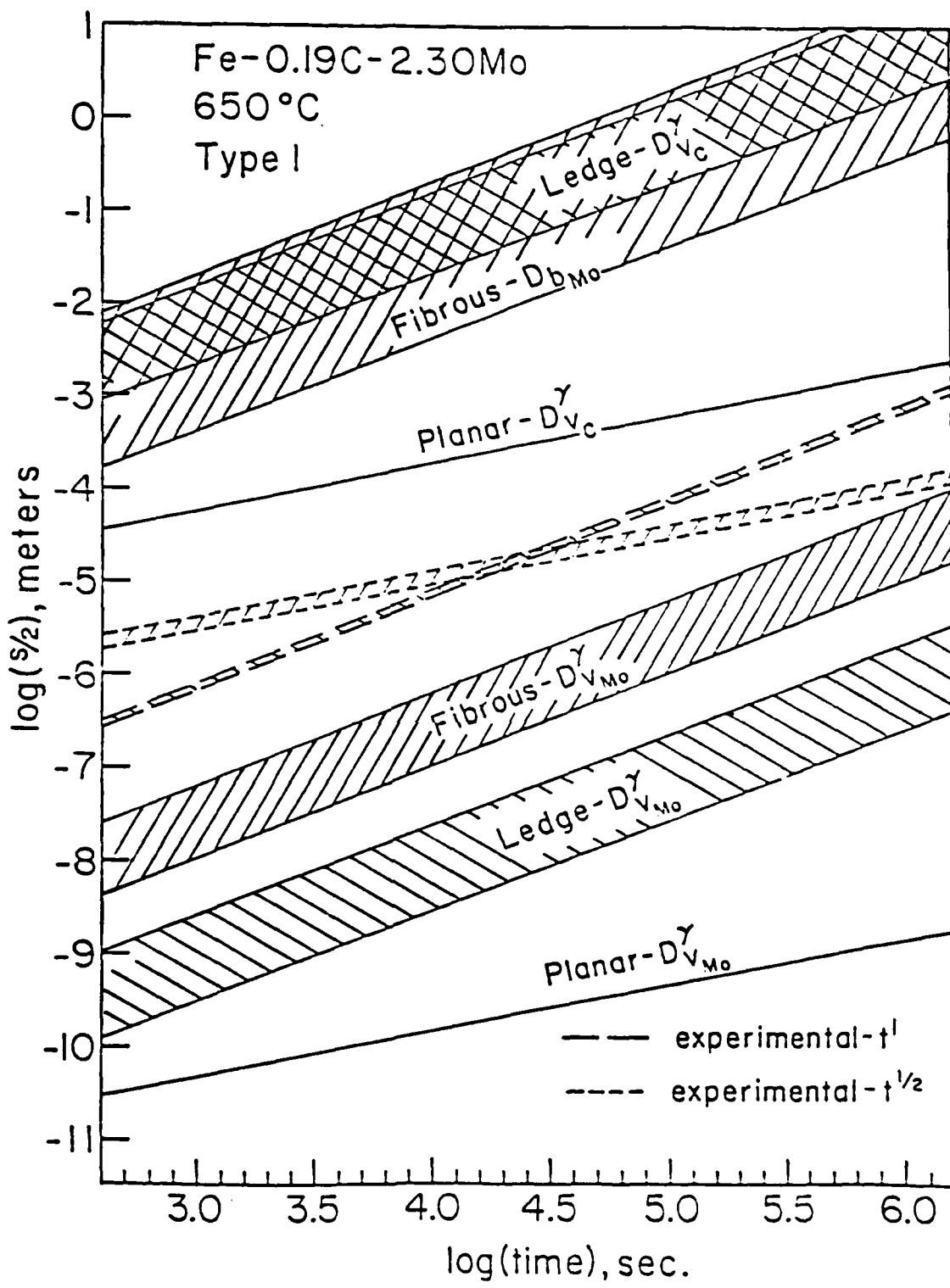


Figure 12a

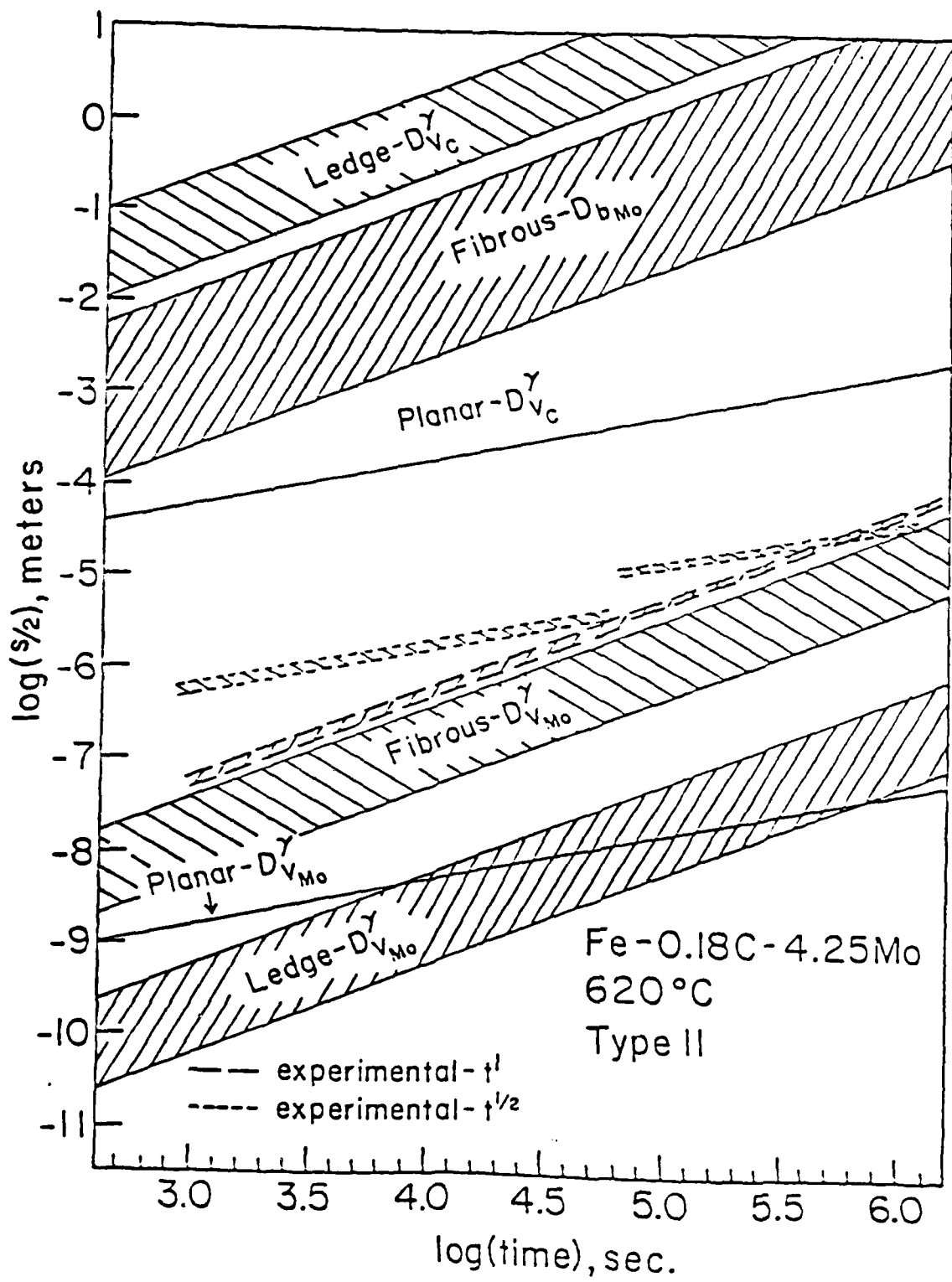


Figure 12b

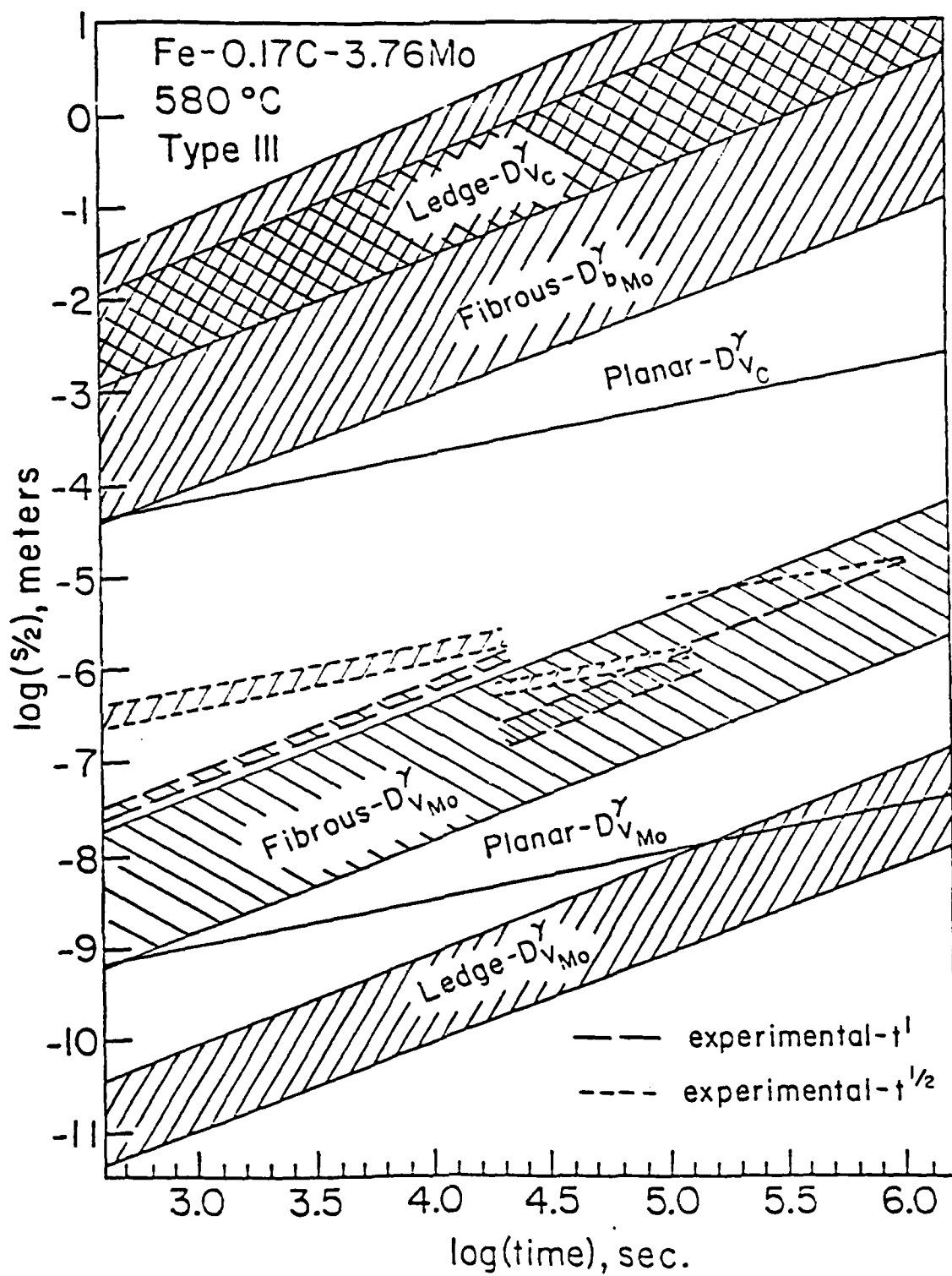


Figure 12c

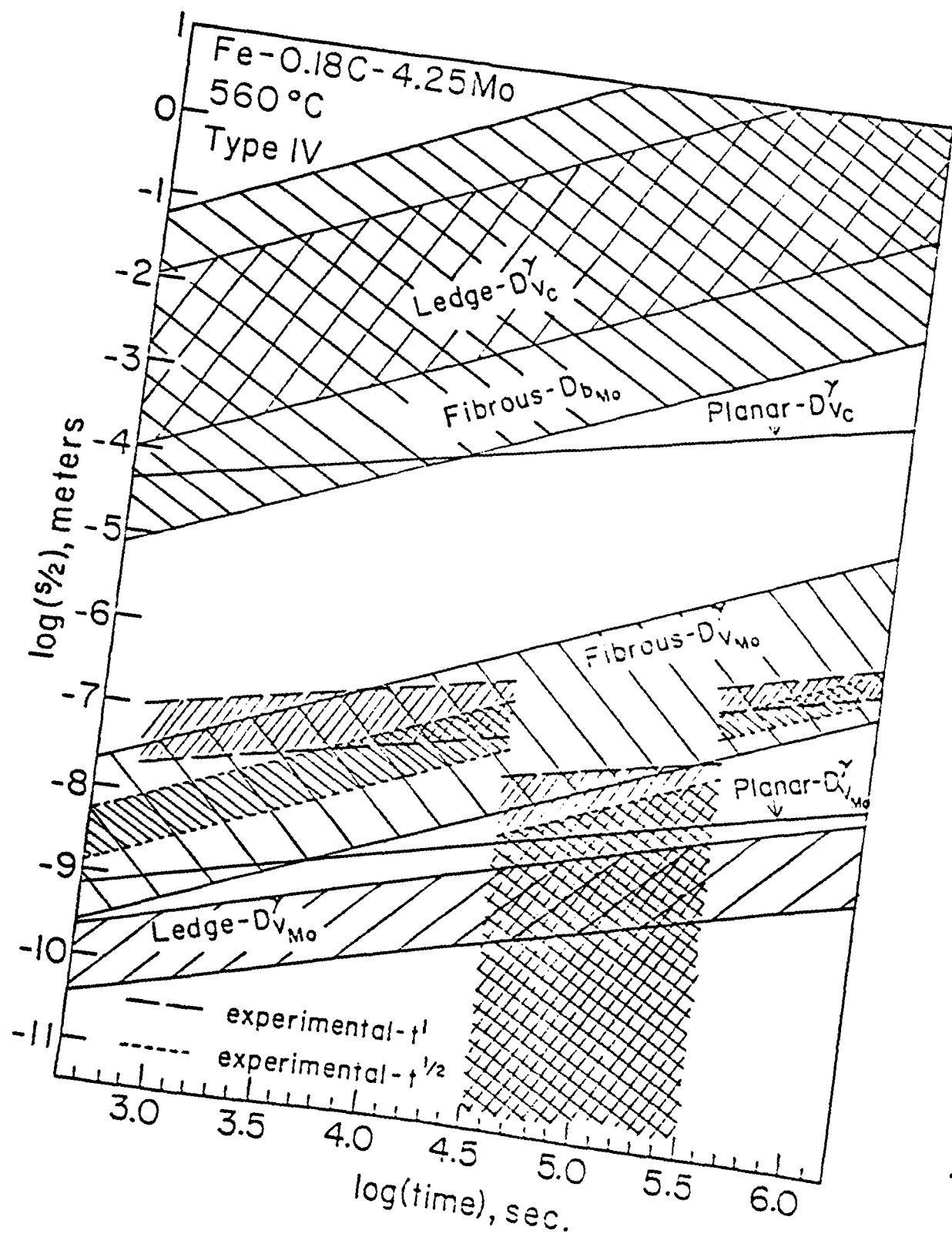


Figure 1-3

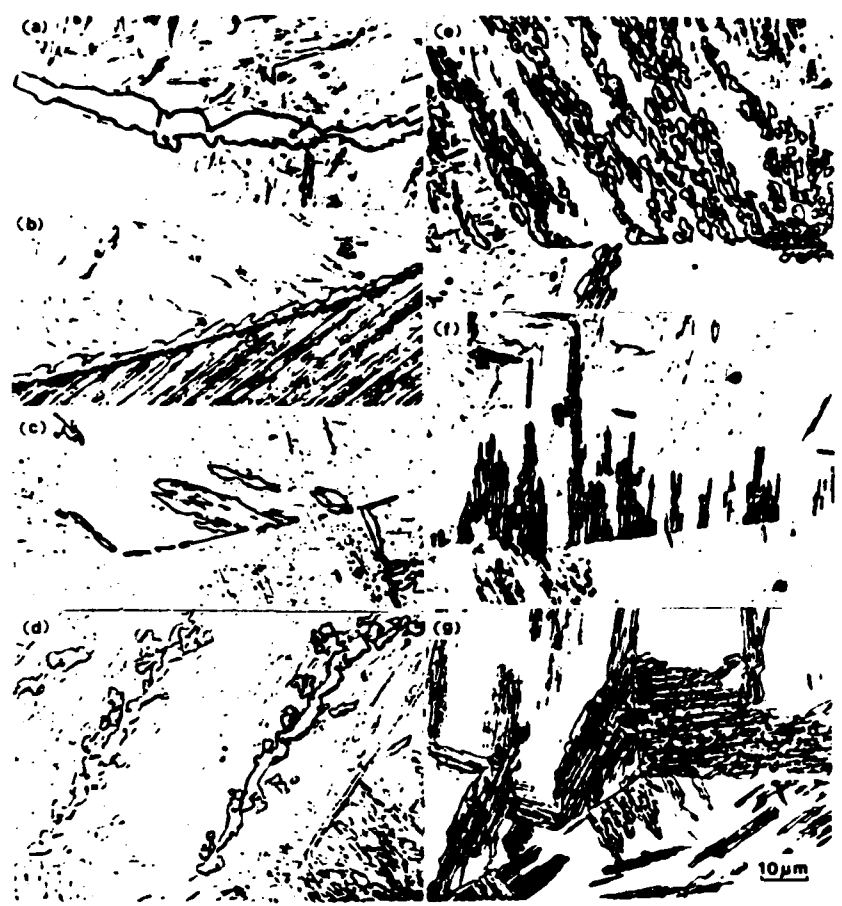


Figure 13



Figure 14



Figure 15

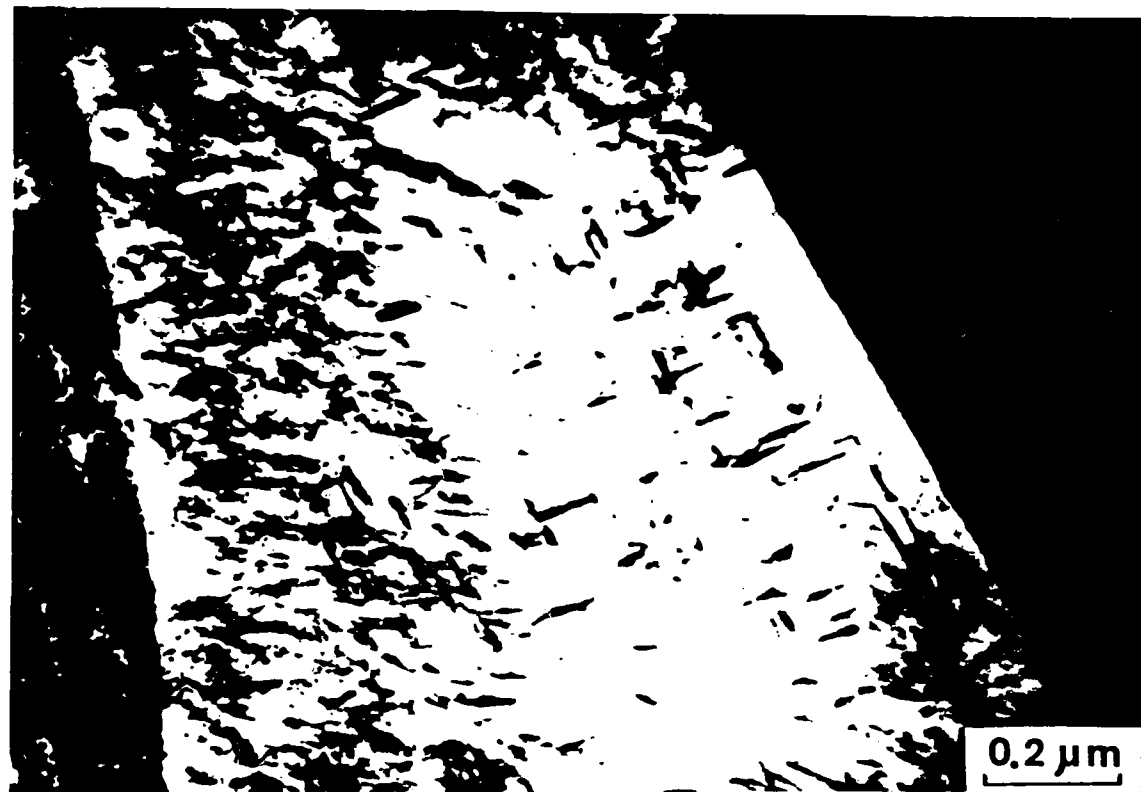


Figure 16

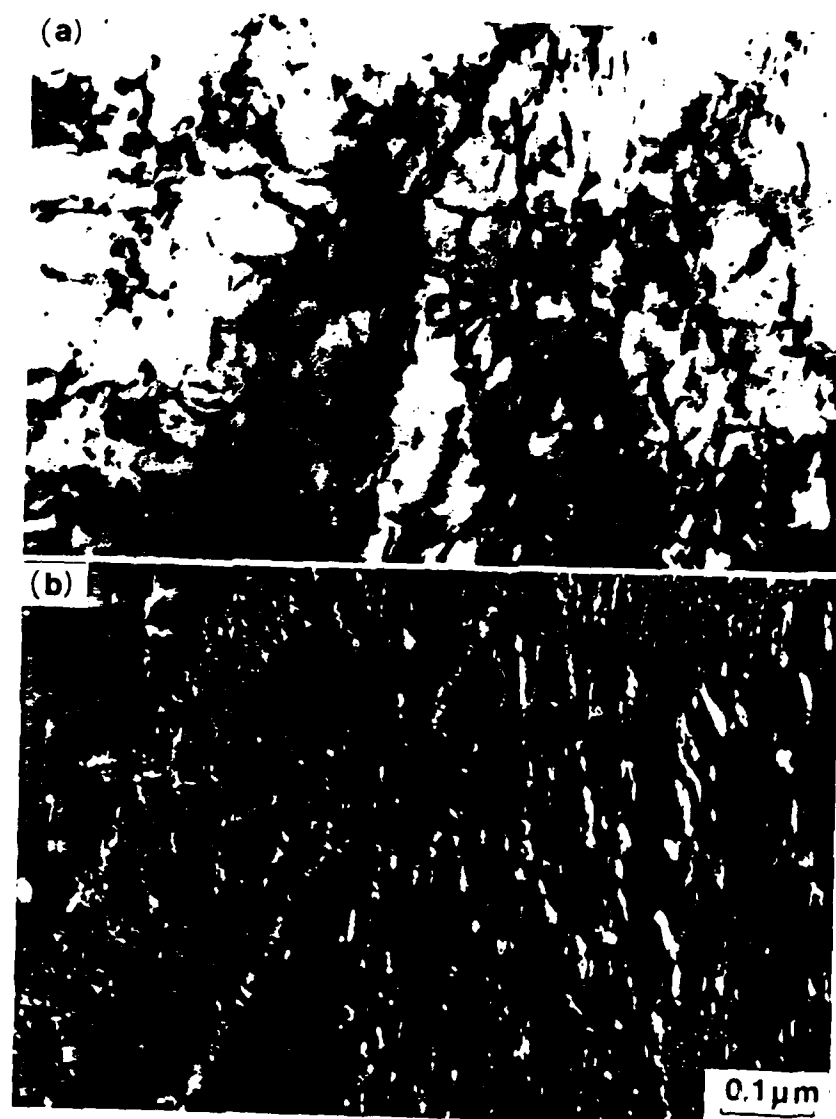


Figure 17

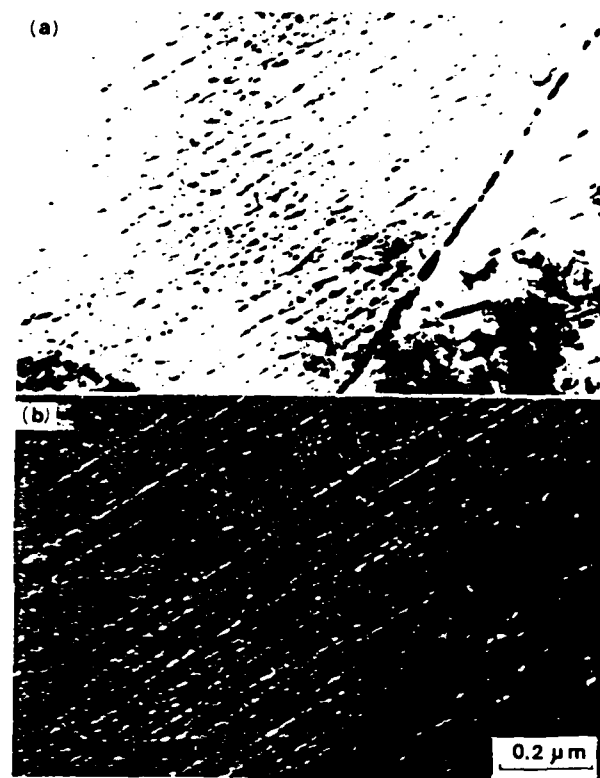


Figure 18

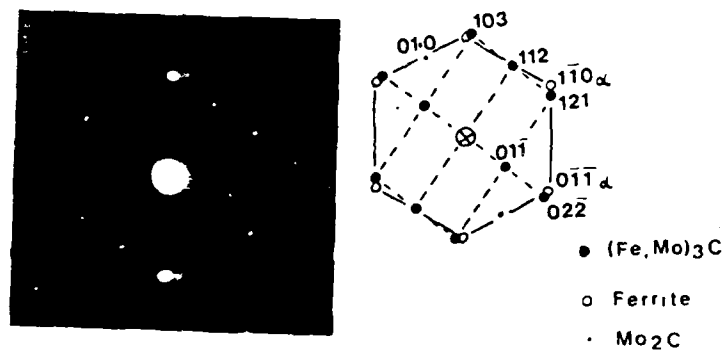


Figure 19

AD-A137 902

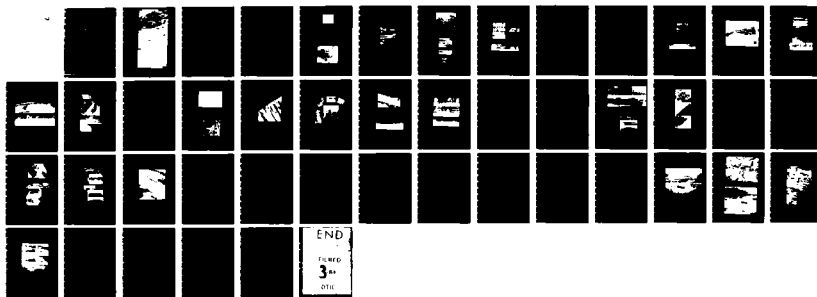
BARRIERS TO THE MIGRATION OF INTERPHASE BOUNDARIES(U)
CARNEGIE-MELLON UNIV PITTSBURGH PA H I AARONSON ET AL.
06 JAN 84 ARO-17094. 1-MS DAAG29-80-C-0018

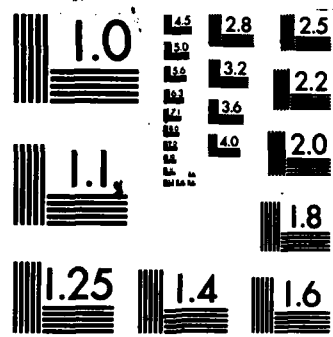
2/2

UNCLASSIFIED

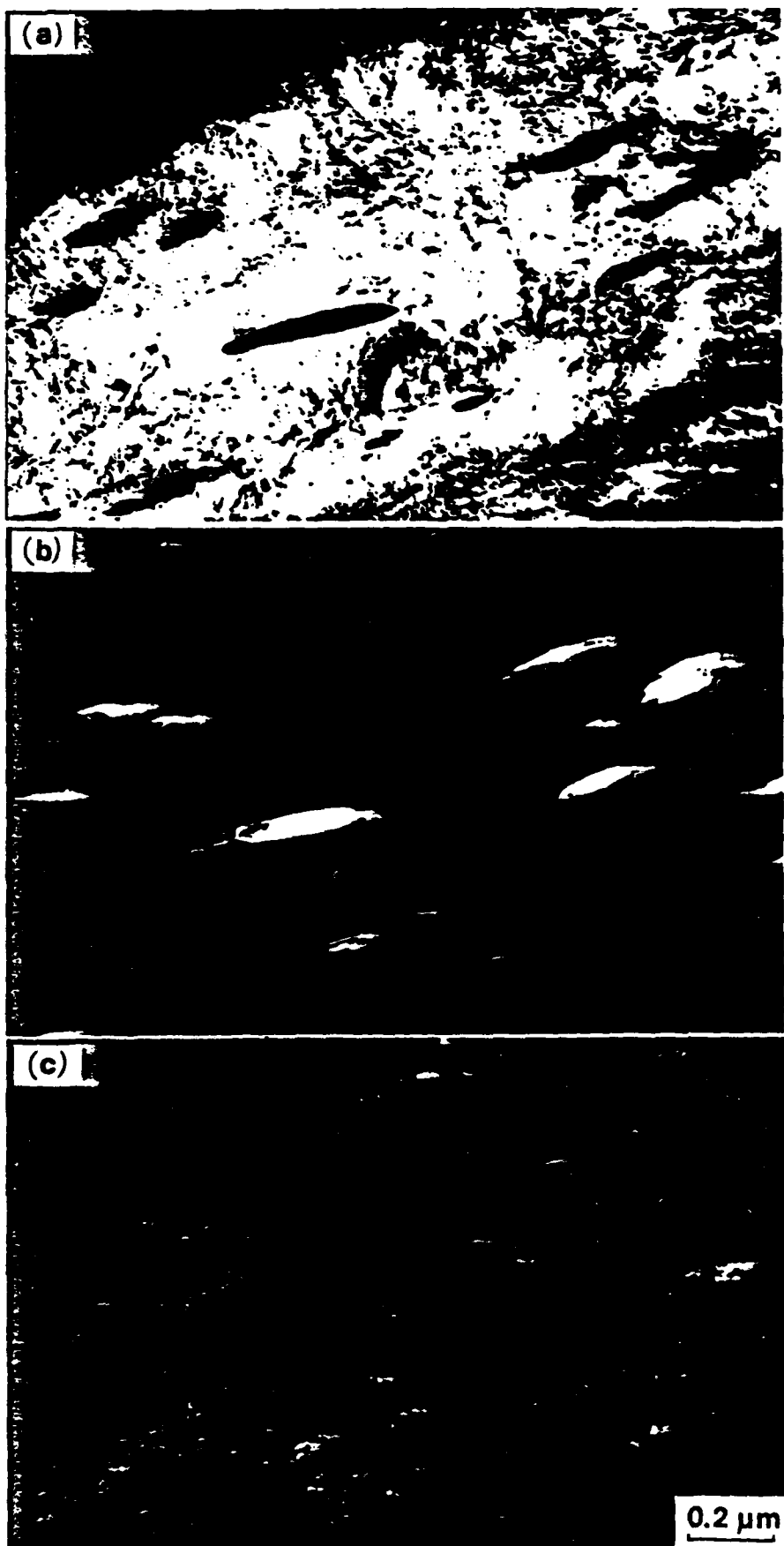
F/G 11/6

NL





MICROCOPY RESOLUTION TEST CHART
NATIONAL BUREAU OF STANDARDS-1963-A



$0.2 \mu\text{m}$

Figure 20

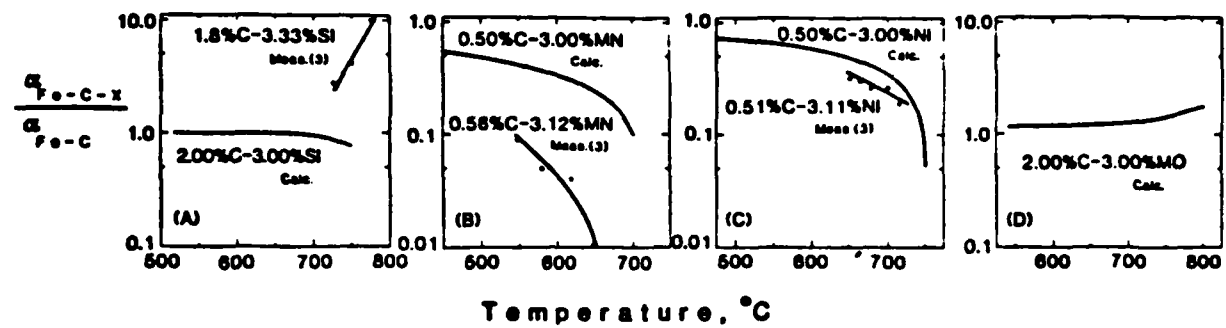


Figure 21

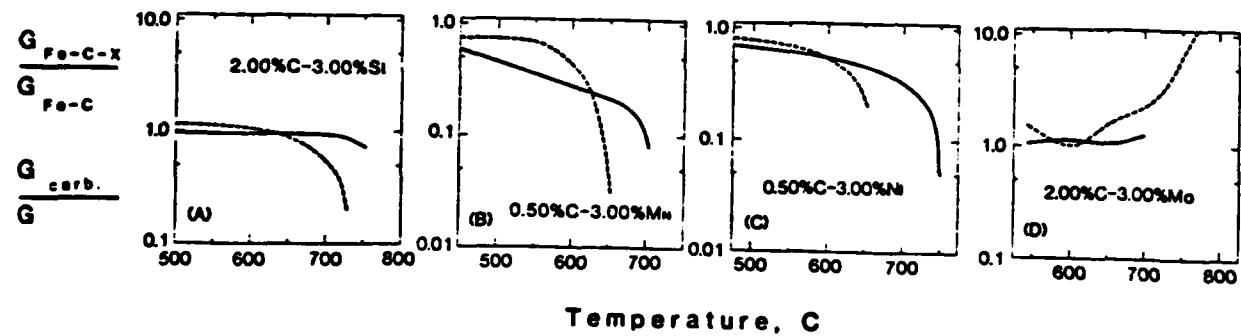


Figure 22

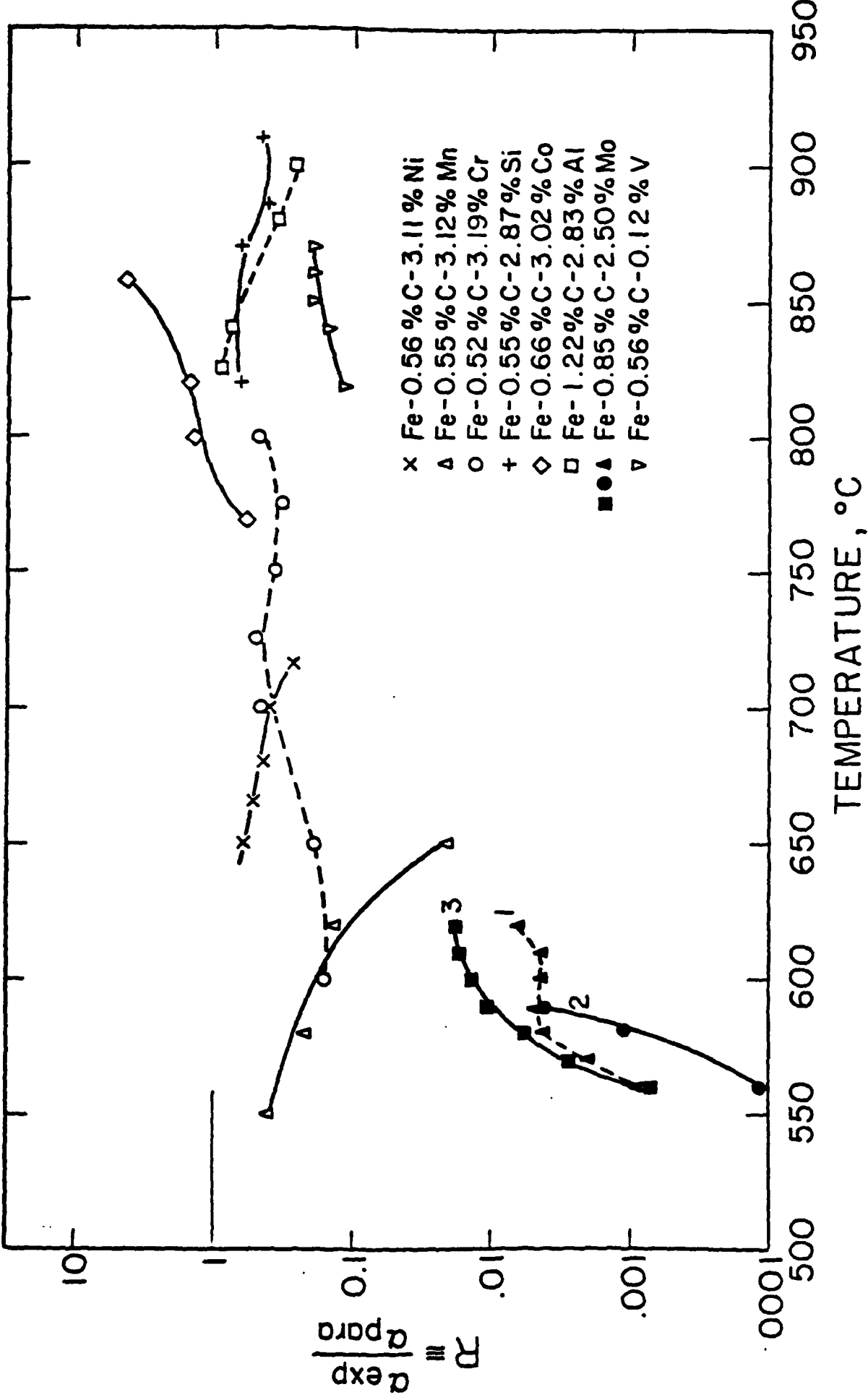
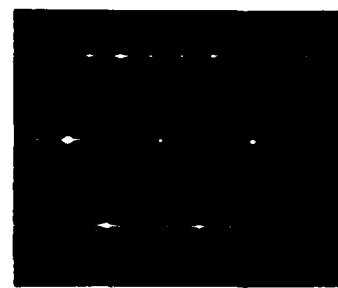


Figure 23



241 244 247
• • • • K=4

122 125 128
• • • • K=2

000 003 006 009
• • • •

Figure 24



Figure 25

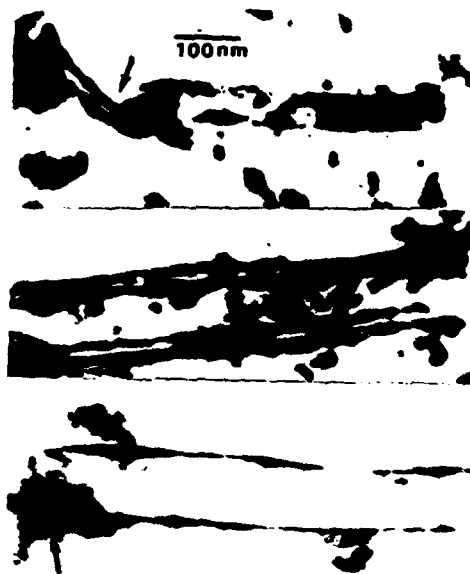


Figure 26



Figure 27

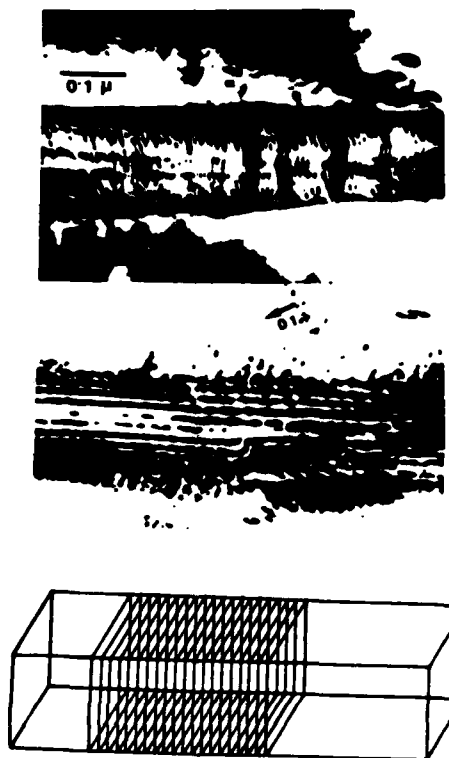


Figure 28

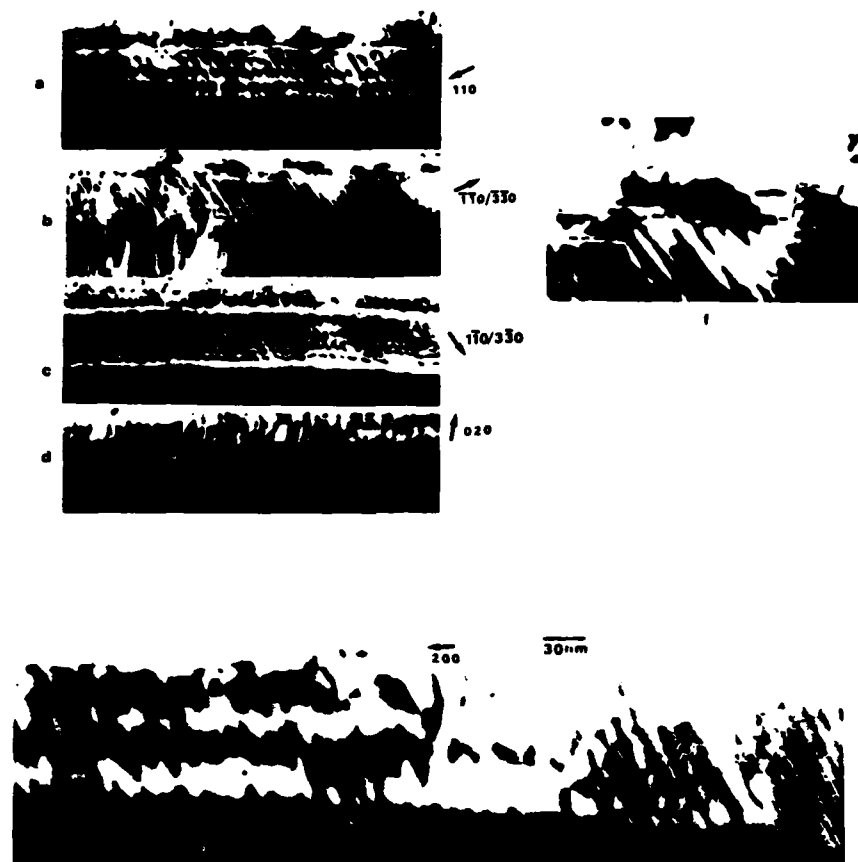


Figure 29

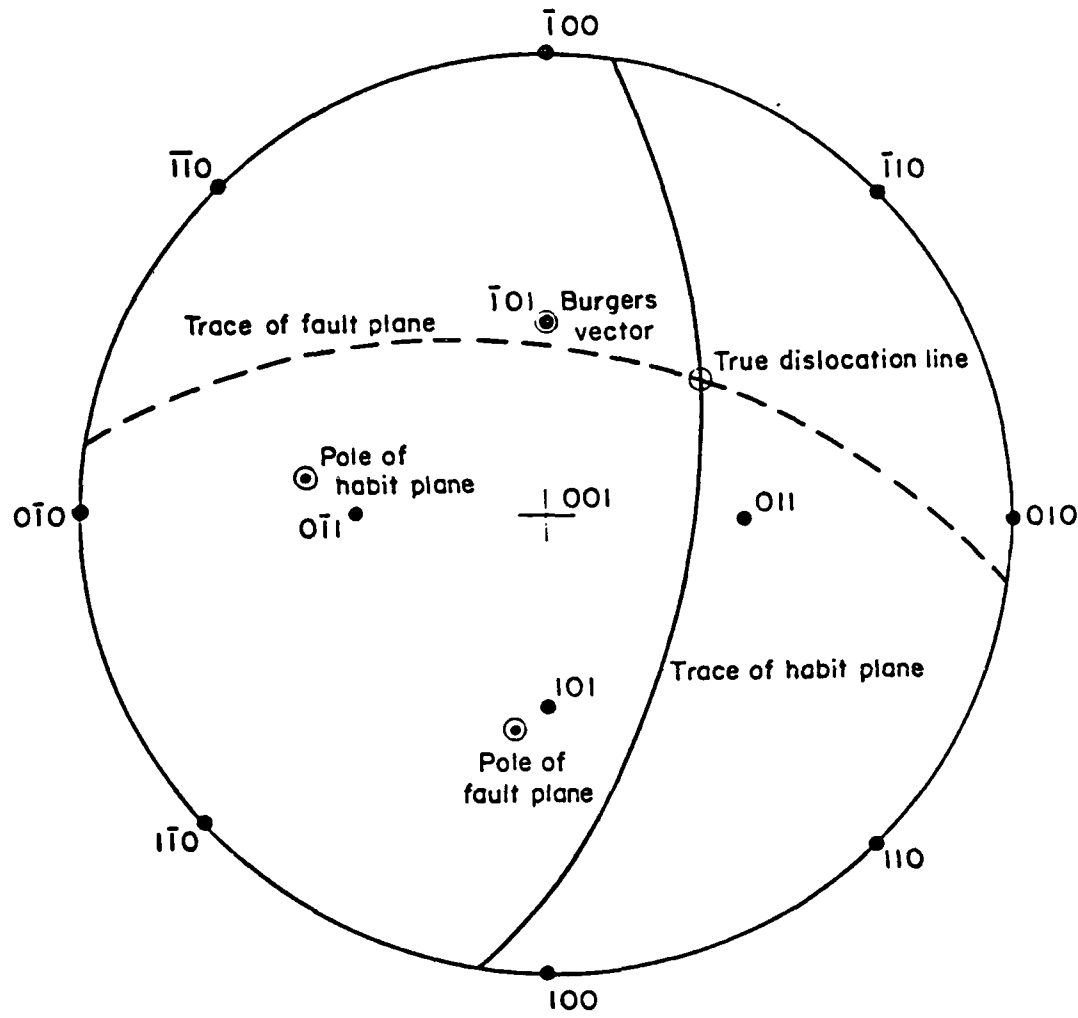


Figure 29 con't.

g	extinction condition
110	N
$\bar{1}10$	N
200	N
020	Y
$1\bar{2}1$	Y
$12\bar{1}$	N

Figure 29 con't.

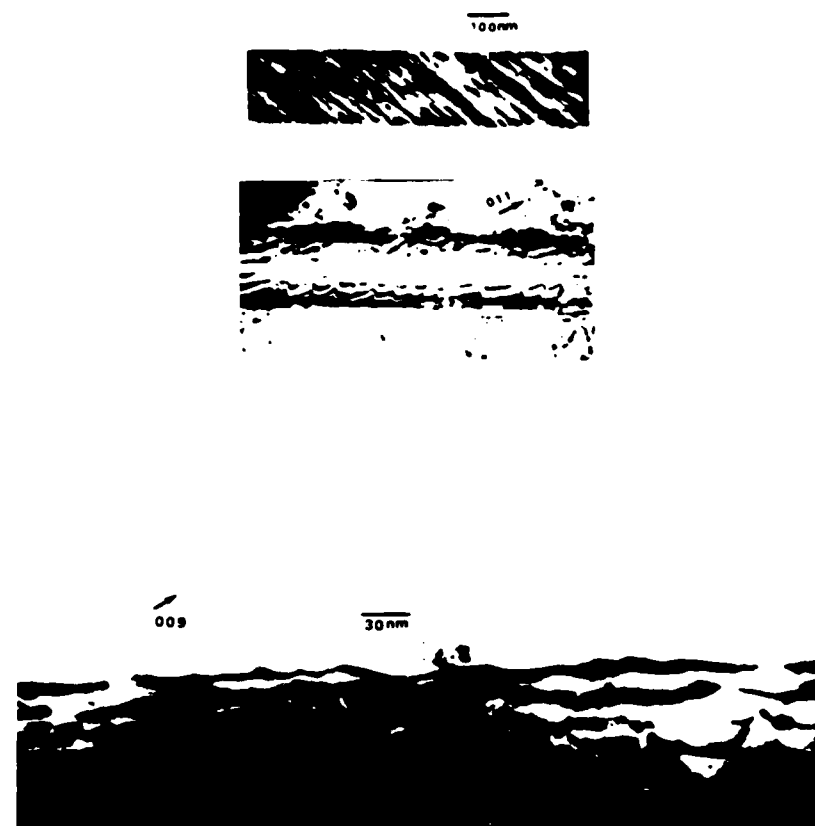


Figure 30

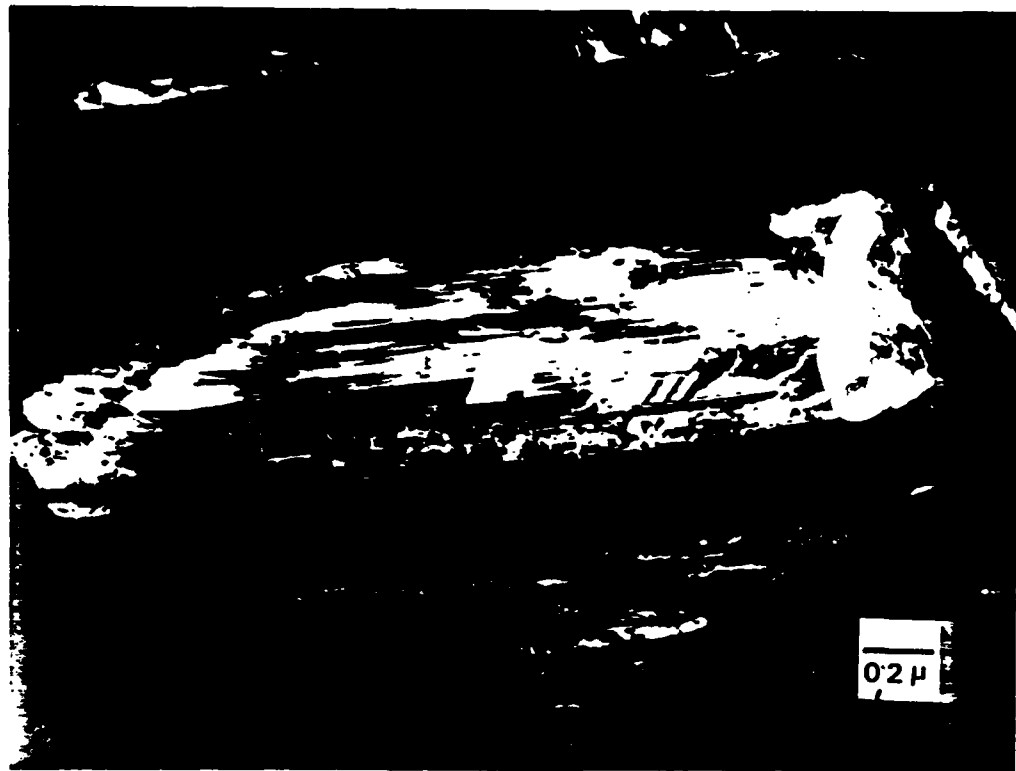


Figure 31

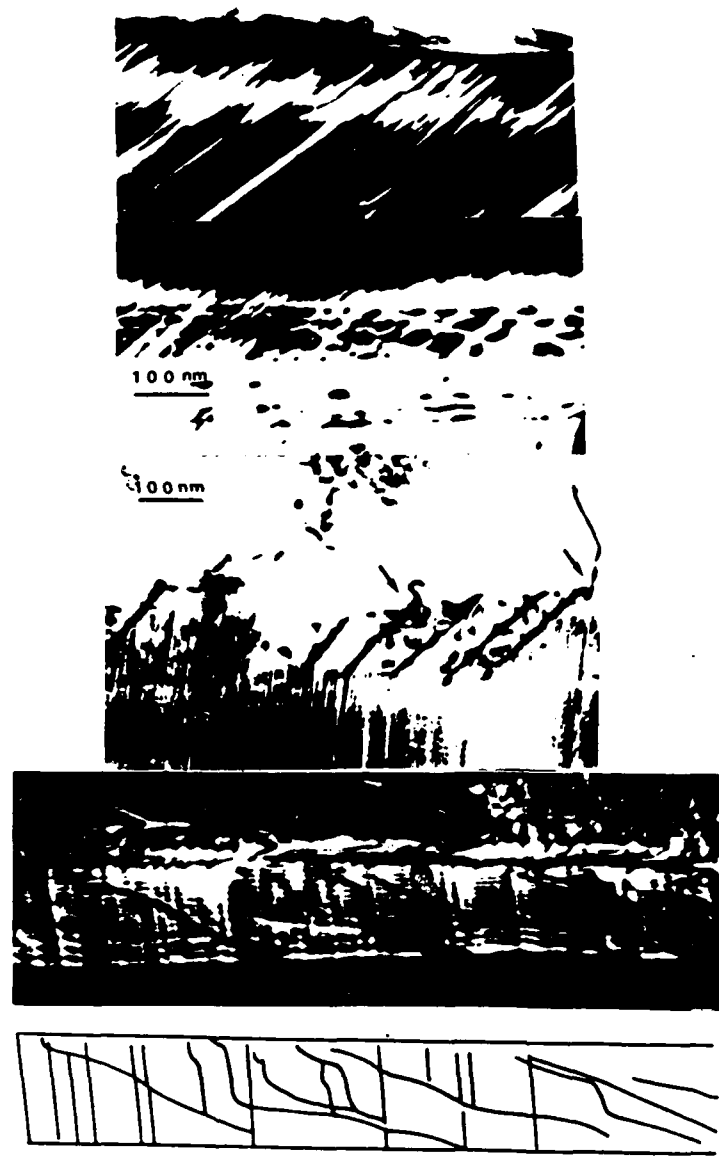


Figure 33



Figure 34

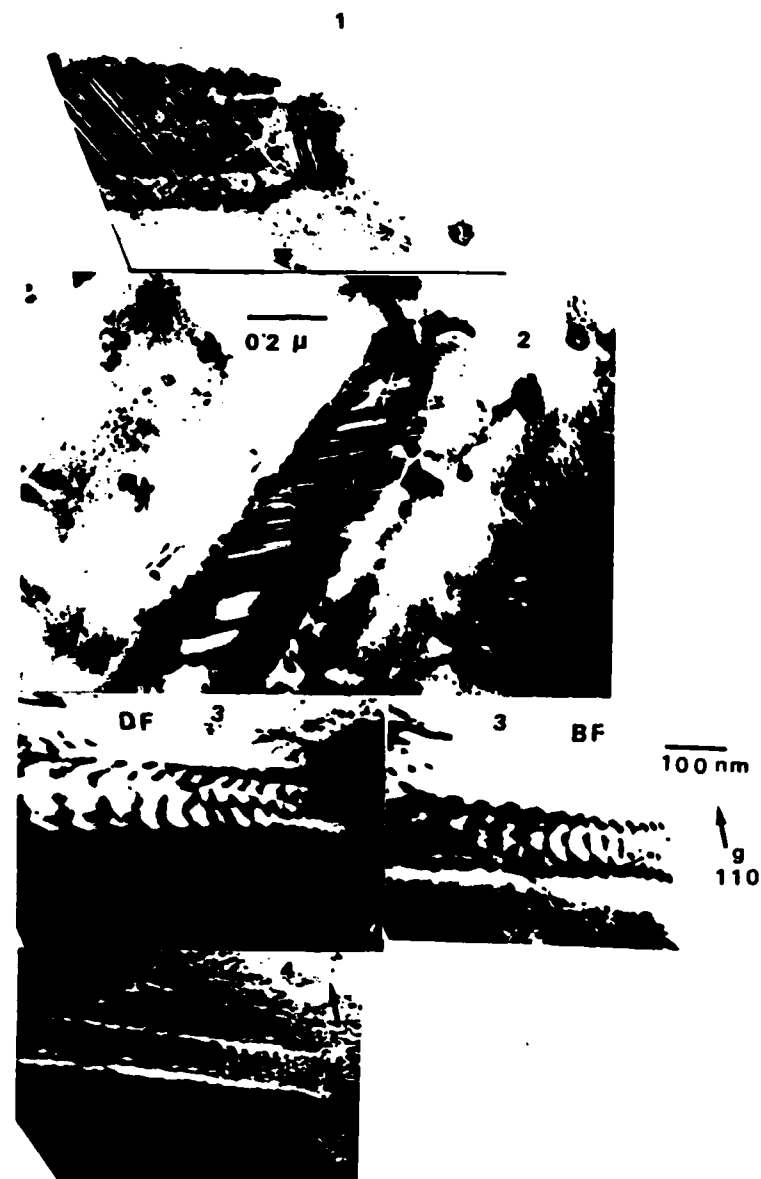


Figure 35

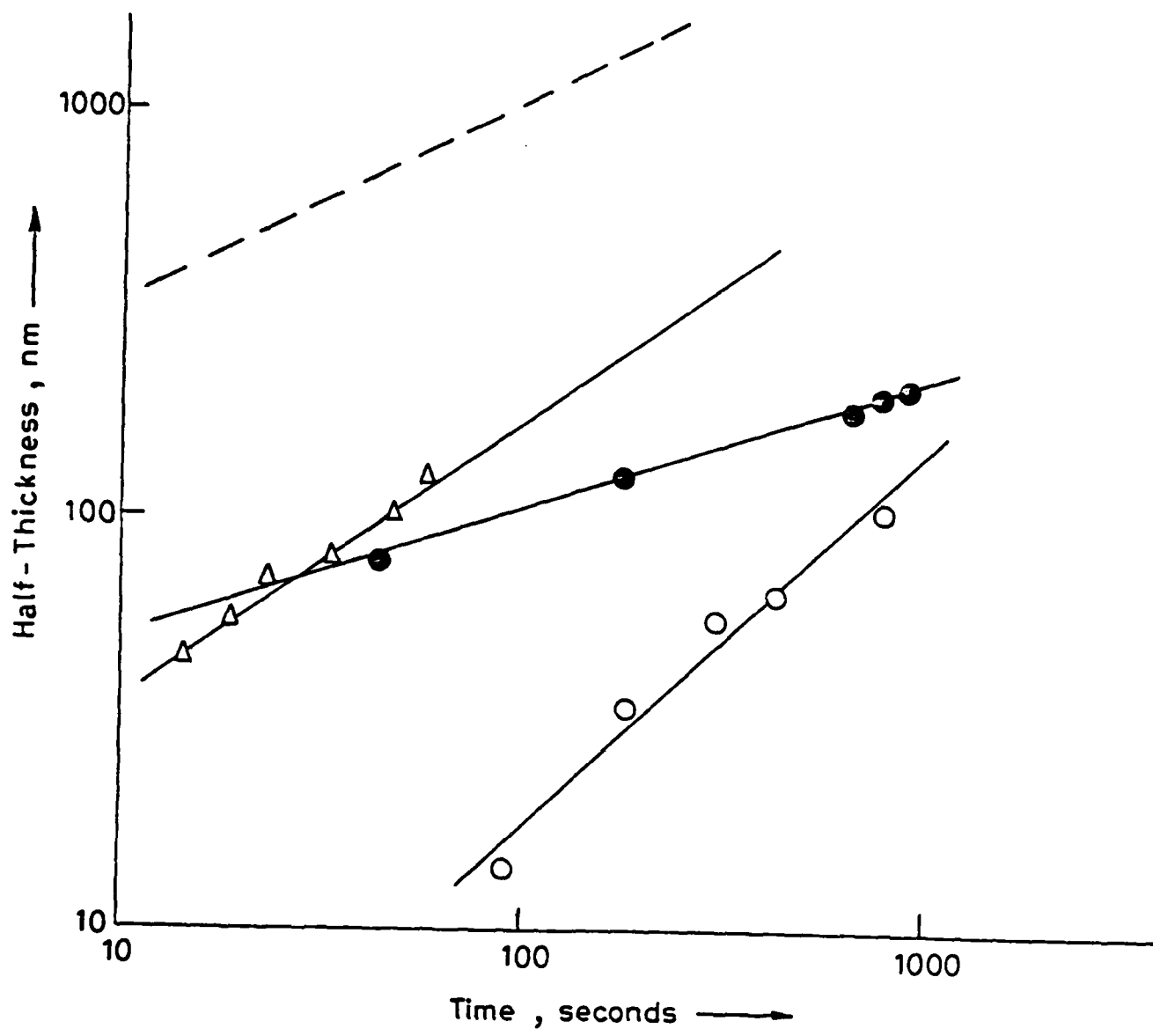


Figure 36

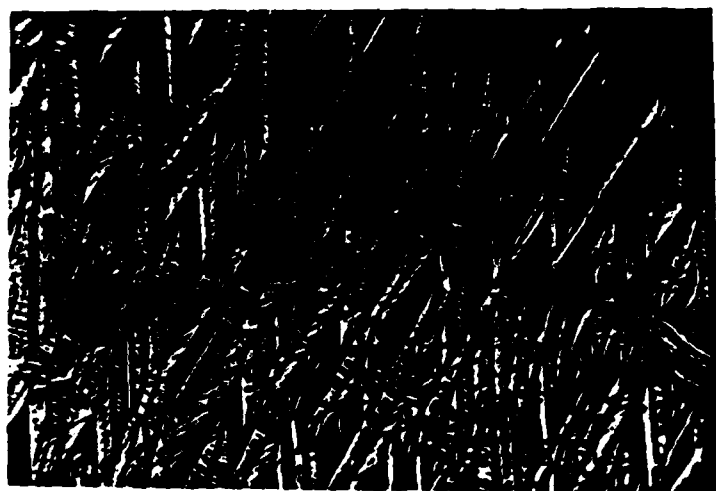


Figure 37



Figure 38

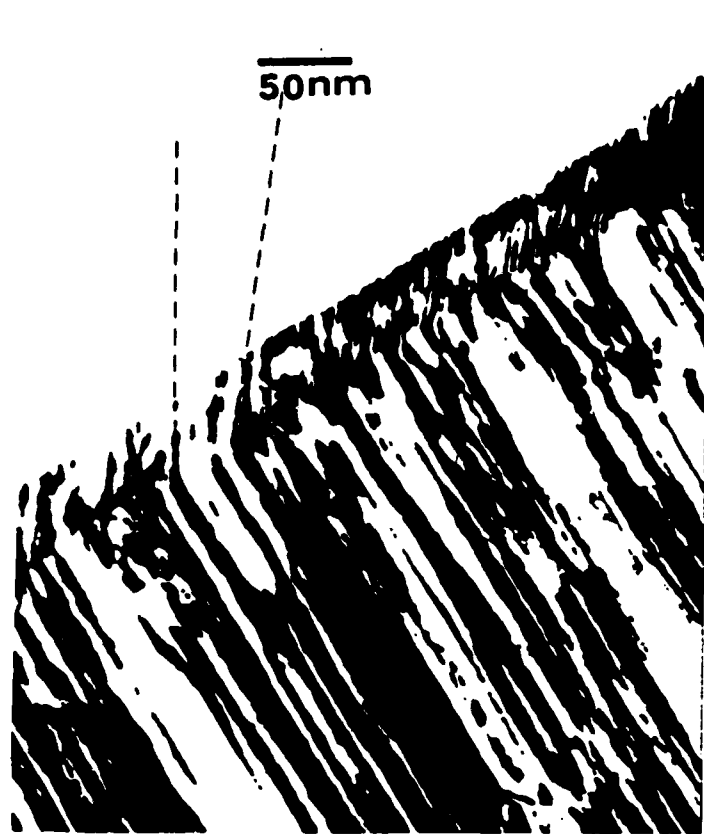


Figure 39

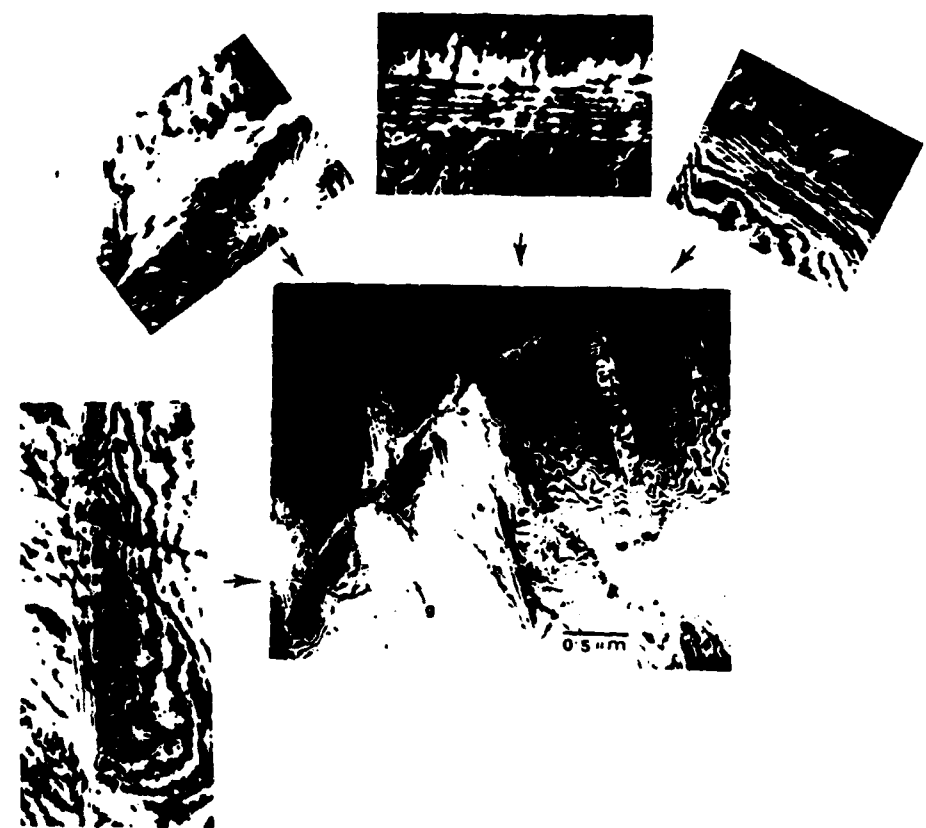


Figure 40

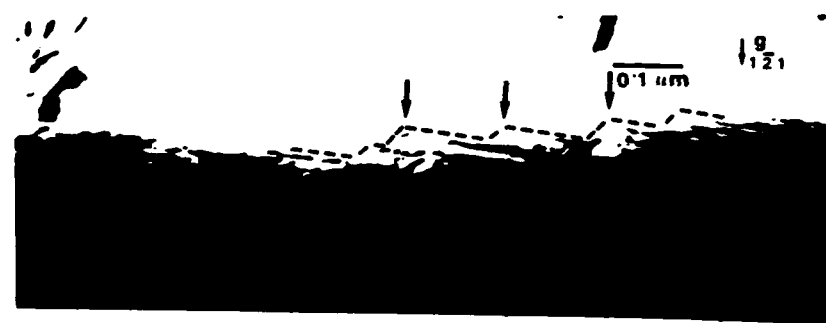
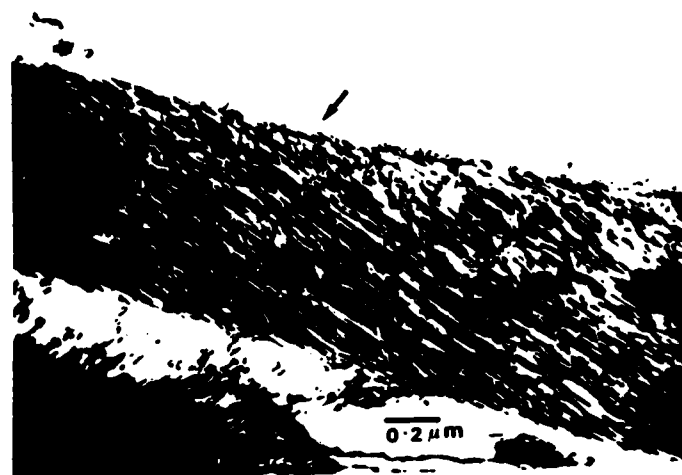


Figure 41

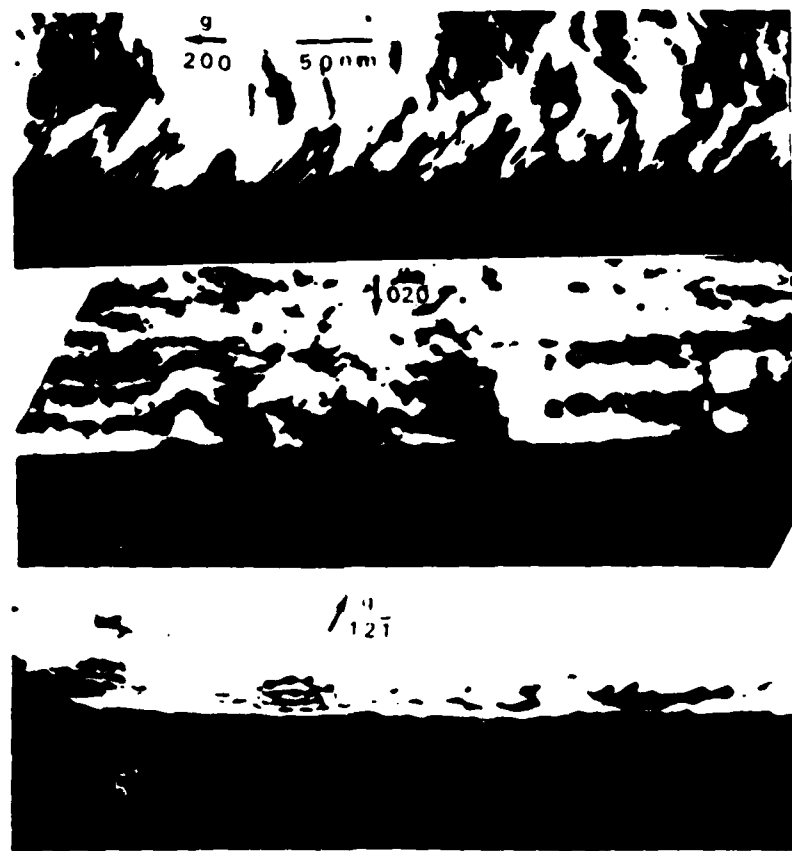


Figure 42

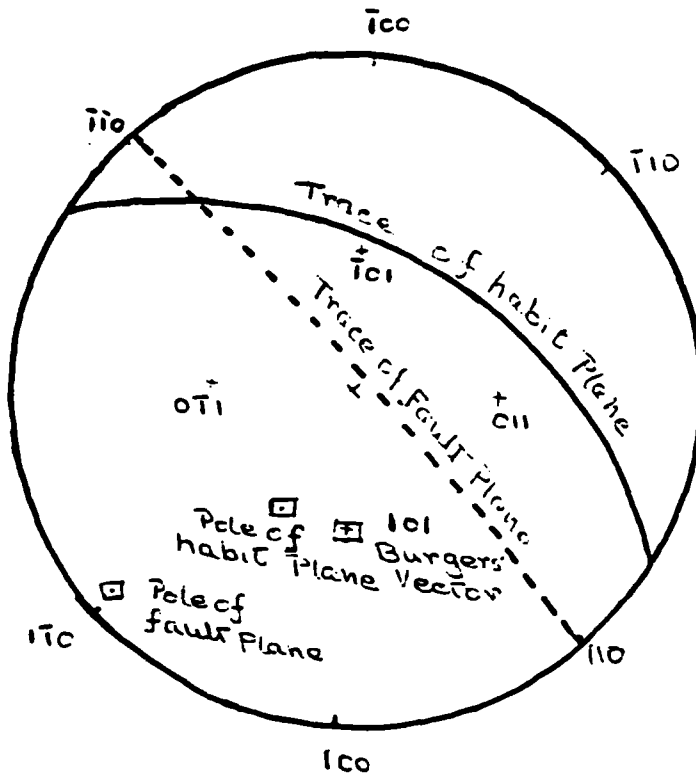


Figure 43

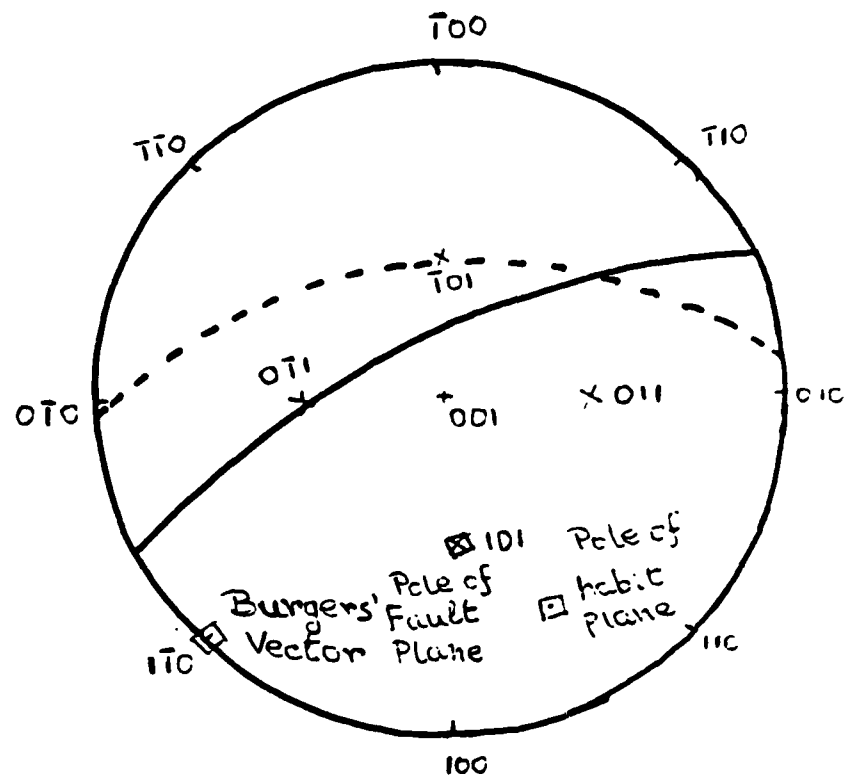


Figure 44

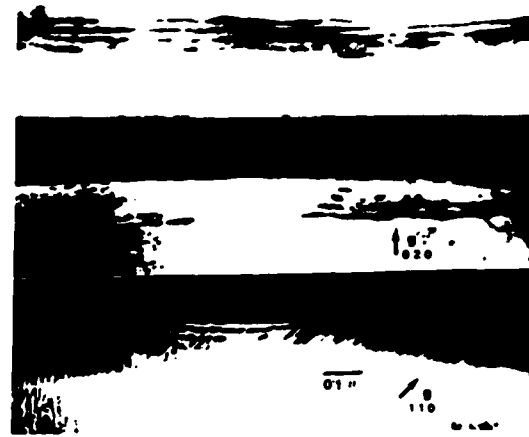
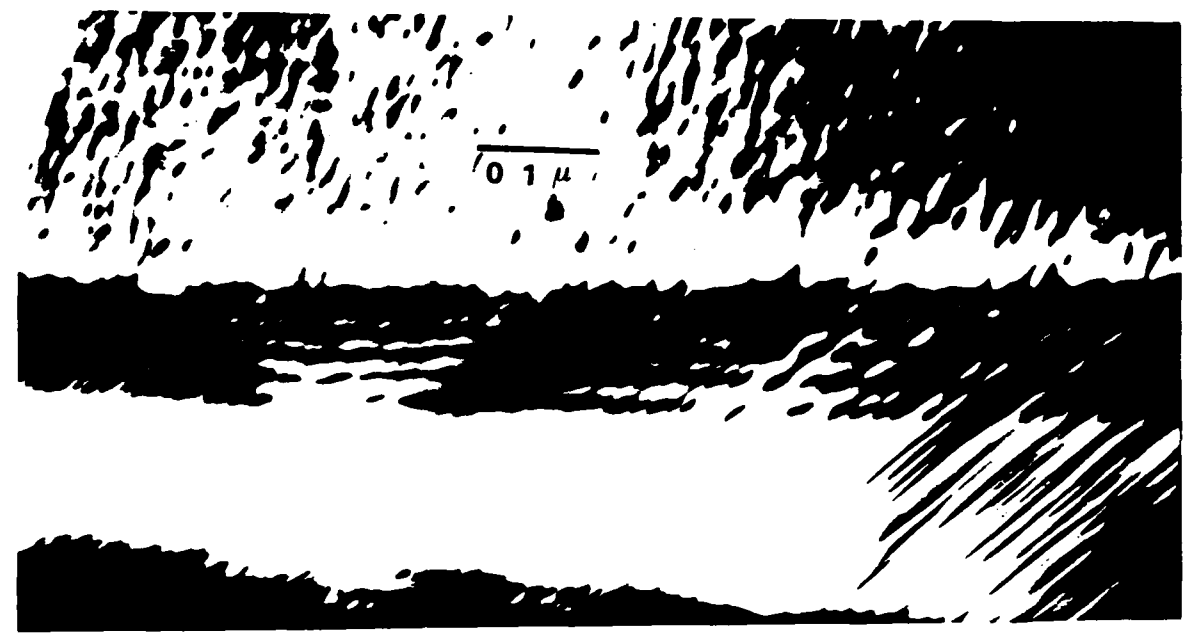


Figure 45



Figure 46

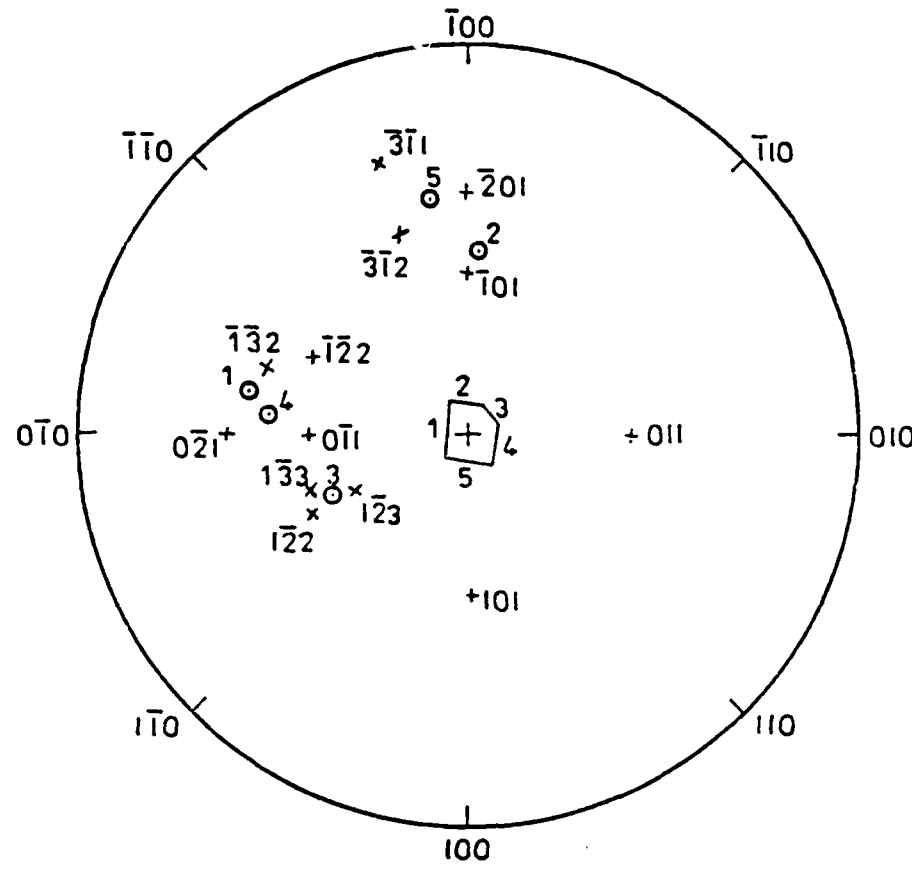


Figure 47

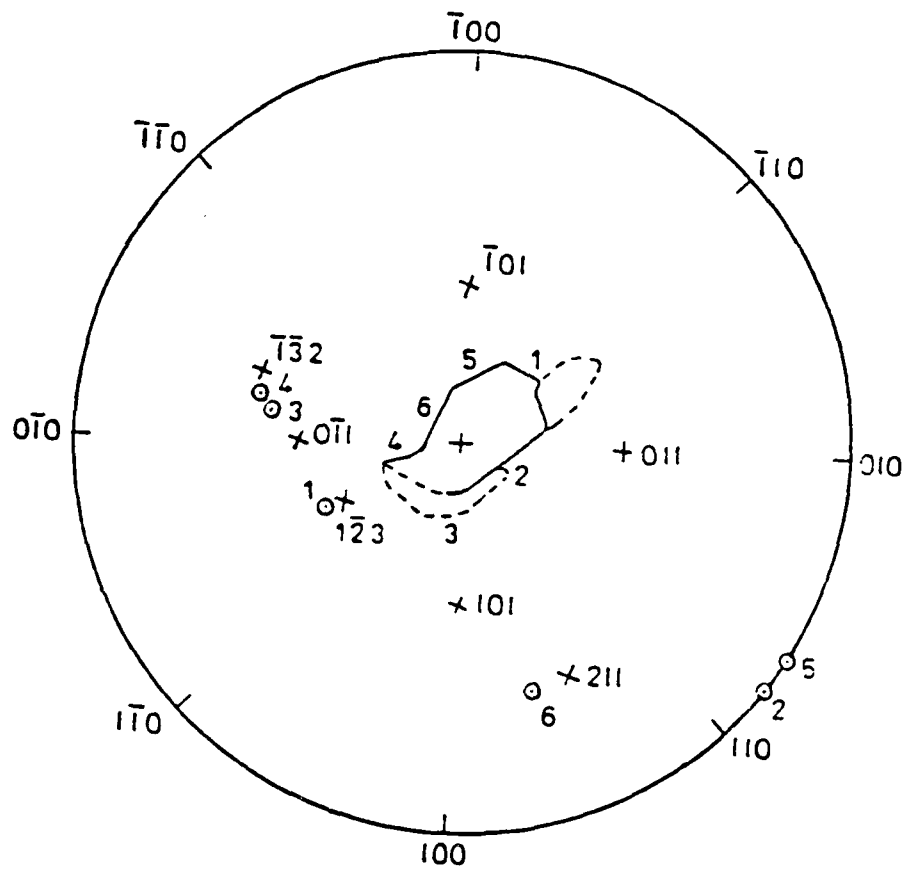


Figure 48

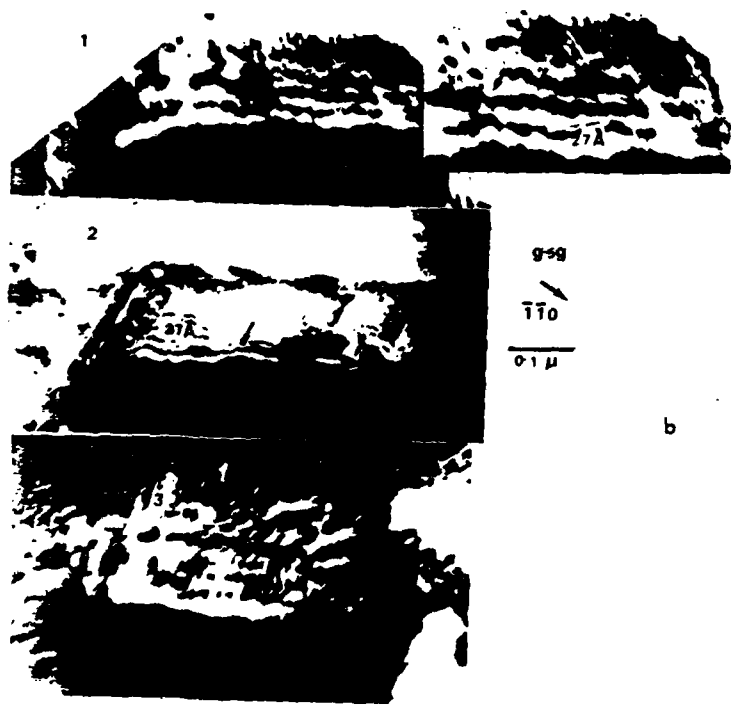


Figure 49

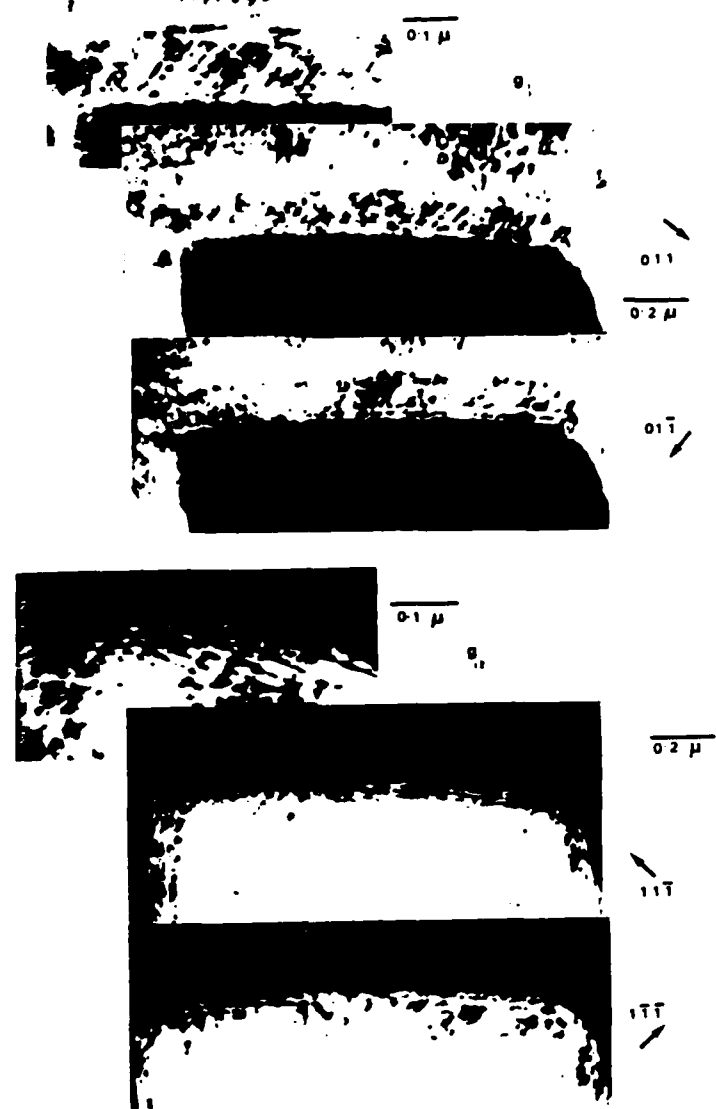


Figure 50

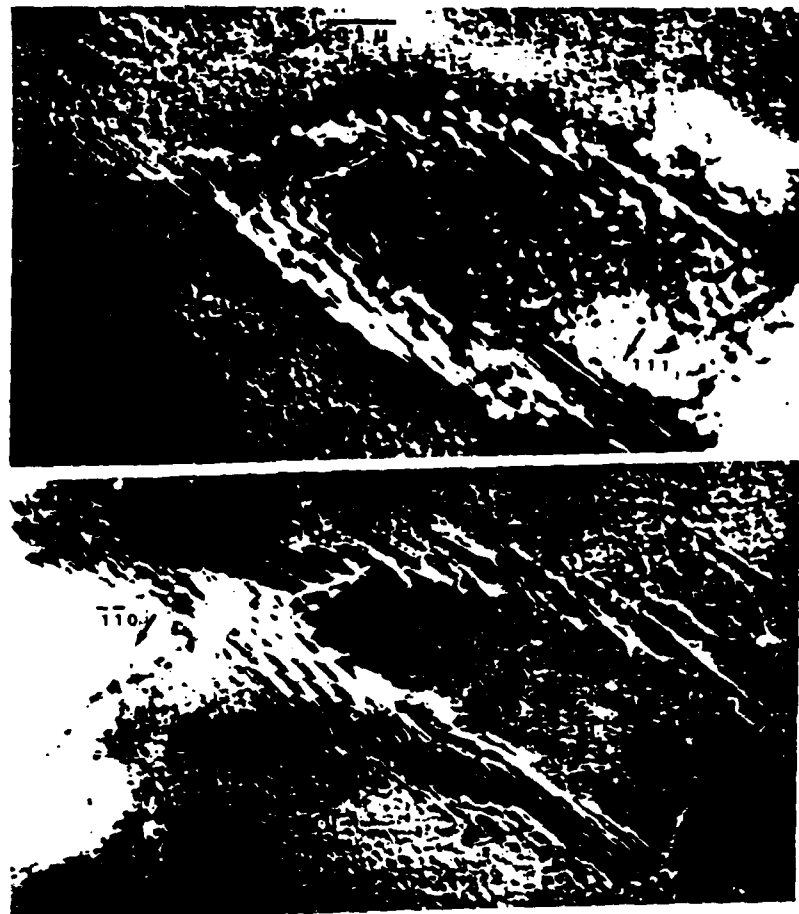


Figure 51

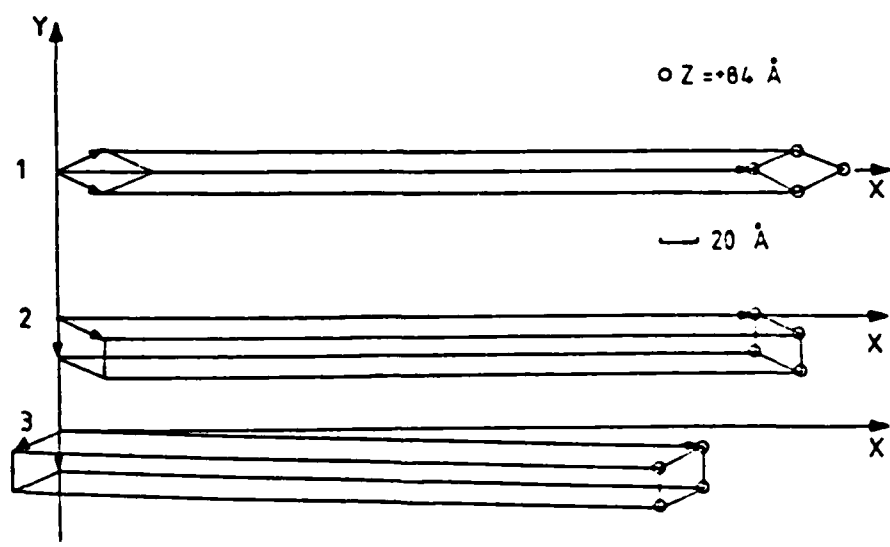


Figure 52

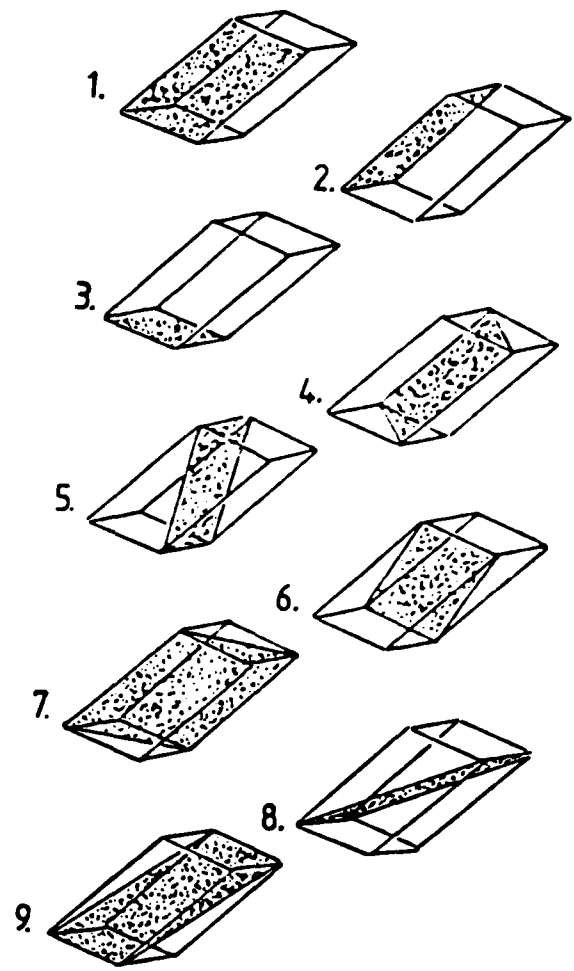
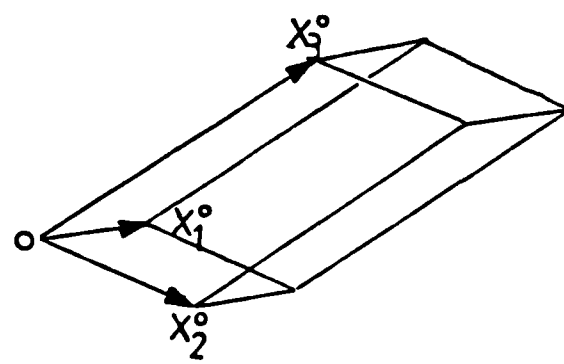


Figure 53

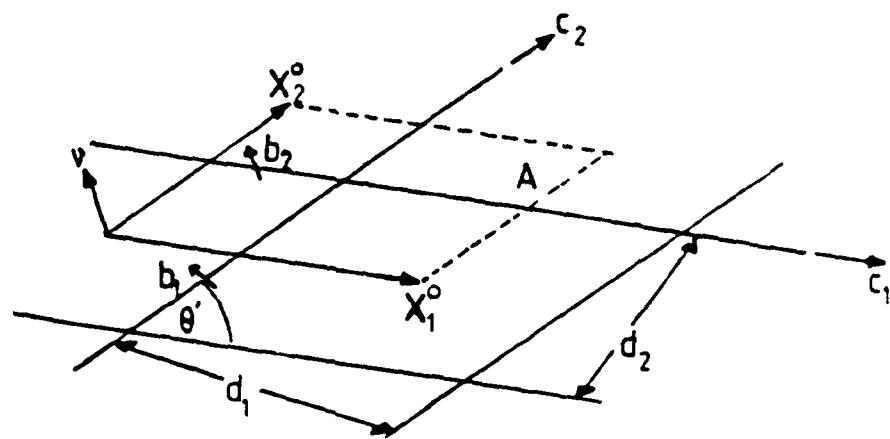


Figure 54

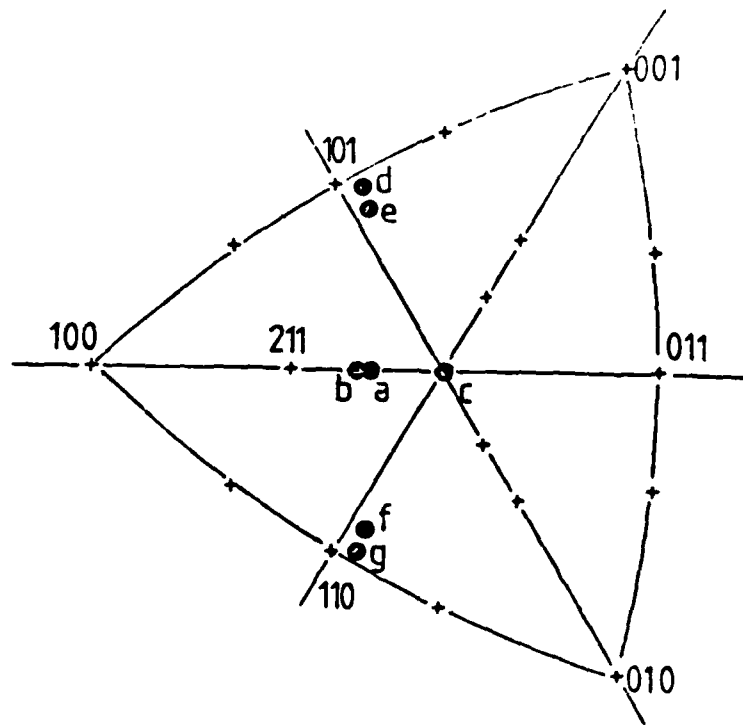


Figure 55

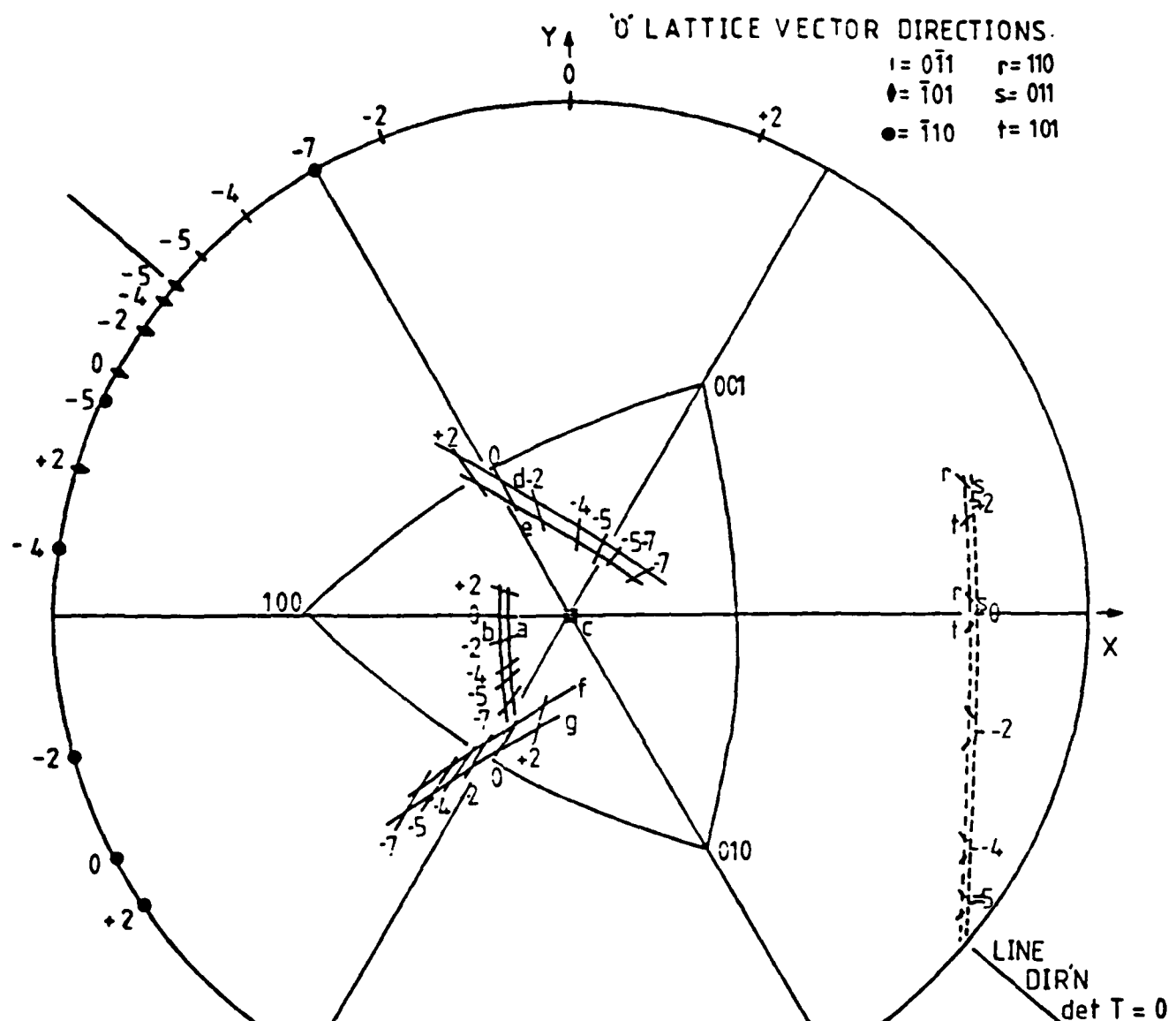


Figure 56

θ	i	$\theta = +2^\circ$	$\theta = 0^\circ$ (N-W)	$\theta = -2^\circ$	$\theta = -4^\circ$	$\theta = -5^\circ$	$\theta = -7^\circ$
	iii						
	ii						
	+						
	+						
	+						
	+						

Figure 57

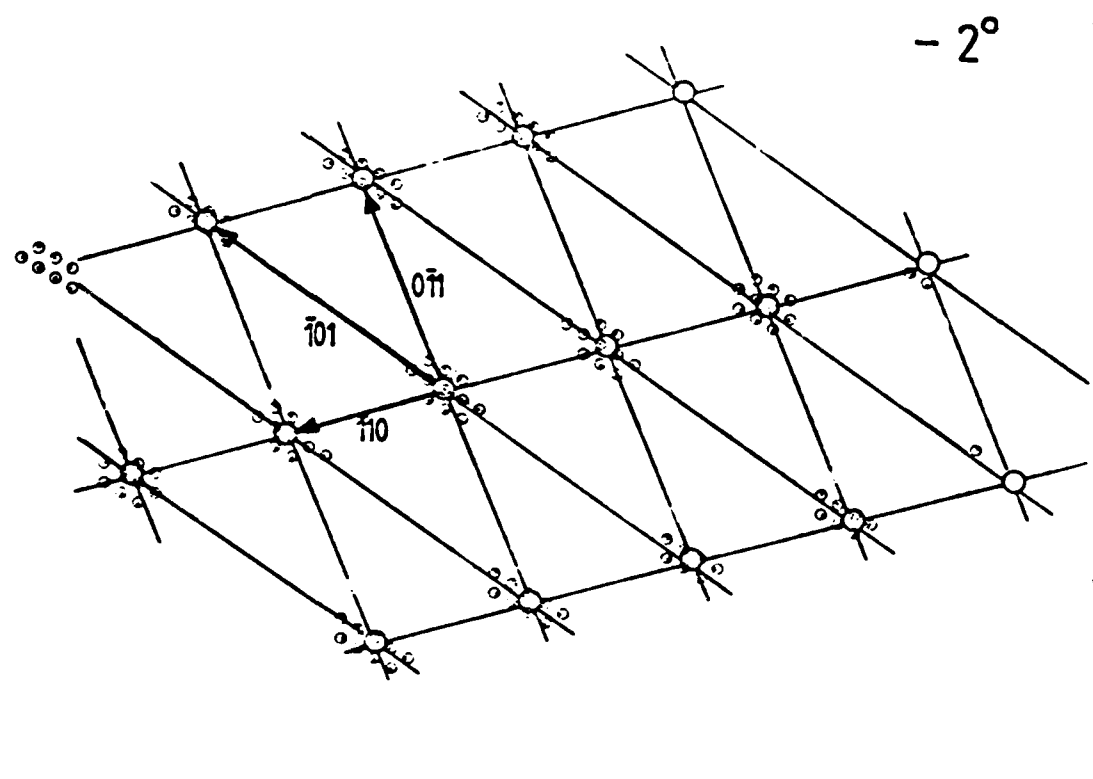
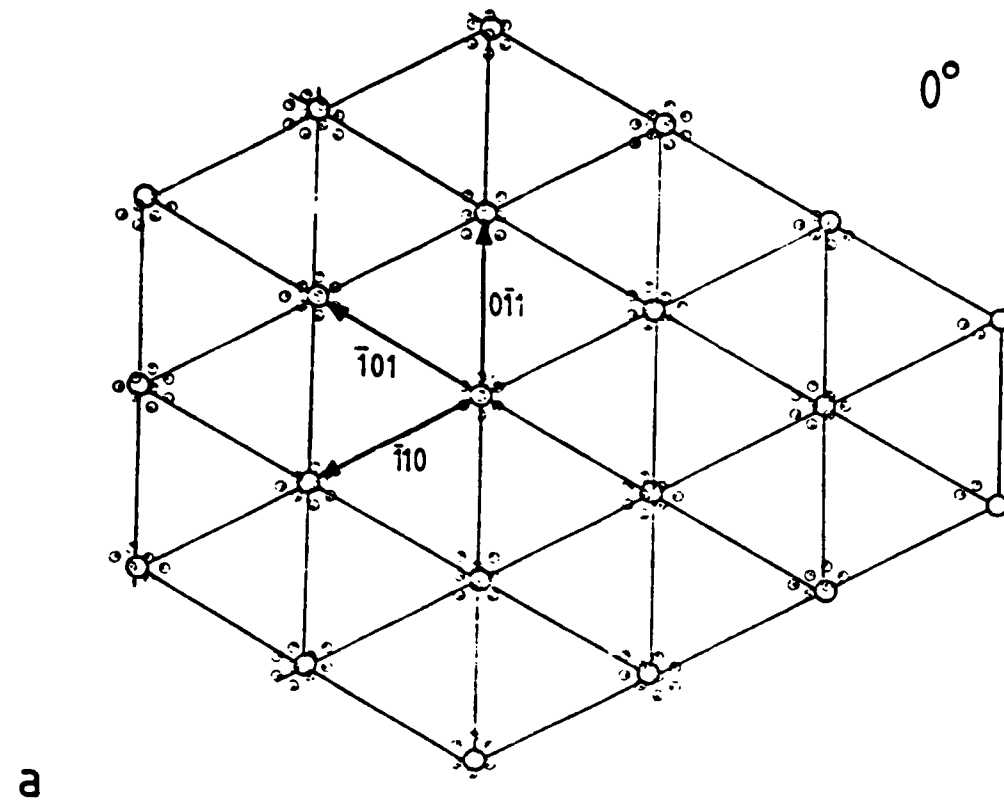


Figure 58

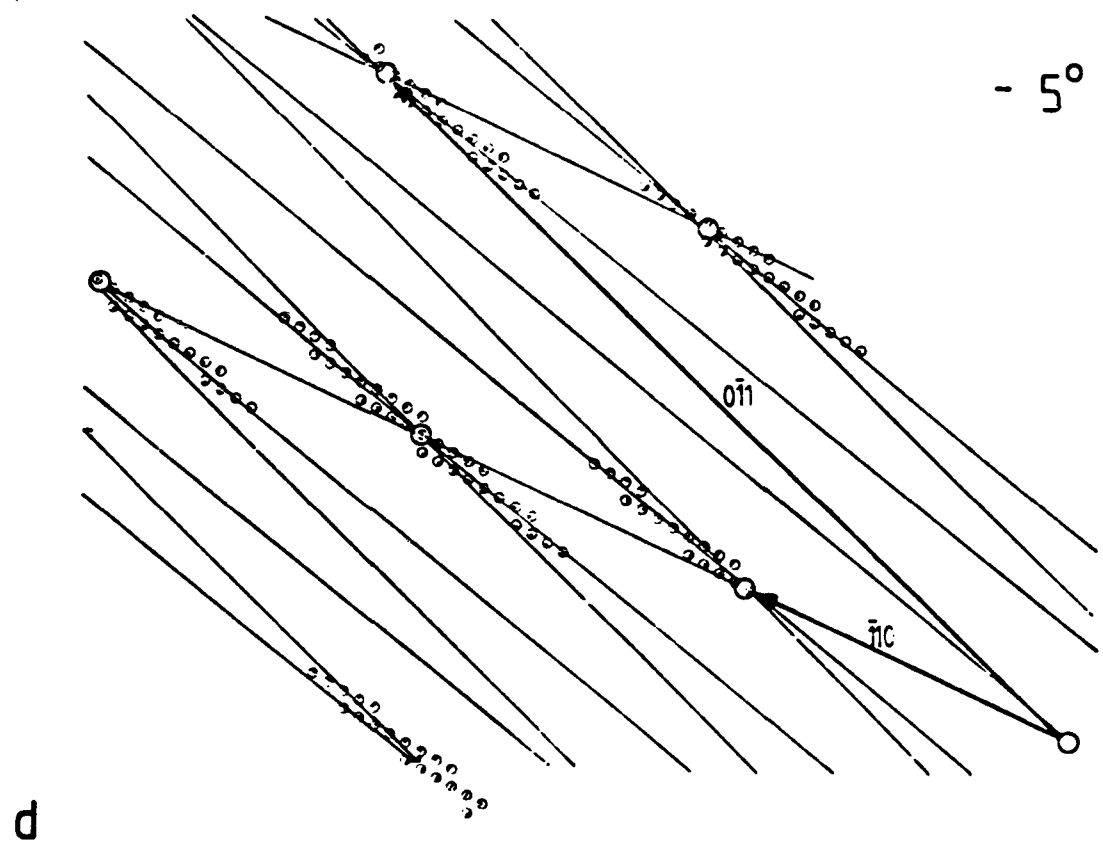
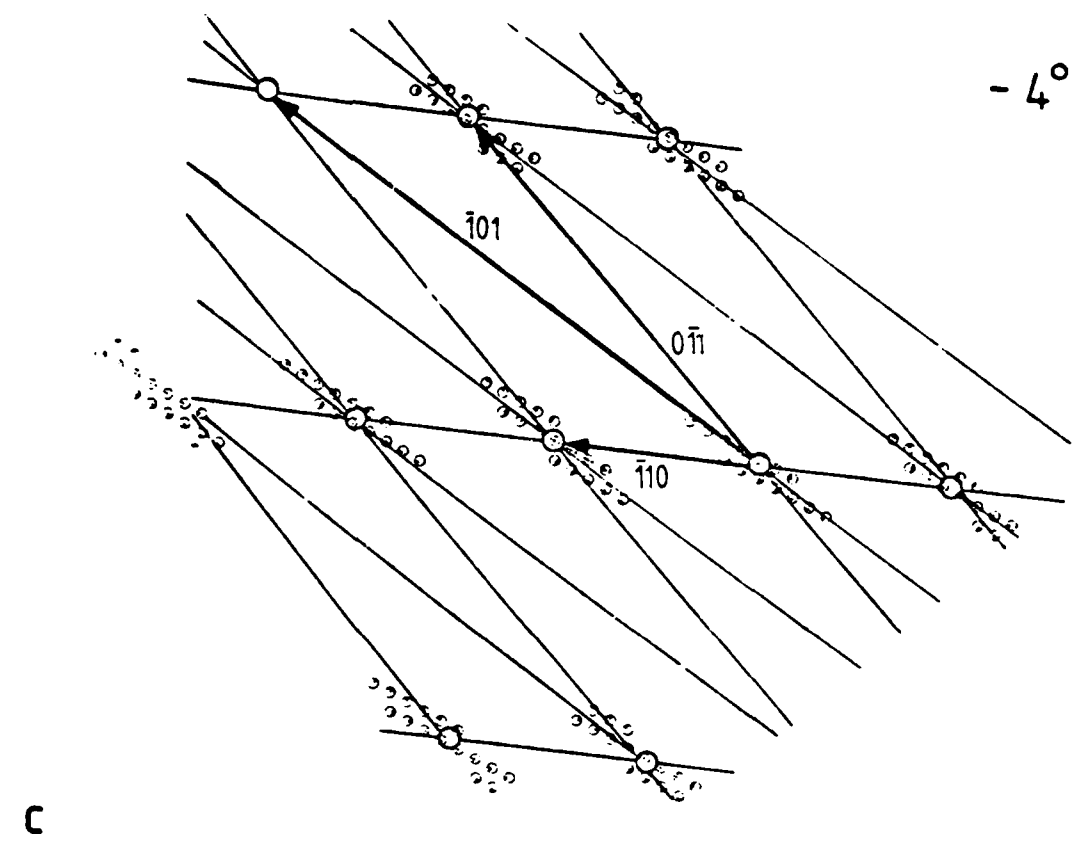


Figure 58 cont.

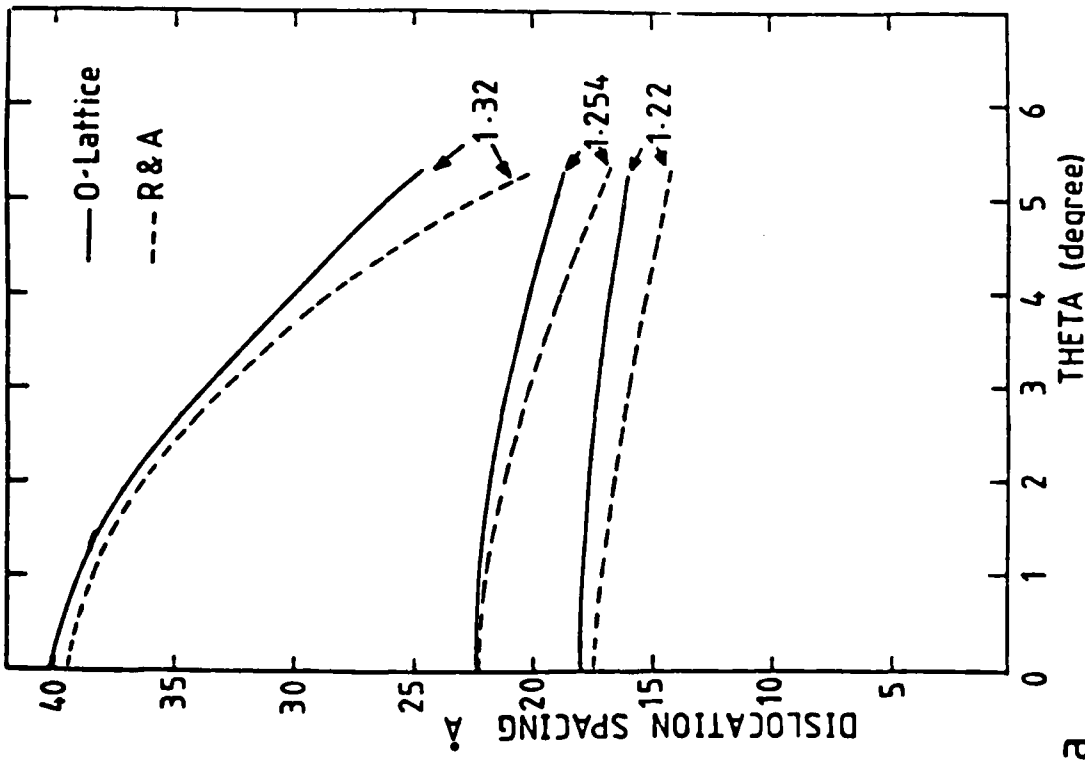
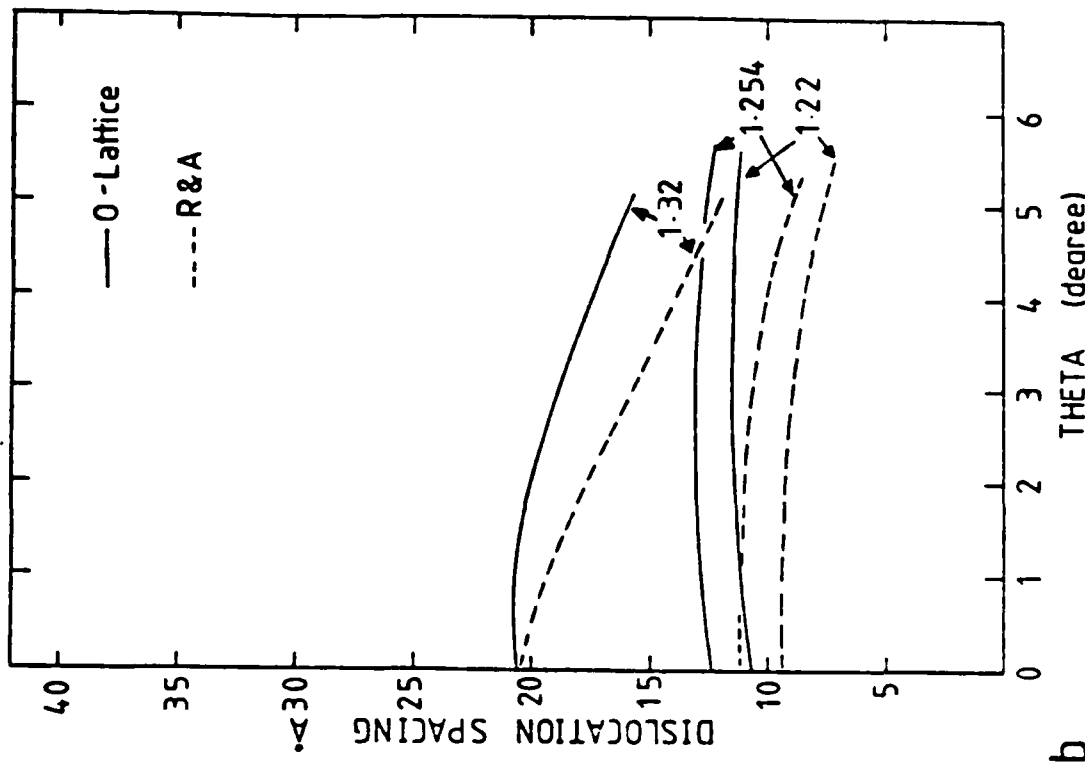


Figure 59

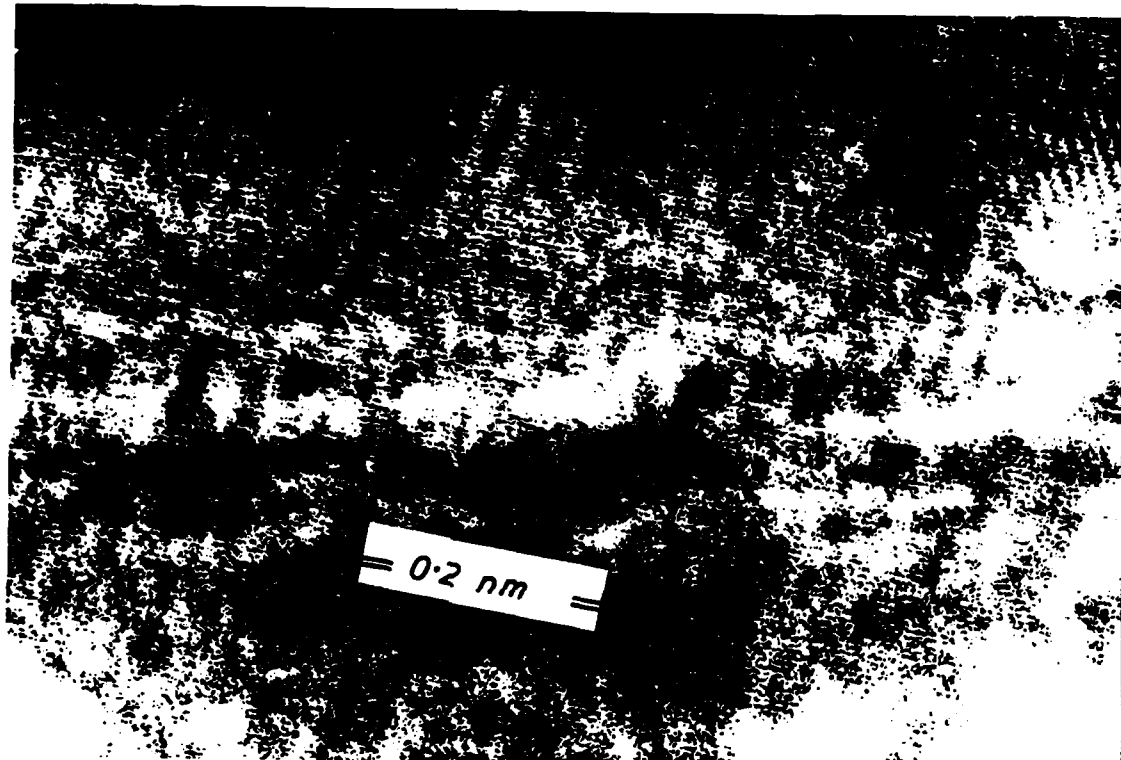


Figure 60

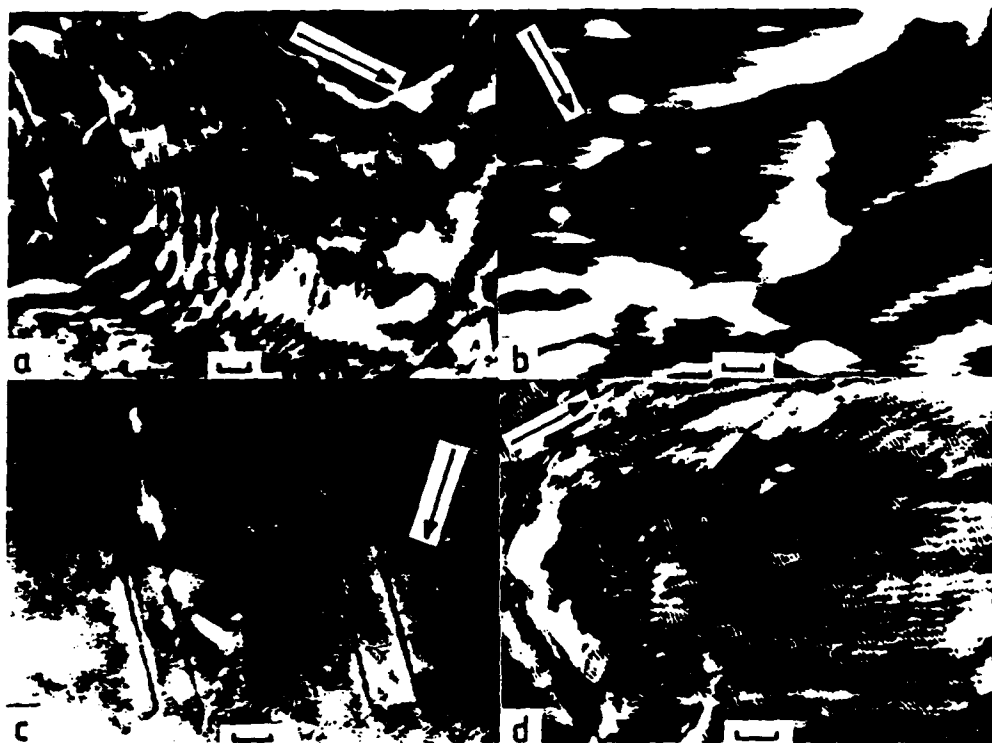


Figure 61



Figure 62

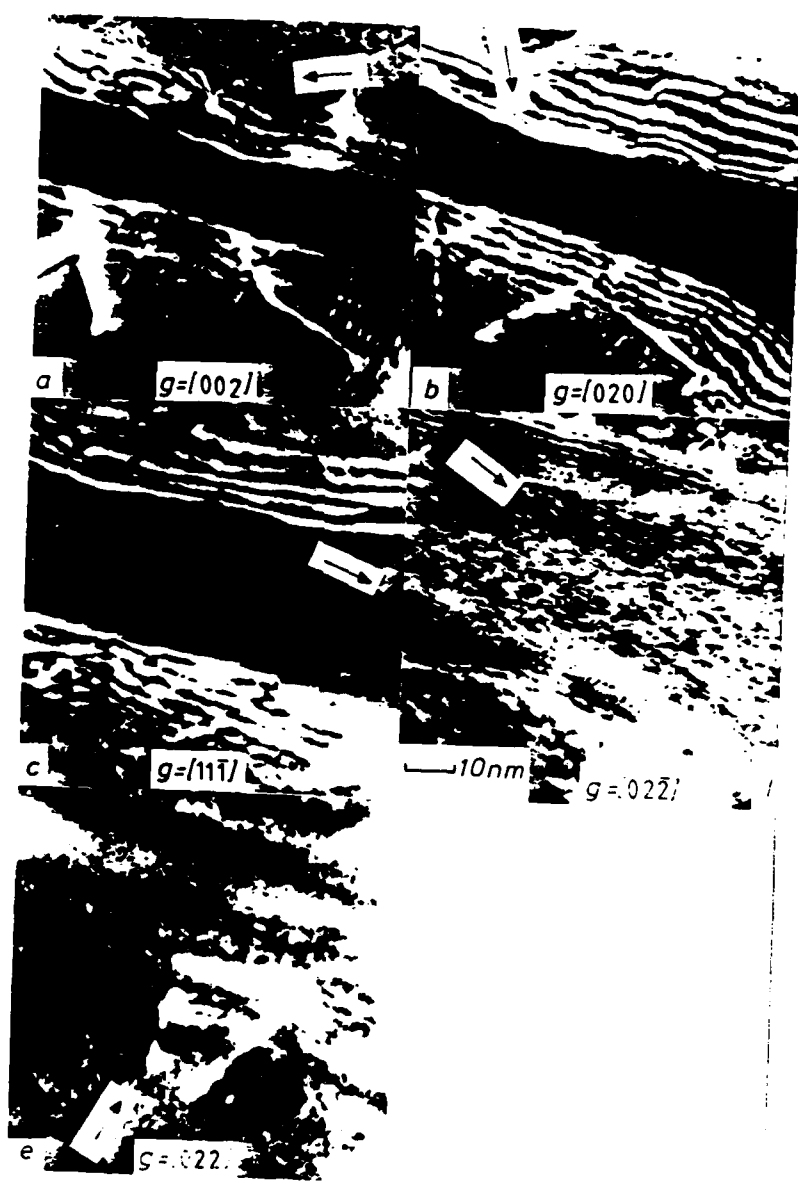


Figure 64

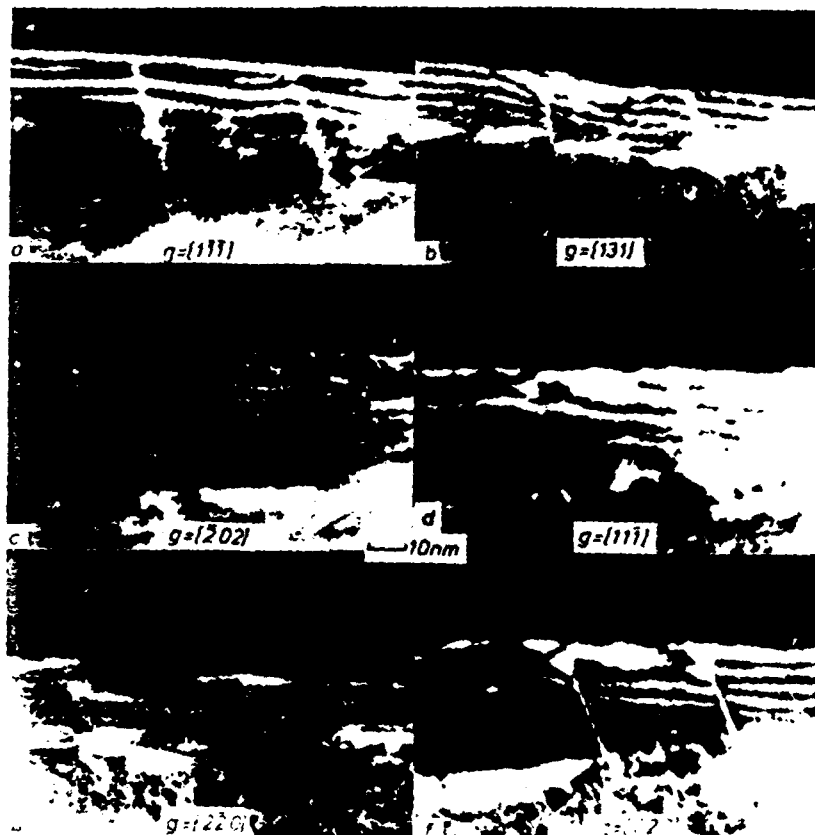


Figure 65

Table I--Summary of Microstructures in Fe-0.19% C-2.30% Mo Alloy

Temperature (°C)	Bay Temperature								
	625	615	610	595	575	550	525	500	475
Ferrite grain boundary nucleated									
intragranular			-----						
degeneracy			greater	greatest	greater				
Carbide fiber			-----						
I B P									
needle or plate on dislocation									
lath				-----					
Mo_2C									
$(\text{Fe}, \text{Mo})_3\text{C}$								-----	
$(\text{Fe}, \text{Mo})_6\text{C}$ on G. B.									
Retained Austenite				-----					
Twinned Martensite					-----				

Table II--Dislocation Burgers Vectors Expressed in Terms of FCC and BCC Crystals

	<u>FCC</u>	<u>BCC</u>
1	101	111
2	101	111
3	011	020
4	011	002
5	110	111
6	110	111

Table III--Theoretical and Observed Array Contrast Behavior--Lath Morphology

g _{fcc}	Observed Contrast	g.b for a/2 [011]	Dislocation Soacings (°A)		Dislocation Direction		Habit Plane	
			Measured	Theory	Observed	Theory	Observed	Theory
020	Strong	2						
002	Strong	2						
111	Not Available	0			Within 5° of theory			
022	Moiré	4	25.5	24.6		[211] fcc	Near (533) fcc	9.4° from (111)
111	Weak	2						
022	Weak	0						

Table IV--Theoretical and Observed Array Contrast Behavior--Equiaxed Morphology

A) Contrasts

g_{fcc}	Observed Contrast (23°A Array)	g.b for $a/2 [10\bar{1}]$	Observed Contrast (11°A Array)	g.b for $a/2 [\bar{1}10]$
$\bar{1}\bar{1}1$	Strong	2	None	0
$1\bar{1}1$	None	0	Strong	2
$02\bar{2}$	None	2	Strong	2
$20\bar{2}$	Strong	4	None	2
$0\bar{2}2$	None	2	Strong	2
$2\bar{2}0$	Weak	2	Weak	4

B) Spacings etc. (Projected onto 111_{fcc})

	23° Array		11° Array	
	Observed	Theory	Observed	Theory
Spacing (Å)	23	29	11	17
Direction (c.w. from $01\bar{1}$)	54°	74°	114°	124°
Angle between Array directions	60°	51°	-	-

END

FILMED

3-84

DTIC